ASDEX Contributions to the 8th International Conference on Plasma Surface Interaction in Controlled Fusion Devices

(Jülich, May 2 - 6, 1988)

and

International Workshop on Plasma Edge Theory

(Augustusburg (GDR), April 26 - 30, 1988)

IPP III/139 November 1988

MAX-PLANCK-INSTITUT FÜR PLASMAPHYSIK

8046 GARCHING BEI MÜNCHEN

ASDEX Contributions to the 8th International Conference on Plasma Surface Interaction in Controlled Fusion Devices

(Jülich, May 2 - 6, 1988)

and

International Workshop on Plasma Edge Theory

(Augustusburg (GDR), April 26 - 30, 1988)

IPP III/139 November 1988

ASDEX Contributions to the 8th International Conference
on Plasma Surface Interaction in Controlled Fusion Devices
(Jülich, May 2 - 6, 1988)

and

International Workshop on Plasma Edge Theory
(Augustusburg (GDR), April 26 - 30, 1988)

IMPURITY STUDIES

IMPURITY ACCUMULATION STUDIES IN PELLET-REFUELLED ASDEX DISCHARGES

G. Fussmann, K. Krieger, R. Nolte, H. Röhr, K.-H. Steuer
and the ASDEX team

ABSTRACT

Pellet injection into ASDEX discharges allows considerable improvement of the confinement properties. Simultaneously with this improvement a strong accumulation of metallic impurities is observed, which leads to intolerable cooling of the plasma core region. We discuss the experimental phenomena and the underlying transport changes associated with the accumulation.

INTRODUCTION

Repetitive injection of pellets has been successfully applied in ASDEX to improve substantially the energy confinement in ohmically and NI-heated plasmas /1/. A characteristic feature of the high confinement phase is the pronounced peaking of the electron density profile. Similar steep profiles have also been found under the improved conditions of ohmic confinement (IOC) and counter injection heating /2/. It is therefore reasonable to assume that the underlying physical mechanism which causes the change in transport is the same in all three cases. This is to be distinguished from the H-mode, where the improvement of energy confinement is mainly a result of broadening of the density profile. In the so-called quiescent H-mode (without ELMs) with excellent energy confinement we noticed for the first time distinct coupling between energy and particle confinement /3/. Such a correlation that links the transport properties of energy, background plasma particles, impurities, and - as seen more recently - also angular momentum /2/ seems to be a rather fundamental relation: it pertains in all four regimes mentioned above.

The detrimental consequences of this coupling relation with respect to density control and impurity accumulation has already been discussed in /4/. A matter of the utmost concern is the accumulation of metals because of the large central radiation losses that are easily produced. In the case of the quiescent H-phase, concentrations of about 1% Fe could build up within ~0.1 s owing to the enhancement of the global impurity confinement in connection with relatively large Fe influxes from the boundary region /5/. The situation for the three other regimes with peaked density profiles seems even more aggravated because of strongly increased neoclassical inward fluxes as a consequence of the steep pressure gradients in the inner plasma region. For this reason the suppression of the Fe fluxes by means of carbonization is a necessary prerequisite for successful operation. Nevertheless, the residual fluxes of copper from the divertor target plates can lead to severe radiation problems. In this respect the pellet discharges with extreme peaking ($n_e(o)\ \bar{n}_e \geq 2.0$) and very high axial densities ($n_e(o) = 1.4 \cdot 10^{14}$ cm^{-3}) are most delicate. In the following we give some detailed information on experimental observations made in such discharges.

Furthermore, the background and results of transport simulation directed at a conclusive description of the accumulation processes are outlined.

IMPURITY ACCUMULATION PHENOMENA

Impurity accumulation is observed for pellet injection into pure ohmic discharges and with moderate additional NI heating ($P_{NI} < 1.3$ MW). Here we will concentrate on a well-analysed discharge where 0.5 MW co-NI ($D^0 \rightarrow D^+$) was applied. This relatively small neutral injection power was added mainly for the purpose of CXR spectroscopy of light impurities ($P_{OH} = 0.4$ MW). The resulting small rotation velocity of $v_\phi(o) < 0.5 \cdot 10^5$ m/s is believed to be insignificant with regard to accumulation.

The measured line-averaged and axial densities $\bar{n}_e$ and $n_e(o)$ as well as the central radiation $P_{rad}(o)$ and the soft X-ray emission along a central chord (SX) are shown in Fig. 1 as functions of time. The central radiation is seen to rise drastically about 100 ms after the injection of the last pellet. Simultaneously, the electron density profile starts peaking and the sawtooth activity disappears. After about 200 ms central radiation losses of 0.3 W/cm^3 are reached, this being already larger than the input power density of $P_{in}(o) \approx P_{OH}(o) = 0.2$ W/cm^3. The radiation profiles as determined from bolometer and SX-array measurements strongly peak on axis for $t \geq 1.3$ s.

VUV spectra (100-320 Å) taken at time intervals of 20 ms show line emission of only three elements: C, O and Cu. During the accumulation phase the spectra change only in the lower wavelength range $\lambda \leq 130$ Å, where some so far unidentified strong lines (132.85 Å, 110.4 Å), and numerous weak ones appear. In particular, the intensity of CVI and CIV lines, which are indicative of the influx of light impurities, stay nearly constant. For the discharge considered, where the T_e changes are marginal, no significant changes in the prominent line emission of CuXVIII (235 Å) and CuXIX (274, 304 Å) are observed either. However, these lines from Mg- and Na-like ions are also emitted relatively far out ($r/a \approx 0.75$) and are thus again more representative of the Cu influx than its central concentration. In the core region Cu is predicted to be in the O to Ne-like states, comprising a complex and not well-known line pattern in the range 10 - 100 Å which is not accessible to survey spectrospoy in ASDEX.

For the above reasons the Cu density on axis must be determined from bolometer measurement via $P_{rad} = n_{Cu} \cdot n_e L_{Cu}$, with the radiation rate coefficient $L_{Cu}(T_e)$ being obtained from code calculations. In a similar way the soft X-ray emission density ε_{SX} can be treated by applying the proper Be-filter absorption function in the code calculations. From $P_{rad}(o) = 0.3$ W/cm^3, measured at $t = 1.4$ s, we deduce a Cu concentration of $8.5 \cdot 10^{-4}$ for the core region. This Cu density is fairly consistent with calculated (0.10 W/cm^3) and measured (0.13 W/cm^3) values of $\varepsilon_{SX}(o)$. The contribution of 0.08% Cu to Z_{eff} amounts to 0.3 only. Corrections arising from C and O bremsstrahlung are of the order of 10% and are thus small in comparison with the uncertainty in the calculation of L_{Cu}, which is certainly in the range of ± 30%.

Information on the important question whether light impurities also accumulate is obtained from 16-channel Z_{eff} bremsstrahlung measurements /6/. Radial Z_{eff} profiles determined from these measurements are shown in Fig. 2a for the ohmic phase and in Fig. 2b for the fully developed accumulation period. The bolometrically determined profiles of P_{rad} and reduced radiation profiles P_{rad}/n_e are also plotted for the purpose of demonstrating the accumulation. The quantity $(Z_{eff} - 1)$, which is representative of the (C + O) concentration is seen to increase only moderately from 0.4 to 0.6 at half minor radius. Even for the plasma centre the changes are not pronounced: subtracting the Cu contribution of 0.3, we notice growth from 0.6 to 1.1 for $(Z_{eff} - 1)$. The resulting concentrations during the accumulation phase amount to 2% carbon and 0.8% oxygen if we assume a ratio of the elements as measured in the boundary region.

IMPURITY TRANSPORT ANALYIS

As outlined in /4/, we tentatively describe the transport of impurities by adding collisional (classical + neoclassical) and anomalous fluxes. For the latter we allow only a diffusive part $\Gamma_{an} = D_{an}\, \partial n_z/\partial r$ since additional anomalous inward drifts of the order of $v_{an} \approx D_{an} r/2a^2$ would yield already appreciably peaked impurity profiles under low confinement conditions, which are not observed in the experiments. On the other hand, anomalous convective terms have to be postulated for the background plasma. These can be understood in terms of favourable phase relations between density perturbations and poloidal electric field fluctuations. However, such a phase relation can be different or absent (as is assumed here) for the impurities because of marked up-down assymetries or other reasons.

The collisional transport is based on the formulation worked out by Hirshmann and Sigmar /7/ and is used in the specialized form presented in /8/ and /4/. The neoclassical banana-plateau fluxes taken therein apply particularly for the case that both impurities and background ions are in the plateau regime. To demonstrate that this assumption is justified, we have plotted the collisionalities for carbon-carbon (ν^*_{cc}) and deuteron-deuteron (ν^*_{ii}) in Fig. 3 versus radius for the discharge under discussion at t = 1.4 s. The background ions are seen to be in the plateau regime in the core and boundary regions and are in the collisionless banana regime around half minor radius. In this middle zone our treatment is not strictly applicable. However, the corrections to be made are small and result primarily in a minor reduction of the temperature gradient term. Because of the scaling $\nu^*_{zz} = \nu^*_{ii} \cdot Z^4 n_z/n_i$ for the self-collisionality, metals (Cu) with $Z \approx 20$ but with concentrations as low as 10^{-4} are generally found in the plateau regime, too. These considerations apply particularly to the important BP fluxes driven by the self-viscosity of the various ions. A complete theory, which would also have to take into account the mixed viscosity terms, is still missing. A correct treatment of the multi-impurity case is therefore not possible at present. Consequently, any C-Cu interaction has been omitted in our calculations, which, in any case, are a reasonable approximation as long as the collision strength $\alpha = Z^2 n_z/n_i \approx Z_{eff}^{-1}$ for carbon is less than unity. Finally, we show in Figs. 4a and 4b the various collisional contributions to the diffusion coefficient and drift velocity for carbon as a function of the radius.

To compare experiment and theory, further assumptions must be made which have a more or less sensitive influence on the results assumed:

1. Constant influxes from the boundary.
2. Reduction of D_{an} takes place at time $t = t_0 = 1.2$ s when the sawteeth disappear.
3. The reduction occurs only within the inner zone $r \leq 0.75$ a.
4. Within this zone the residual anomalous diffusion coefficient is kept constant at a level of $D_{an} = 0.05$ m^2/s, as is measured for the central diffusion coefficient of the background plasma /1/.

Whereas assumptions 1 to 3 are relatively uncritical, the residual value of D_{an} must of course be chosen small enough in comparison with $D_{coll} \approx 0.1$ m^2/s to obtain sufficient impurity peaking. The influence of this parameter is demonstrated in Fig. 5 where the measured SX profile at $t = 1.4$ s is compared with Cu simulations. As seen from the figure, the narrowness of the measured profile postulates a reduction of D_{an} from 0.8 m^2/s down to <0.1 m^2/s. The above model can also fairly describe the temporal evolution of the SX traces. In comparison with this good consistency found for Cu, the situation is less satisfying for carbon since so far no reliable CXRS measurements could be obtained. The comparison can only be made via Z_{eff} as it is shown in Fig. 6 for three different times during the accumulation period. In these calculations oxygen is not distinguished from carbon. We notice that apart from the region $r > a/2$, where the measured profiles tend to increase again, the agreement between experiment and calculation is fairly good.

DISCUSSION

In pellet-refuelled discharges considerable improvement of the energy confinement can be achieved. The effect is correlated with a marked peaking of the plasma density. Concomitant with this improvement, a highly unfavourable accumualation of metallic impurities in the plasma centre is observed. Light impurities such as carbon and oxygen also show the tendency to accumulate, but without critical consequences for the plasma performance and with still tolerable dilution effects of less than 20%.

Our simulation calculations corroborate the basic concept according to which the accumulation process results from a reduction of the anomalous diffusive terms (assumed to be associated with turbulence), which normally compensate for the large neoclassical inward drifts of the impurities. In addition, the effect is significantly amplified by the large central pressure gradients occurring in these discharges. Applying this model, we obtain a satisfying description for copper, whereas for carbon the agreement is not as concincing. There are still several parameters undefined in such simulations, which can change the outcome to a certain extent. Thus, the residual value of the anomalous diffusion coefficient can be chosen within a range of zero to about 0.1 m^2/s. Furthermore, the extent of the radial zone where the reduction takes place is rather uncertain. In fact, the accumulation would still be dangerous if this region of improved confinement is only about 1/3 of the cross-section. In this case a marginal improvement of the global energy confinement is to be paid for with grave

radiation loss problems induced by accumulation in the core zone. Two ways of overcoming this shortcoming are conceivable. Firstly, a reduction of all metals to concentrations of $\leq 10^{-5}$ under normal confinement conditions would presumably suffice and seem to be attainable in a fully carbonized machine. Secondly, any method that allows continuation of the sawtooth activity might help as well. As discussed in /4,9/, sawteeth are found to have a cleaning effect in the central region and their disappearance is probably caused by the decreasing conductivity during the accumulation phase. This lowering of the conductivity is in turn produced by increased impurity fluxes into the central regions that tend to raise Z_{eff} and, in addition, cool the plasma. If cooling is dominant for the reduction of conductivity, HF heating in the core region should help to overcome the problems.

REFERENCES

/1a/ M. Kaufmann, K. Büchl, G. Fussmann et al., Nucl. Fus., 28, 5 (1988).
/1b/ M. Kaufmann, et al., Proc. 12th Intern. Conf. on Plasma Phys. and Contr. Nucl. Fus. Research, Nice, 1988, paper IAEA-CN-50/A-4-2
/2/ G. Fussmann, O. Gruber, H. Niedermeyer et al., ibid, paper IAEA-CN-50/A-3-1.
/3/ M. Keilhacker, G. Fussmann, G.v.Gierke et al., Proc. 10th Intern. Conf. on Plasma Phys. and Contr. Nucl. Fus. Research, London, 1984, Vol. 1, 71.
/4/ G. Fussmann, J. Hofmann, G. Janeschitz et al., Proc. 8th Intern. conf. on Plasma Surface Interactions in Contr. Fus. Devices, Jülich, 1988, paper 60.
/5/ E.R. Müller, G. Janeschitz, P. Smeulders and G. Fussmann, Nucl. Fus. 27, 11, 1817-1825, (1987).
/6/ K.-H. Steuer, H. Röhr, D.E. Roberts, A. Eberhagen, G. Janeschitz, G. Fußmann et al., Proc. 15th Europ. Conf. on Contr. Fus. and Plasma Phys., Dubrovnik, Vol. 12 B, 31 (1988).
/7/ S.P. Hirshman and D.J. Sigmar, Nucl. Fus. 21, 9, 1079-1201 (1981).
/8/ TFR Group, Nucl. Fus. 22, 9, 1173-1189, (1982).
/9/ G. Fussmann, G. Janeschitz, G. Becker et al., Proc. 14th Europ. Conf. on Cont. Fus. and Plasma Phys., Madrid, Vol. 11D, 41 (1987).

FIGURE CAPTIONS

Fig. 1 Temporal development of line-averaged density $\bar{n}_e$ and peak density $n_e(o)$ for a pellet-refuelled discharge (t = 1.05 - 1.20 s) with a small amount of neutral injection heating. The traces of the central radiation density $P_{rad}(o)$ and the chord-integrated soft X-rays are also shown.

Fig. 2 Profiles of Z_{eff} determined from bremsstrahlung measurement, P_{rad} and reduced radiation density P_{rad}/n_e for the ohmic phase (2a) and the impurity accumulation phase (2b).

Fig. 3 Collisionality of deuterons (ν^*_{ii} and carbon impurity ions (ν^*_{zz}) as a function of radius. The banana plateau limit $\nu^* = 1$ and the Pfirsch-Schlüter limit $\nu^* = (R_o/r)^{3/2}$ are also plotted.

Fig. 4 Collisional diffusion coefficient (4a) and drift velocity (4b) for carbon vs. radius. The various contributions from neoclassical (BP), classical, and Pfirsch-Schlüter (PS) type terms are indicated.

Fig. 5 Comparison of a measured soft X-ray profile during the accumulation phase with simulations for Cu. The sensitivity of the calculations with respect to the reduction of D_{an} from 0.8 m^2/s (unchanged) to 0 (fully collisional) is demonstrated.

Fig. 6 Comparison of measured (***) and calculated Z_{eff} profiles at three different times during the accumulation phase. In the calculation only contributions from carbon are taken into account.

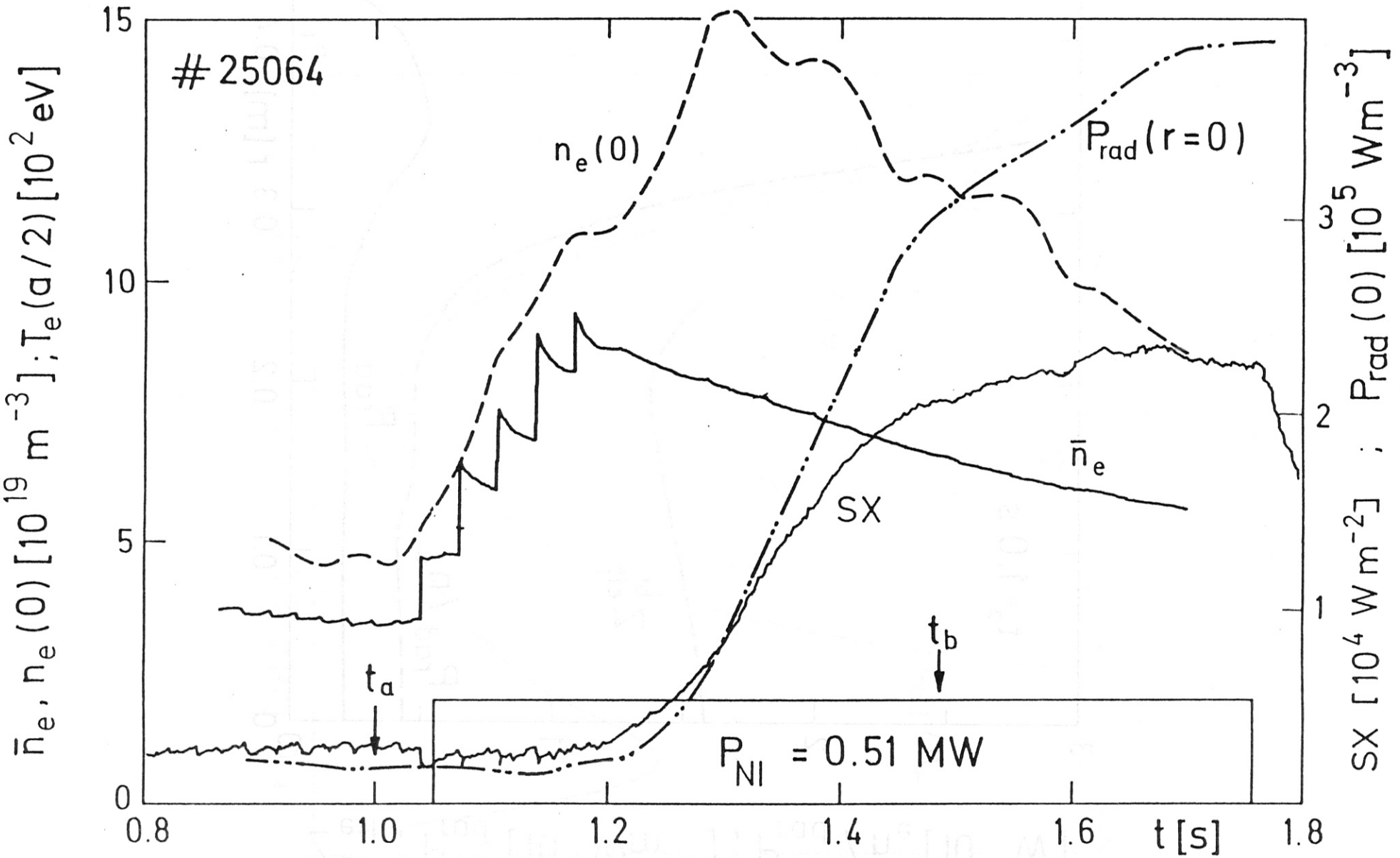
#25064
$n_e(0)$
$P_{rad}(r=0)$
$\bar{n}_e$
SX
t_a
t_b
P_{NI} = 0.51 MW
$\bar{n}_e$, $n_e(0)$ [10^{19} m^{-3}]; $T_e(a/2)$ [10^2 eV]
SX [10^4 W m^{-2}] ; $P_{rad}(0)$ [10^5 W m^{-3}]
t [s]
0
5
10
15
1
2
3
0.8
1.0
1.2
1.4
1.6
1.8

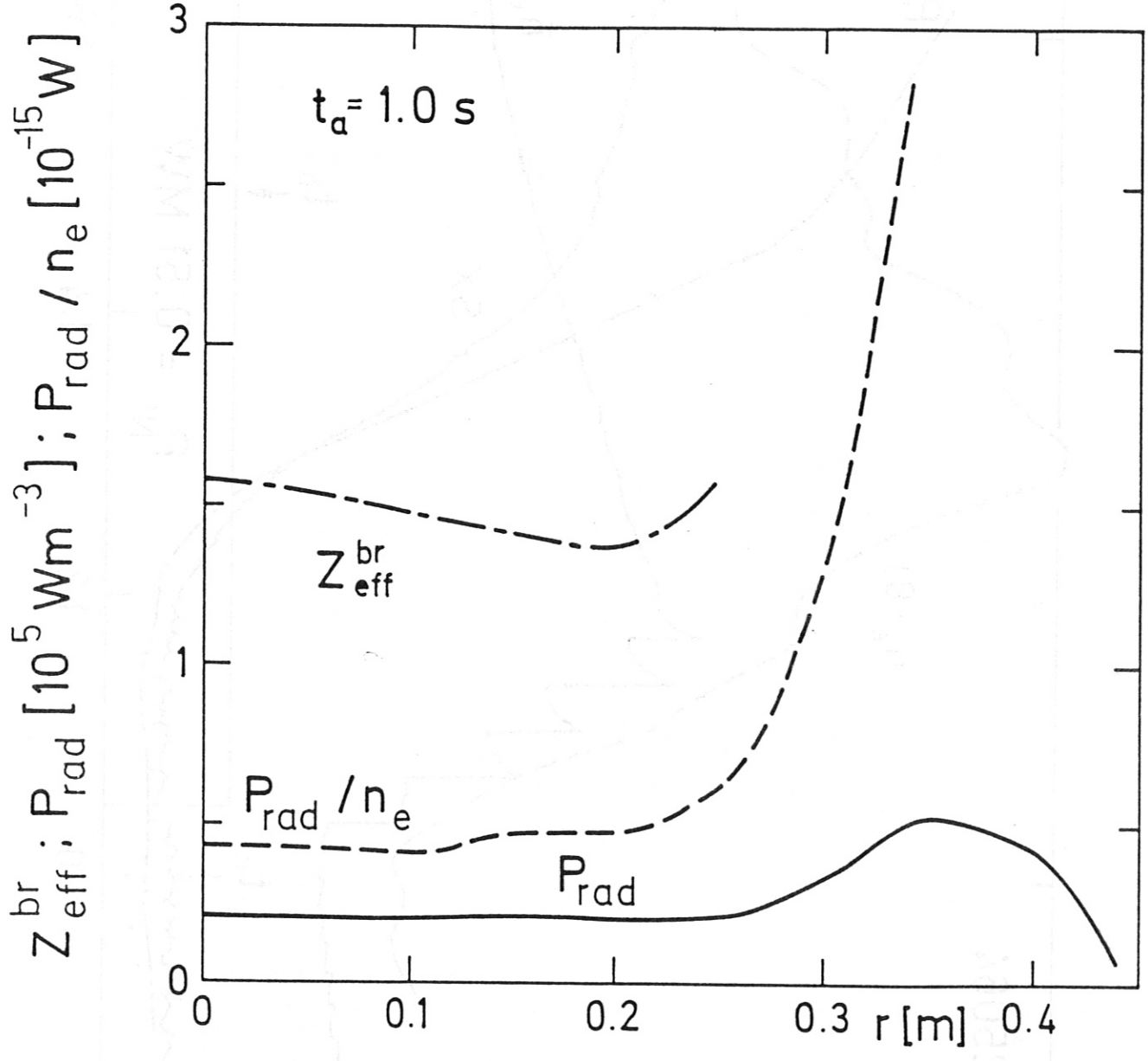
Z_{eff}^{br} ; P_{rad} [10^5 Wm^{-3}] ; P_{rad} / n_e [10^{-15} W]
t_a = 1.0 s
Z_{eff}^{br}
P_{rad} / n_e
P_{rad}
r [m]
0
0.1
0.2
0.3
0.4
1
2
3

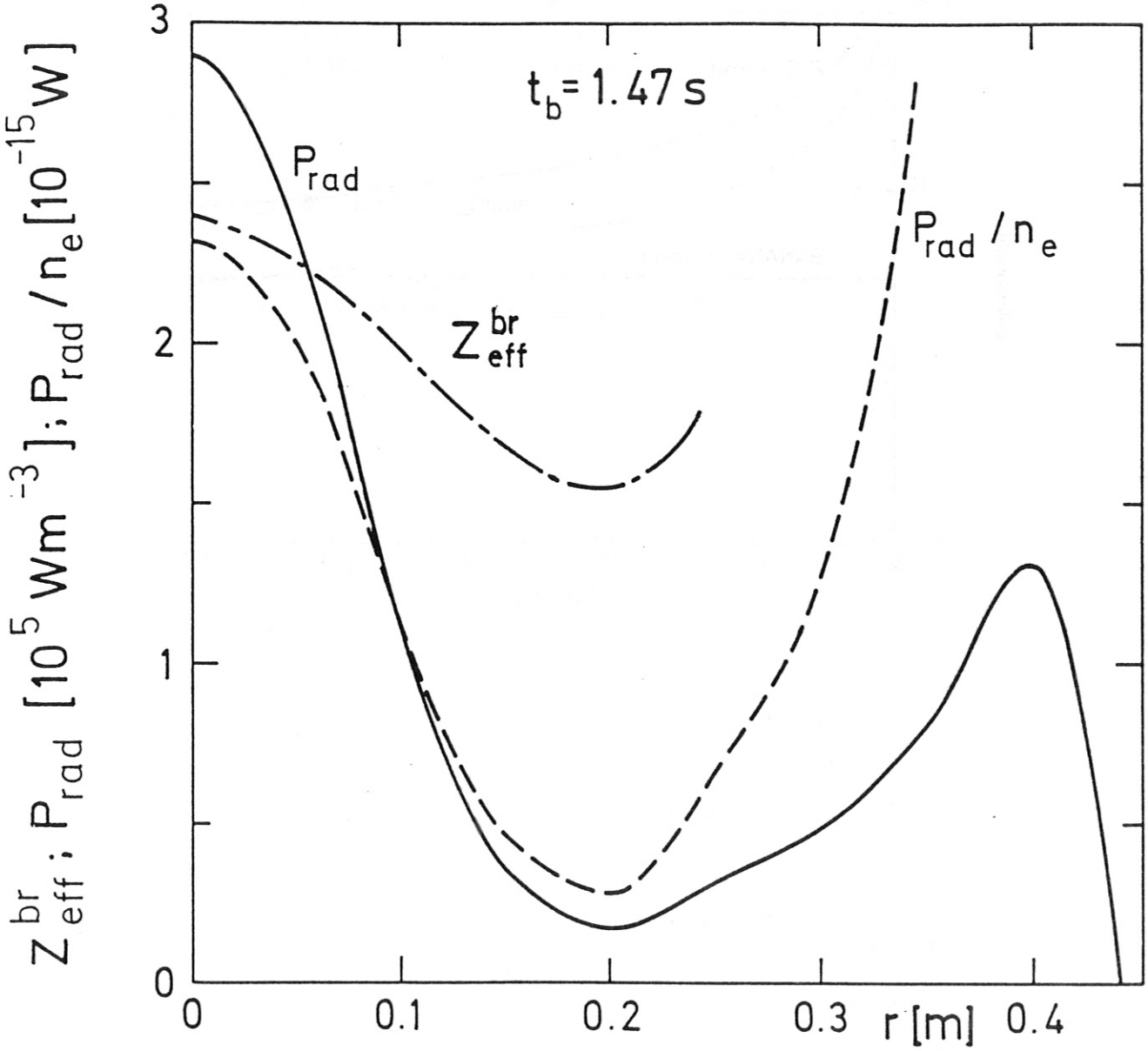
$t_b = 1.47\,s$
P_{rad}
P_{rad}/n_e
Z_{eff}^{br}
Z_{eff}^{br} ; P_{rad} [10^5 Wm^{-3}]; P_{rad}/n_e [10^{-15} W]
r [m]
0
0.1
0.2
0.3
0.4
1
2
3

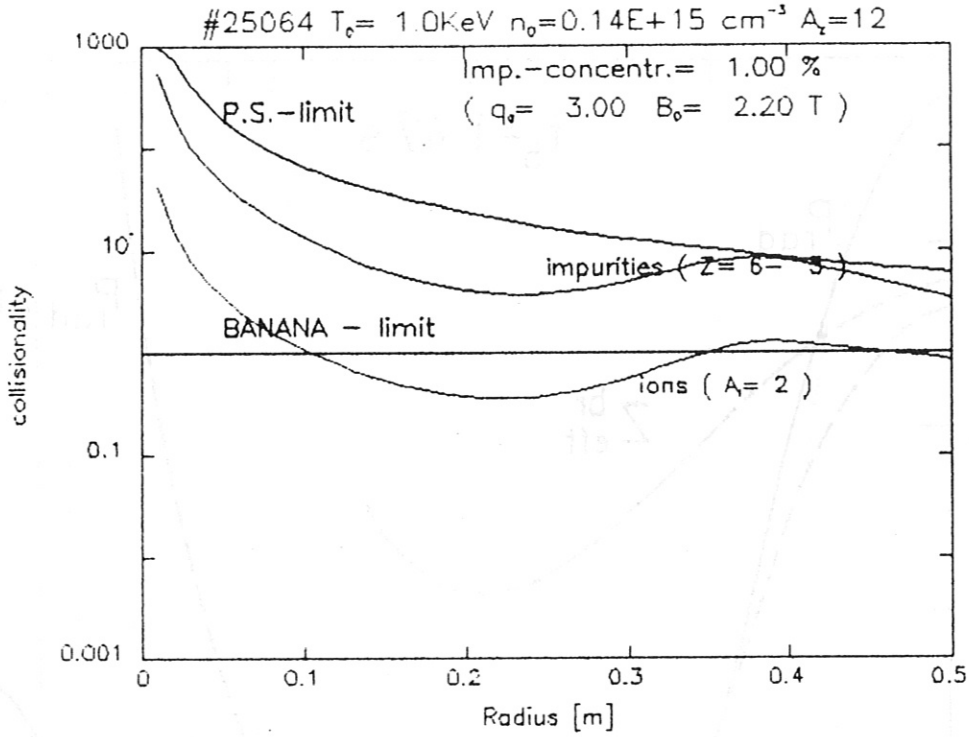
#25064 T_e= 1.0KeV n_e=0.14E+15 cm^{-3} A_z=12
Imp.-concentr.= 1.00 %
(q_a= 3.00 B_o= 2.20 T)
P.S.-limit
impurities (Z= 6- 9)
BANANA - limit
ions (A_i= 2)
collisionality
1000
10
0.1
0.001
0
0.1
0.2
0.3
0.4
0.5
Radius [m]

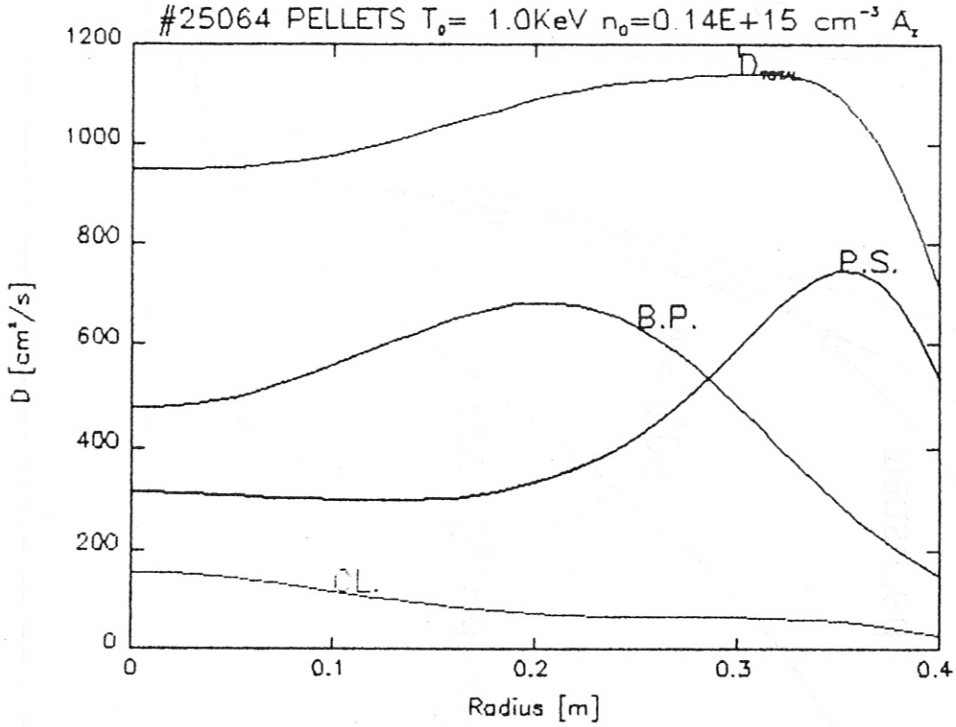
#25064 PELLETS T_0= 1.0KeV n_0=0.14E+15 cm^{-3} A_z
D_{TOTAL}
P.S.
B.P.
CL.
D [cm^2/s]
Radius [m]
1200
1000
800
600
400
200
0
0
0.1
0.2
0.3
0.4

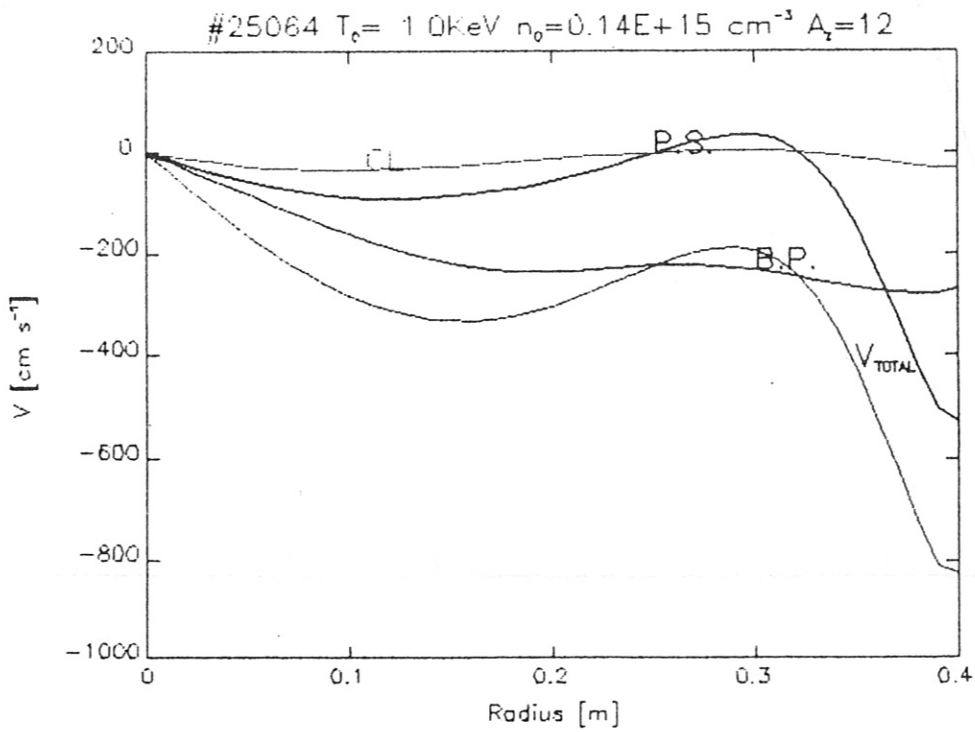
#25064 T_0= 1.0KeV n_0=0.14E+15 cm^{-3} A_z=12
CL
P.S.
B.P.
V_{TOTAL}
V [cm s^{-1}]
Radius [m]
200
0
-200
-400
-600
-800
-1000
0
0.1
0.2
0.3
0.4

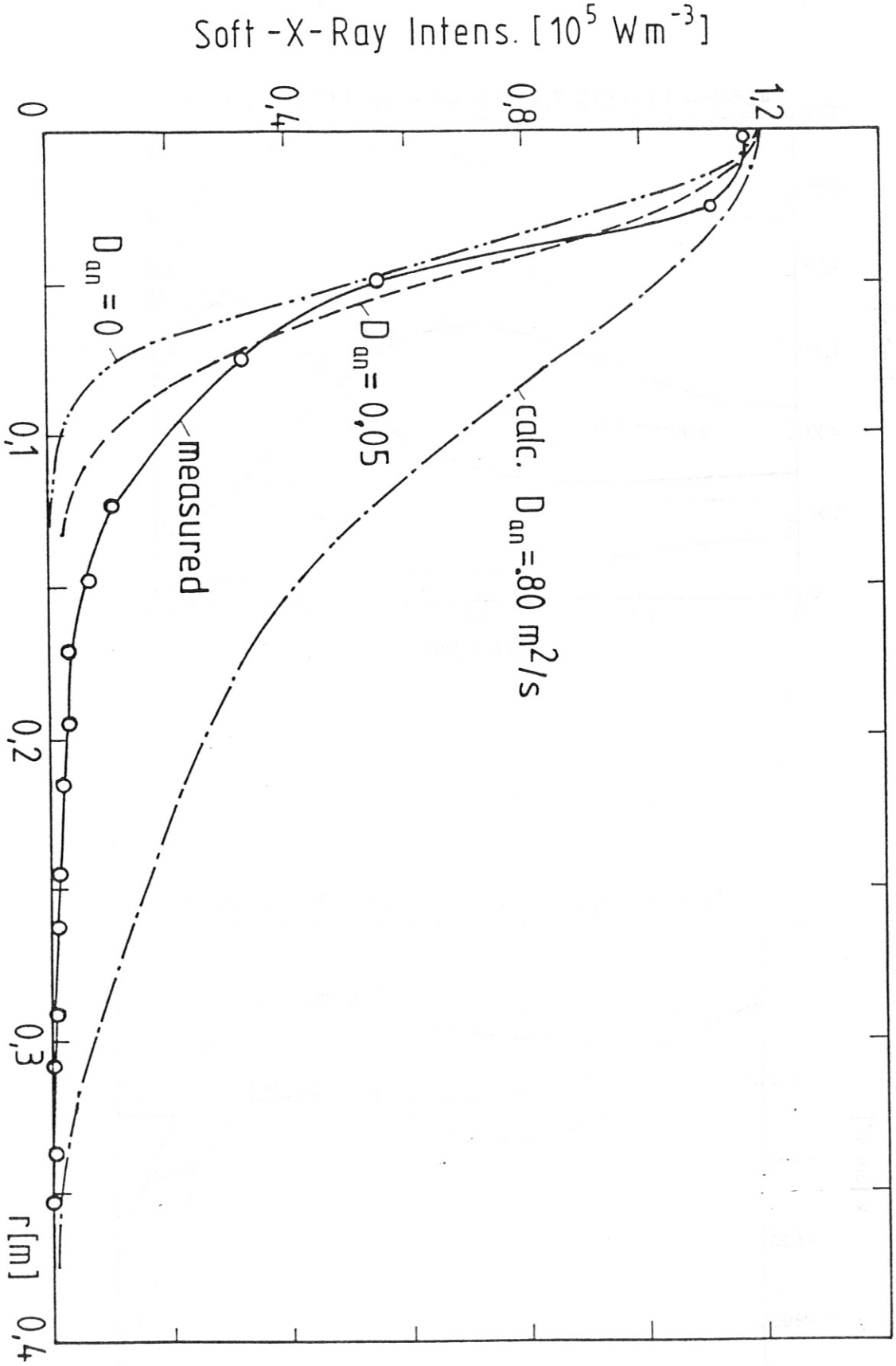
Soft-X-Ray Intens. [10^5 Wm^-3]
0
0,4
0,8
1,2
0,1
0,2
0,3
0,4
r[m]
D an = 0
D an = 0,05
measured
calc. D an = 80 m^2/s

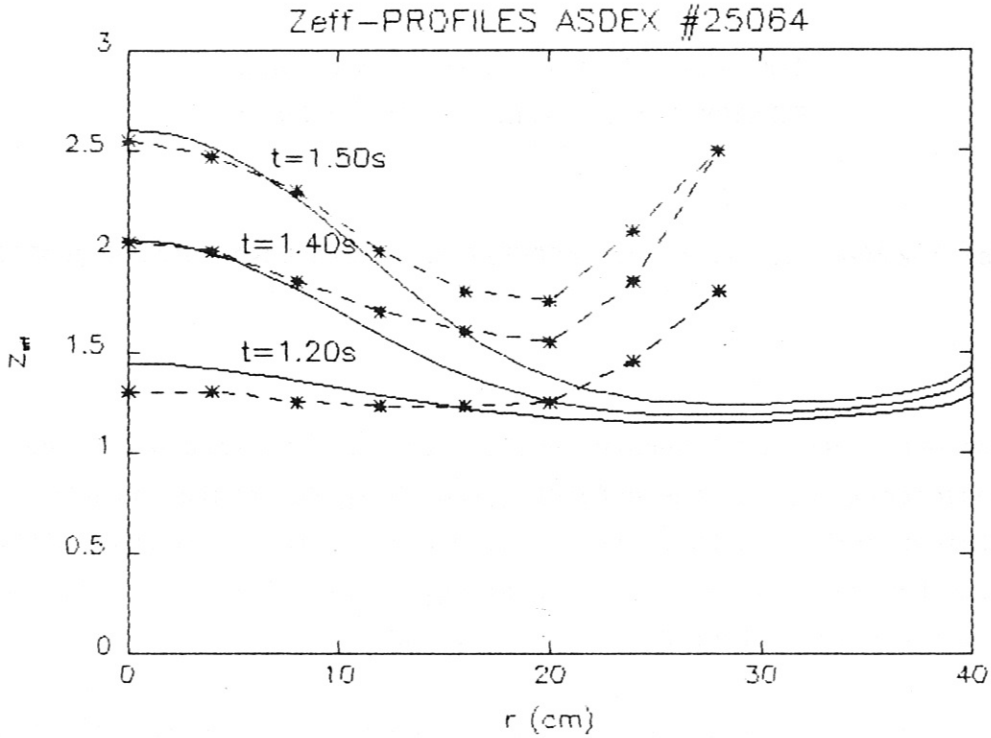
Zeff-PROFILES ASDEX #25064
t=1.50s
t=1.40s
t=1.20s
Zeff
r (cm)
0
0.5
1
1.5
2
2.5
3
0
10
20
30
40

Characterization of the ASDEX Scrape-Off-Layer Density Profile During Neutral Beam Heating

G.K. McCormick, Z.A. Pietrzyk[1], ASDEX-Team, NI-Team

Max-Planck-Institut für Plasmaphysik
EURATOM Association, D-8046 Garching

Key words: tokamak, ASDEX, scrape-off-layer, plasma edge density profile

Abstract

The scrape-off-layer (SOL) density profile is characterized by the density at the separatrix n_s, and the e-folding length λ_n for ohmic and H°-neutral-injection-heated (NI) plasmas at power levels P_{NI} leading either only to the L-mode (low power injection: P_{NI} = 0.4 - 1.7 MW), or to the H-mode (high power injection: P_{NI} = 2.4 - 3.4 MW).

Behavior of the SOL at low P_{NI} is studied over the ranges: $\bar{n}_e$ = 1 - 5 x $10^{13}/cm^3$, I_p = 270 - 420 kA and B_t = 21.8 kG, for D^+ and He^{++} (only 420 kA) discharges. It is found: $n_s(OH) \propto \bar{n}_e I_p^{0.25}$; $n_s(L) \propto \bar{n}_e I_p^{-0.5}$ and $\lambda_n(OH+L) \propto \bar{n}_e^{-0.22} I_p^{-0.6} P_{tot}^{0.19}$, where P_{tot} is the total power absorbed by the plasma. More explicitly, n_s is proportional to $\bar{n}_e$, whereby the constant of proportionality increases at the onset of NI, but is independent of P_{NI}.

For high P_{NI}, over the ranges $\bar{n}_e$ = 1.8 - 5 x $10^{13}/cm^3$, I_p = 220 - 415 kA and B_t = 16.7 - 25.1 kG, the relationships $n_s(L) \propto n_e^{1.55} I_p^{-1}$ and $n_s(H) \propto n_e^{2.2} P_{tot}^{-2.5}$ emerge, the scaling for $n_s(H)$ applying only at the onset of the H-mode. However, due to the small size of the data base, these scalings may be taken only as indicative. For λ_n: $\lambda_n(L)/\lambda_n(OH) \sim 1.3 \pm 0.27$ and $\lambda_n(H)/\lambda_n(OH) \sim 0.7 \pm 0.12$, with single-null-diverted (SN) discharges exhibiting the smaller values of $\lambda_n(L)$. The decrease in λ_n to $\lambda_n(H) \sim 1.0$ - 1.4 cm upon attainment of the H-mode occurs on a sub-ms time scale. Typically, both $\lambda_n(H)$ and $n_s(H)$ exhibit little change from their initial

[1]Univ. of Washington, Seattle, USA under the DOA-IEA agreement

values, regardless of the subsequent development of β_p or $\bar{n}_e$. Edge-localized-modes (ELMs) inject particles into the SOL in a time less than 200 µs, producing an extreme enhancement of λ_n (greater than a factor of four), which decays back to the pre-ELM valve within a few ms.

1. Introduction

Previous papers on the ASDEX SOL density profile using lithium-beam-spectroscopy as the principal diagnostic technique to make systematic investigations have dealt with ohmically - and low power NI - heated plasmas which led to L-mode confinement /1,2/. Earlier, the behavior of OH-L-H plasma edge properties were described phenomenologically /3/. This paper quantifies ASDEX SOL n_e-profiles in the outer midplane during the L-H phases of high NI power ($P_{NI} > 2.4$ MW) diverted discharges sustained by gas puffing. Emipirical scaling relationships for n_s and λ_n for ohmic and low P_{NI} conditions are introduced as well. The stainless-steel walls of the vacuum vessel were neither carbonized nor gettered for these discharges.

2. Temporal Characterization of an H-Mode Plasma

Figure 1 exhibits the characteristic signatures of an H-mode discharge in ASDEX. Initiation of NI leads to a gradual decrease in $\bar{n}_e$, accompanied by a smooth transition in λ_n from 2.15 cm during OH to about 2.85 cm at t_{NI} = 30 ms. λ_n then slowly decreases to about 2.5 cm before entering into the H-phase through a rapid successive series of ELMs (which are not resolved on the D_α trace). At the conclusion of the first distinct ELM, λ_n and n_s have reached values of ~ 1.1 - 1.3 cm and $1.3 \times 10^{13}/cm^3$ respectively, which are maintained throughout the discharge irrespective of the values of $\bar{n}_e$ and $\beta_p + li/2$. Termination of NI reverses the train of events seen at the beginning.

Precursor phenomena in the SOL density profiles are not observed either for the L-H transition or for ELMs. Further, Fig. 1 illustrates that measurements made within 200 µs before an ELM reveal the same λ_n, n_s values as a few ms after the ELM. During the event, an ELM induces a density depletion of the peripheral plasma which is mirrored by a strong density increase in

the SOL and a clamping of $\bar{n}_e$. Typically, λ_n increases from ~ 1.3 cm to greater than 5 cm in less than 200 μs. The decay of the SOL density back to the pre-ELM state occurs with an exponential time constant of ~ 0.5 ms. These features are qualitatively illustrated by Fig. 2 which is a 3-D plot of the Li [2p - 2s] light intensity along the probing beam. (At low densities this intensity is proportional to n_e. At high densities, e.g. near the separatrix, this proportionality breaks down, so that n_e increases faster than the light intensity).

Density profiles (derived from Li [2p - 2s] profiles - see /1,3,4/ for diagnostic details) for the OH, L and initial H-phase are presented in Fig. 3a as a function of distance from the separatrix radius R_s. As already apparent from Fig. 1, $n_s(H) > n_s(OH) > n_s(L)$, and $\lambda_n(L) > \lambda_n(OH) > \lambda_n(H)$. Further, the shoulder over the region $5.5 > R - R_s > 2.5$ cm - briefly discussed in /1/ - is present in all phases. The $n_e(H)$ profile near the separatrix is virtually invariant during the entire H-phase, as documented by Fig. 3b and by the near-constancy of $\lambda_n(H)$ in Fig. 1. This result is particularly striking, given that R_s (determined from magnetic signals) has varied over a two cm range in magnitude as a consequence of the β_p increase and plasma position control. Finally, from other discharges where the inner region is better examined, it is found that the steep density gradient in the SOL associated with the H-mode continues inside the separatrix.

3. Parametric Characterization of NI-Heated Plasmas

Since the scalings for n_s and λ_n depend upon the plasma mode, and hence P_{NI}, this section is divided into two categories, corresponding to low and high P_{NI}.

3.1 Low-Power NI ($P_{NI} < 1.7$ MW)

Two shot series are considered: one in He^{++} ($\bar{n}_e$, P_{NI} are scanned) and one in D^+ ($\bar{n}_e$, P_{NI} and I_p are scanned). Non-linear regression fits of n_s and λ_n to functionals of the form $n_e^\alpha I_p^\beta P_{tot}^\gamma$ have been carried out, and are plotted in Figs. 4 and 5. The lines through the experimental points represent the best linear fit of n_s and λ_n to their respective functionals.

For D^+ (Fig. 4): $n_s(OH) = 0.052\ \bar{n}_e^{1.0 \pm 0.09}\ I_p^{0.25 \pm 0.15} + 0.234$ $[10^{13}/cm^3, kA]$ with a correlation coefficient R = 0.93;
$n_s(L) = 7.024\ \bar{n}_e^{0.97 \pm 0.13} / I_p^{0.5 \pm 0.2} + 0.009$ with R = 0.92; and
$\lambda_n(OH + L) = 104\ P_{tot}^{0.19 \pm 0.02} / \bar{n}_e^{0.22 \pm 0.04}\ I_p^{0.61 \pm 0.07} - 0.108$
$[cm, MW, 10^{13}/cm^3, kA]$ with R = 0.93.

For He^{++} (Fig. 5): $n_s(OH) = 0.215\ \bar{n}_e + 0.17$ with R = 0.997;
$n_s(L) = 0.348\ \bar{n}_e - 0.102$ with R = 0.996; and
$\lambda_n(OH + L) = 3.23\ P_{tot}^{0.16 \pm 0.04} / \bar{n}_e^{0.22 \pm 0.03} - 0.148$ with R = 0.9.

Common to He^{++} and D^+ is the absence of an $n_s(L)$ dependence on P_{NI}. Of course, I_p does not appear in the He^{++} scaling, since it was held constant at 420 kA. The forefactors in the $n_s(He^{++})$ scalings are reproduced by the $n_s(D^+)$ formulas, using I_p = 420 kA. Also, the $n_s(OH, L)$ data of a D^+ series at I_p = 250 kA, discussed in /2/, is fitted by the $n_s(D^+)$ formulas well within the exponential error bars of I_p.

No edge Thomson scattering data was available to furnish an absolute calibration point for the series of relative n_e profiles produced by the Li-beam diagnostic. Hence, calibration experience from other discharges was drawn upon. This may introduce an absolute error as high as 0.1 - 0.2 x $10^{13}/cm^3$, affecting primarily the offset of the parametric fits. There should be little influence on the global systematic dependencies revealed by the regression formulas.

The regression formulas for λ_n (OH + L) are in complete accord with the λ_n(OH: D^+, He^{++}) values given in /1/. For example, using the relationship $P_{tot}(OH) = 0.326\ I_p^{1.2}$ from the D^+ data set, and setting $\bar{n}_e$ = 2.5 x $10^{13}/cm^3$, we obtain $\lambda_n(OH) \sim 1.33\ q_a^{0.38}$. This compares favorably to $\lambda_n(OH) = 1.3\ q_a^{0.35}$ derived from the D^+ data set of /1/. We further note that although $\lambda_n(He^{++}) > \lambda_n(D^+)$, both fits have the same parametric dependencies. λ_n can generally be determined to an accuracy of ± 0.1 cm on a relative basis within a shot, and to ±0.1 - 0.2 cm on an absolute basis.

3.2 High-Power NI (P_{NI} > 2.4 MW)

The eight discharges of this analysis were selected for their extremes in parameter space. Since they were carried out over a span of three years, and only some of the shots had Thomson scattering density calibrations

(e.g. see /5/), $n_s(OH) = 0.22\ \bar{n}_e$ is taken as a reasonable approximation for these discharges. Therefore, the scalings for $n_s(L, H)$ give only the relative behavior with respect to this assumed $n_s(OH)$ line.

In Fig. 6, the $n_s(L)$ points are taken at the time corresponding to the maximum $\lambda_n(L)$ (t_{NI} ~ 60 ms), and the $n_s(H)$ points within 20 ms after the L-H transition. The regression analysis of $n_s(L,H)$ on $\bar{n}_e$, I_p, B_t and P_{tot} yields: $n_s(H) = 0.523\ \bar{n}_e^{2.2} \pm 0.17 / P_{tot}^{2.5\pm0.36} + 0.047$ with R = 0.982; and $n_s(L) = 36.2\ \bar{n}_e^{1.55\pm0.22}/I_p^{1.0\pm0.33} + 0.038$ with R = 0.967. Single null discharges apparently can be characterized in the same fashion as those with a double-null (DN) divertor. As in the case of low-P_{NI} discharges, there is no correlation of $n_s(L)$ with P_{tot}. However, now $n_s(L) \leq n_s(OH)$. Excluding I_p as a variable gives $n_s(L) = 0.21\ \bar{n}_e - 0.028$ (R = 0.89). Or, retaining I_p as a variable, but excluding one particular data point of the eight, yields $n_s(L) = 0.19\ n_e^{1.07\pm0.1} + 0.03$ (R = 0.967). Thus to first order, the ratio $n_s/\bar{n}_e$ remains fairly constant up to this phase of the discharge. (Remember that $n_s = 0.22\ \bar{n}_e$ is the assumed OH scaling.) $n_s(H)$ exhibits an exceptionally strong dependence on $\bar{n}_e$ and P_{tot}. $n_s(H)$ is greater than $n_s(OH)$ for large $\bar{n}_e^{2.2}/P_{tot}2.5$ - as for shot # 9630 of Figs. 1 - 3 ($\bar{n}_e = 3.67 \times 10^{13}/cm^3$, $P_{tot} = 2.32$ MW, $B_t = 21.7$ kG, $I_p = 315$ kA) - and $n_s(H)$ is less than $n_s(OH)$ at the lower left of Fig. 6 (corresponding to $\bar{n}_e = 1.75 \times 10^{13}/cm^3$, $P_{tot} = 2.47$ mw, $B_t = 16.7$ kg and $I_p = 221$ kA).

For the present data set, no convincing correlations of $\lambda_n(L,H)$, nor even $\lambda_n(OH)$, with the global plasma parameters were discovered. Evidently, some unknown factors also influence λ_n, and are more likely to become noticeable if data is gathered over a long time period, rather than from a tightly controlled series of one day. Relatively speaking, one finds: $\lambda_n(L)/\lambda_n(OH)$ ~ 1.3 ± 0.27 and $\lambda_n(H)/\lambda_n(OH)$ ~ 0.7 ± 0.12, with SN discharges exhibiting the smaller values of $\lambda_n(L)$. $\lambda_n(H)$ ~ 1.0 - 1.4 cm.

The steep density gradient around the separatrix in the H-phase implies that any uncertainty in the position of the separatrix leads to a large uncertainty in n_s. The excellent overlap of n_e profiles in Fig. 3b attests to the reliability of the relative movements of R_s as determined from magnetic signals. (The relative error bars in the n_e profiles are on the order of a few percent). The absolute value of R_s (from magnetics) is known to within ± 1 cm. Using pressure constancy along field lines, one finds for shot

9630 that the R_s deduced in this manner is larger than the magnetic R_s by 0.3, 0.6 and 0.7 cm for the OH, L, and H-phases, respectively /6/. Other preliminary experimental evidence also points to an R_s greater than that computed from magnetics /7/. Thus, it is likely that all n_s scalings presented here are actually for a radial position slightly inside the separatrix.

4. The Effect of an Altered Divertor Configuration on the SOL

The ASDEX divertor configuration has been modified to tolerate higher thermal loads. These mechanical changes have altered gas recycling conditions such that the external gas puff (GP) rate required to sustain a given density is reduced /8/. As a result, the energy confinement time τ_E, which previously saturated above $\bar{n}_e \sim 3 \times 10^{13}/cm^3$ in ohmic discharges, continues to increase with $\bar{n}_e$, provided the gas puff rate is low /9/. Fig. 7 illustrates the behavior of n_s and λ_n during the $\bar{n}_e$ ramp-up (high GP) and plateau (low GP) phases of such a discharge: n_s initially increases in proportion to $\bar{n}_e$, but begins to decay as soon as the GP rate is throttled back by the density feedback control system to a level necessary to maintain $\bar{n}_e$ at the pre-programmed value of $\bar{n}_e \sim 5 \times 10^{13}/cm^3$. Concurrently with the n_s decrease, the n_e profiles of the main plasma begin to peak - as shown by the $\bar{n}_e(0)/\bar{n}_e(30)$ trace of Fig. 7, ($\bar{n}_e(r)$ is a chord density) - and τ_E begins to rise /9/. λ_n varies slightly over ~ 1.5 -1.7 cm.

With the old divertor configuration, n_s(OH) was strictly proportional to $\bar{n}_e$. Changing recycling conditions has allowed ASDEX to access a region of Improved Ohmic Confinement (IOC), and has made evident that the GP rate can be an important variable in determining n_s. Note that all SOL scalings presented here, and in the past, were derived for machine conditions permitting only Saturated Ohmic Confinement (SOC).

5. Discussion

Common properties of all $n_s(L)$ scalings are: (a) the lack of a correlation with injected power, and (b) a decrease of $n_s(L)$ with increasing current. That the exponents of I_p take on different values of -1 (high P_{NI}), and -0.5 (low P_{NI}) is probably not significant: The high-power scaling is forced by one data point; removal of this point leads to $n_s(L) \propto n_e^{1.07}$.

The low-power $n_s(L) \propto I_p^{0.5}$ scaling may be regarded as being better founded: (a) the data base is larger, and (b) the formula for D^+ is able to predict the scalings derived for two other series of discharges carried out at 420 kA in He^{++} and at 250 kA in D^+.

For ohmic heating, $n_s(OH) \propto \bar{n}_e I_p^{0.25}$. Again, since the formula for D^+ can predict the OH-behavior for the 420 kA/He^{++} and 250 kA/D^+ series mentioned above, some degree of confidence may be placed in the expression. Moreover, it is intuitively reasonable that n_s augments with I_p, since the main plasma density profile is known to broaden with I_p, e.g. from /10/, one can deduce $n_{eo}/\langle n_e \rangle \propto I_p^{-0.5}$. Further, $n_s(OH)$ being directly proportional to $\bar{n}_e$ simply means that the global density profiles exhibit self-similarity in the parameter $n_s/\bar{n}_e$.

In like manner, with NI-heating the density profiles are self-similar in $n_s/\bar{n}_e$. The significant features are: (a) at low P_{NI}, $n_s(L)$ is greater than $n_s(OH)$ over most of the $\bar{n}e$ range, whereas, (b) at high P_{NI}, $n_s(L) \approx n_s(OH)$. The inverse dependence of $n_s(L)$ on I_p may not be interpreted as a global peaking of the density profile; $n_{eo}/\langle n_e \rangle$ also decreases with increasing I_p in the presence of neutral injection.

The regression formula $n_s(H) \propto n_e^{2.2}/P_{tot}^{2.5}$ is unique in that the absorbed heating power enters strongly, and is independent of the plasma current. Of equal importance, the expression has validity only for the initial part of the H-phase. Beyond the H-phase onset, $n_s(H)$ remains largely independent of the temporal evolution of $\bar{n}e$. As with $n_s(L)$, there is no correlation with B_t.

The expressions for $\lambda_n(OH + L)$ for He^{++} and D^+ have the same weak parametric dependences on $\bar{n}e$ and P_{tot}. Thus, the absence of an isotope effect, as far as the exponents are concerned, is indicated. However, this may be fortuitous. Inclusion of an I_p scan for He^{++}, or a B_t scan for both, could well lead to slightly different exponents. Certainly, $\lambda_n(He^{++})$ is greater than $\lambda_n(D^+)$. From /1/ we may expect that q_a is the dominant scaling parameter, as opposed to I_p or B_t separately. Finally, an interesting aspect is that λ_n can be described by a single formula for ohmic- and low-power NI-heated plasmas.

In conclusion, the importance of recycling on the SOL properties has been emphasized through an example where $n_s(OH)$ is closely related to the external gas puff rate (IOC conditions), rather than to $\bar{n}_e$ (SOC conditions). Therefore, all results above must be regarded as a special subset for which SOC conditions prevailed, where no strong coupling to the GP rate existed other than through $\bar{n}_e$.

REFERENCES:

/1/ K. McCormick, Z.A. Pietrzyk, et al., J. Nucl. Mater. 145-157 (1987) 215.

/2/ K. McCormick, Z.A. Pietrzyk, et al., 14th EPS Conf. on Contr. Fusion and Plasma Physics II (Madrid, 1987) 666.

/3/ K. McCormick, H. Murmann, El Shaer, J. Nucl. Mater. 121 (1984) 48.

/4/ K. McCormick, Rev. Sci. Instr. 56 (1985) 1063.

/5/ H. Murmann, M. Huang, Plasma Phys. 27 (1985) 103.

/6/ K. Lackner, et al., Proc. 10th IAEA Conf. on Plasma Physics and Controlled Fusion Research I (London, 1984) 319.

/7/ Max-Planck-Institut für Plasmaphysik Annual Report (1986) 23.

/8/ G. Haas, W. Poschenrieder, et al., this conference

/9/ E.R. Müller, F.X. Söldner, et al., 15th EPS Conference on Controlled Fusion and Plasma Physics I (Dubrovnik, 1988) 19.

/10/ G. Gehre, et al., 13th EPS Conf. on Contr. Fusion and Plasma Physics, I (Schliersee, 1986) 220.

Figure Captions:

FIG. 1: Temporal behavior of $\beta p + l_i/2$, $\bar{n}_e$, the D_α light intensity of the divertor plasma, the separatrix density n_s, and the density e-folding length λ_n in the SOL during and after NI. $H^\circ \rightarrow D^+$, 2.8 MW. B_t = 2.17 KG, I_p = 315 kA.

FIG. 2: 3D plot of the Li [2s - 2p] light intensity along the beam over the time span 1.209 - 1.22 sec, encompassing two ELMs.

FIG. 3: SOL density profiles for the discharge of Fig. 1 during the (a) OH-L-H phases, and (b) H-phase over the NI time span.

FIG. 4: $H^0 \rightarrow D^+$ with P_{NI} = 0.41, 0.83, 1.67 MW (1, 2, and 4 NI sources); P_{tot} = 0.24 - 1.69 MW;
$\bar{n}_e$ = 1.8 - 2.3, 3 - 4.2 x 10^{13} cm^{-3};
I_p = 270, 320, 370, 420 kA;
B_t = 21.8 kG (a) Separatrix density n_{s13} $[10^{13}/cm^3]$ vs. the regression parameter fit for OH-(scales at bottom and on the right) and L-phases (left and top scales), (b) λ_n vs. the parametric fit for the combined OH- and L-phases.
$\bar{n}_e$ $[10^{13}/cm^3]$, I_p [kA], P_{tot} [MW].

FIG. 5: $H^0 \rightarrow He^{++}$ with P_{NI} = 0.41, 0.88 and 1.24 MW (1, 2 and 3 sources); P_{tot} = 0.5 - 1.5 MW; I_p = 420 kA, B_t = 21.8 kG
(a) n_s vs. $\bar{n}_e$ during OH and NI
(b) λ_n vs. the parametric fit for the combined OH- and L-phases.

FIG. 6: n_s vs. the parametric fit for the L- (bottom scale) and H-phases (top scale).
$H^0 \rightarrow D^+$ with P_{NI} = 2.4 - 3.4 MW; $P_{tot}(H)$ = 2.0 - 3.0 MW; $\bar{n}_e$ = 1.8 - 5 x $10^{13}/cm^3$;
I_p = 220 - 415 kA and B_t = 16.7 - 25.1 kG. SN, DN = single- or double-null divertor operation.

FIG. 7: Temporal behavior of n_s and λ_n during the $\bar{n}_e$ ramp-up and plateau phase of a discharge with the new divertor configuration, as well as the gas puff rate (GP) and the density peaking factor.

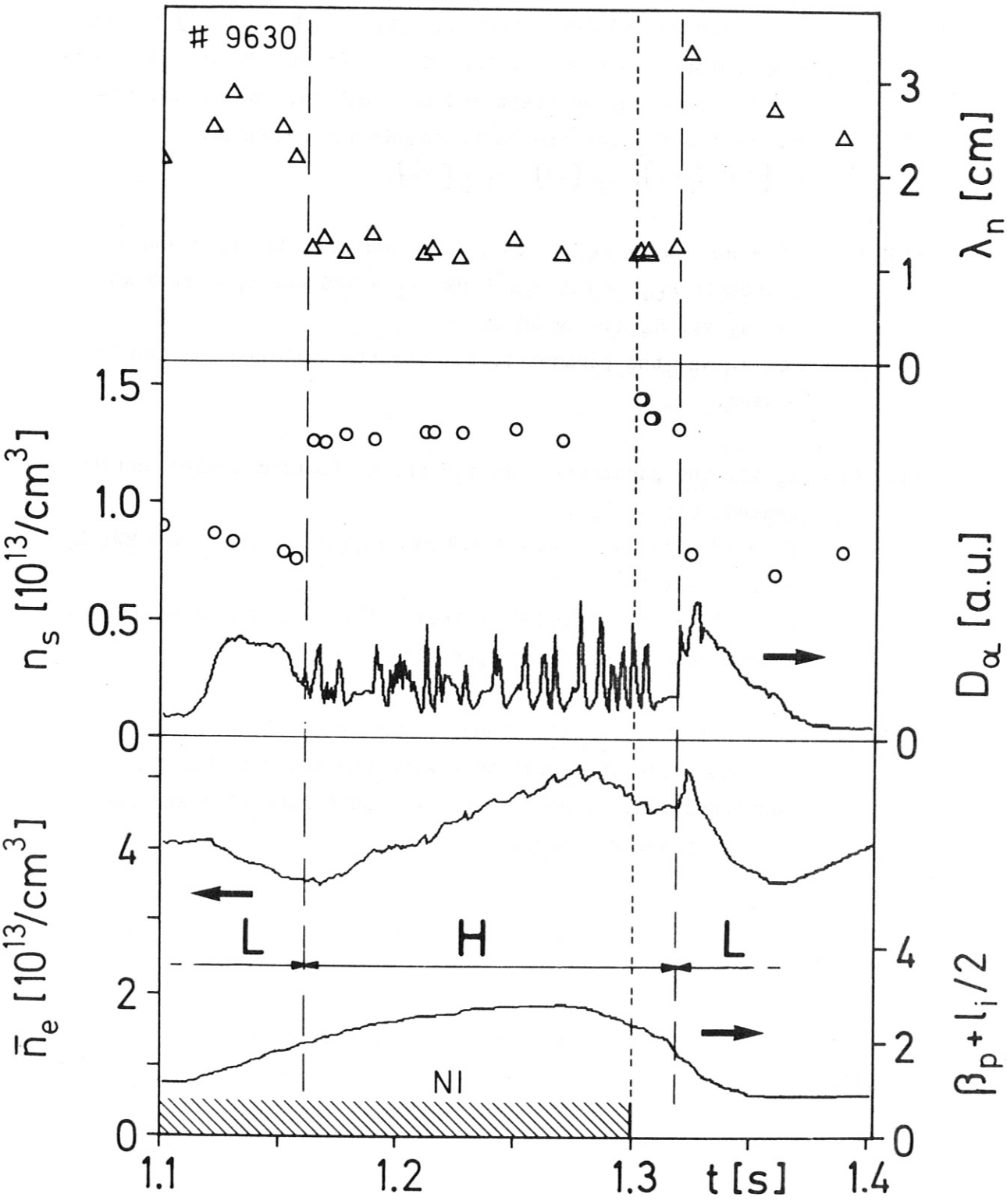

IPP 3 MCC 563 - 88

Fig. 1

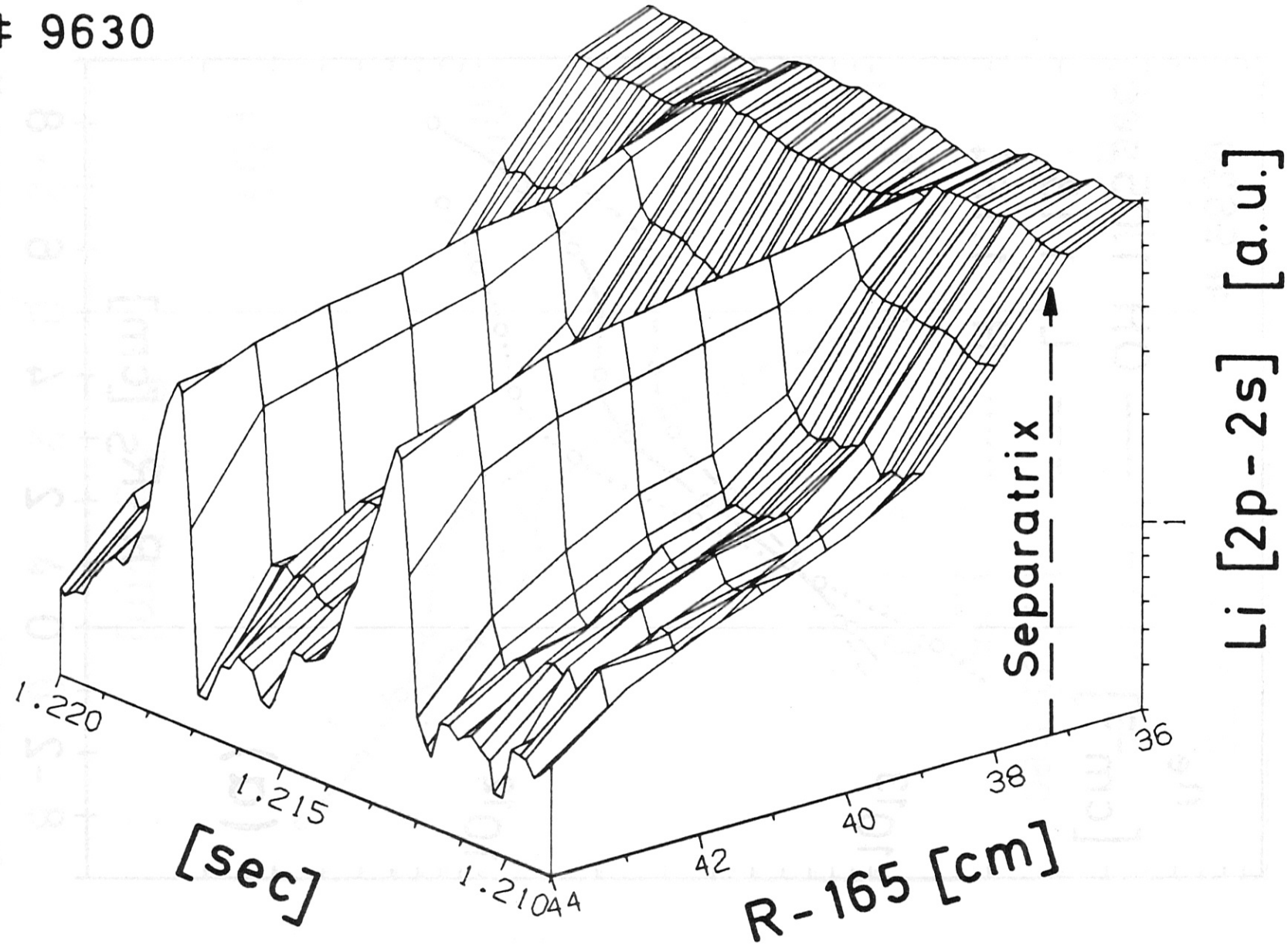

Fig. 2

IPP 3 MCC 564 - 88

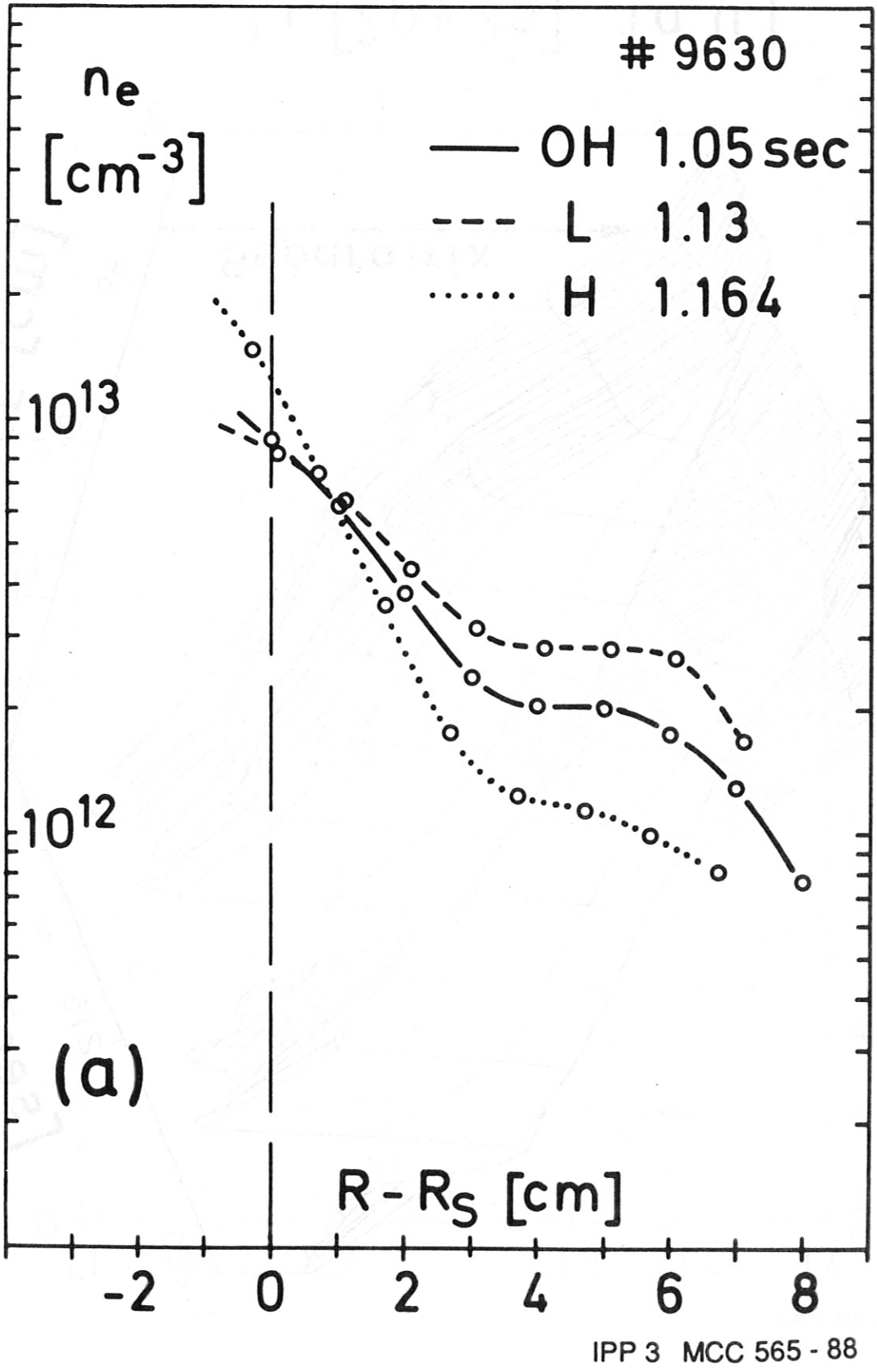
n_e
[cm^{-3}]
9630
OH 1.05 sec
L 1.13
H 1.164
10^{13}
10^{12}
(a)
R - R_S [cm]
-2
0
2
4
6
8
IPP 3 MCC 565 - 88

Fig 3a

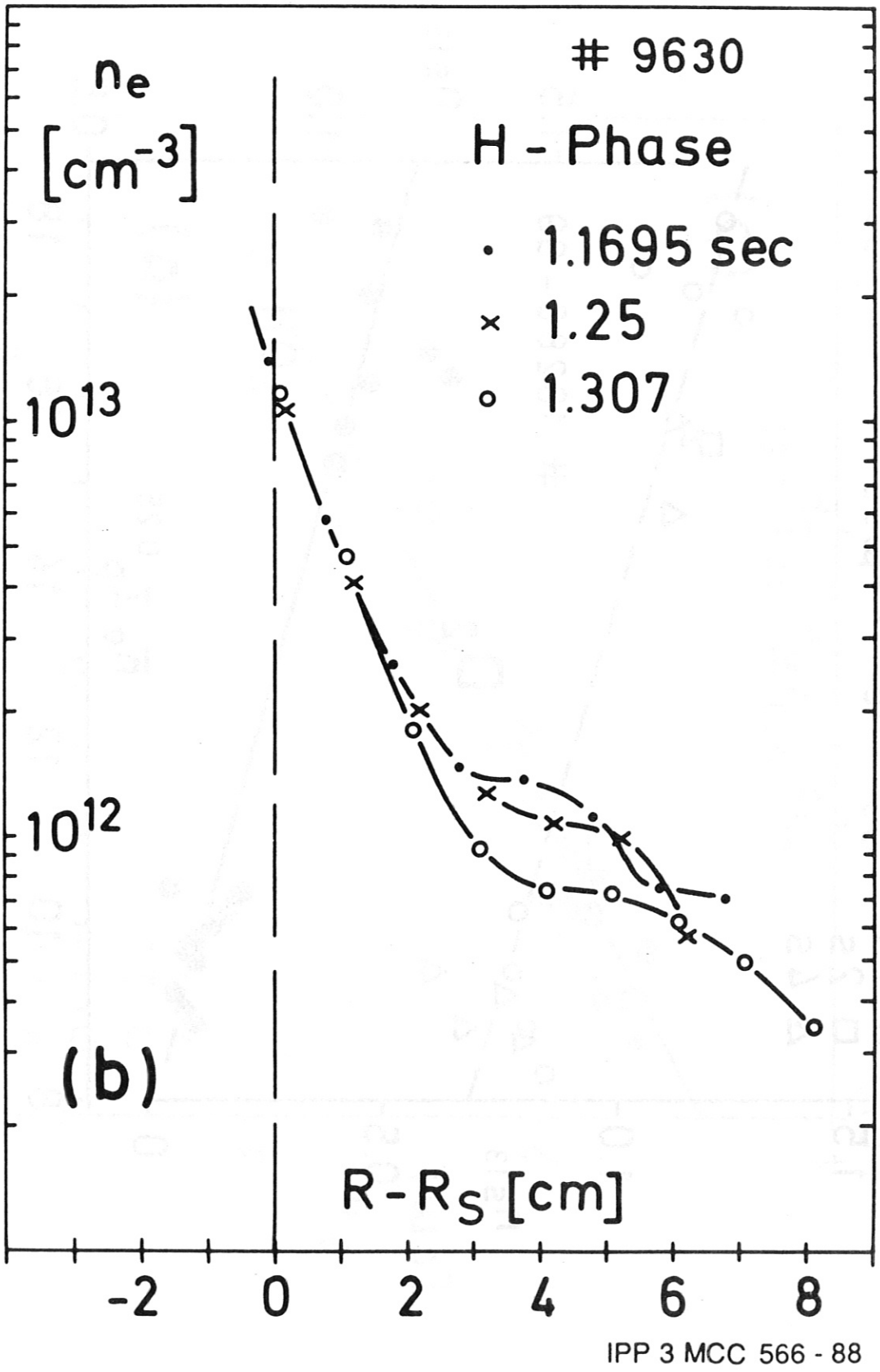
n_e
$[cm^{-3}]$
9630
H - Phase
• 1.1695 sec
× 1.25
○ 1.307
10^{13}
10^{12}
(b)
$R-R_S$ [cm]
-2
0
2
4
6
8
IPP 3 MCC 566 - 88

Fig. 3b

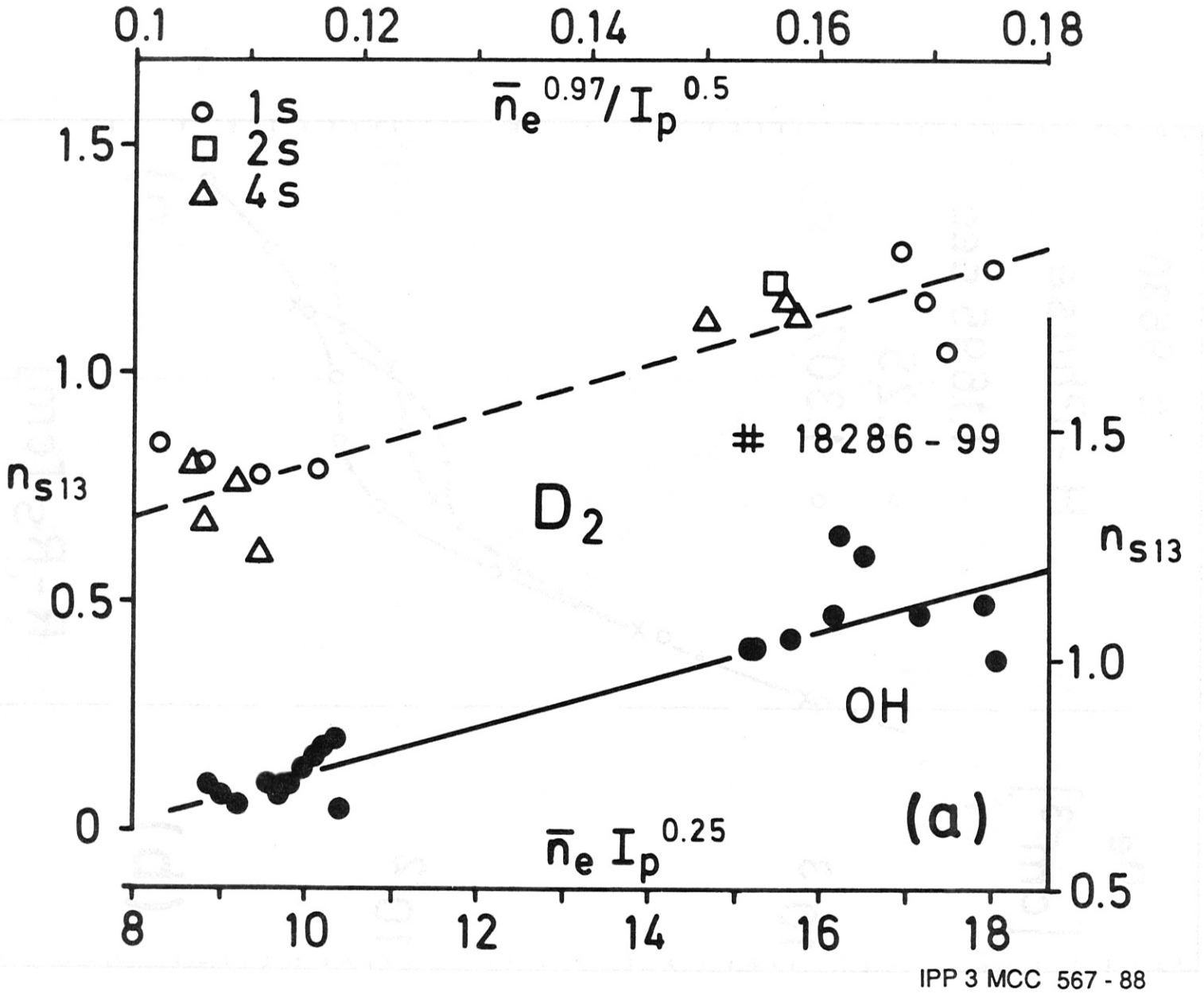
0.1
0.12
0.14
0.16
0.18
$\bar{n}_e^{0.97}/I_p^{0.5}$
1s
2s
4s
1.5
1.0
0.5
0
n_{s13}
18286 - 99
D_2
OH
(a)
$\bar{n}_e I_p^{0.25}$
8
10
12
14
16
18
IPP 3 MCC 567 - 88

Fig 4a

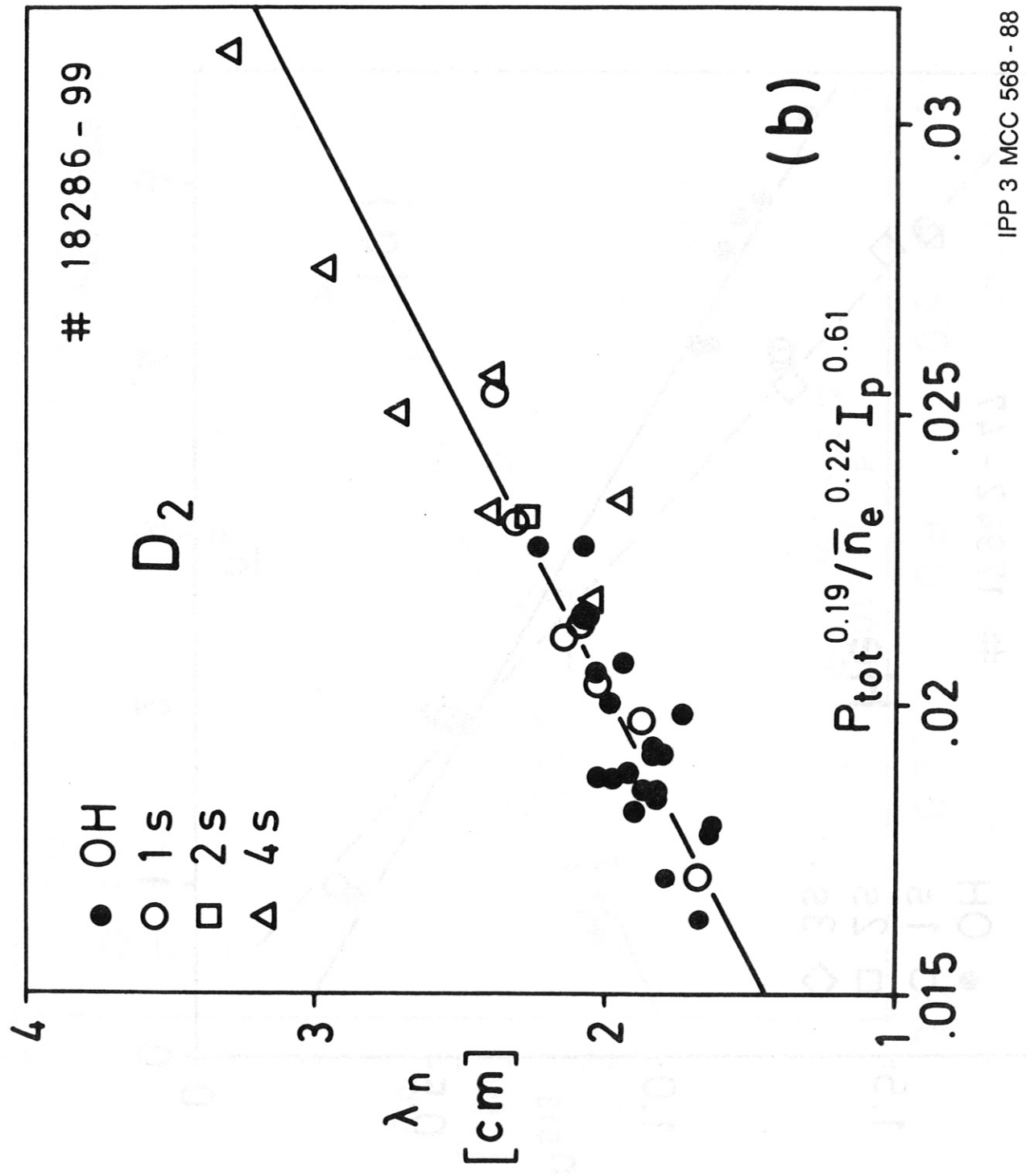

IPP 3 MCC 568 - 88

Fig. 4b

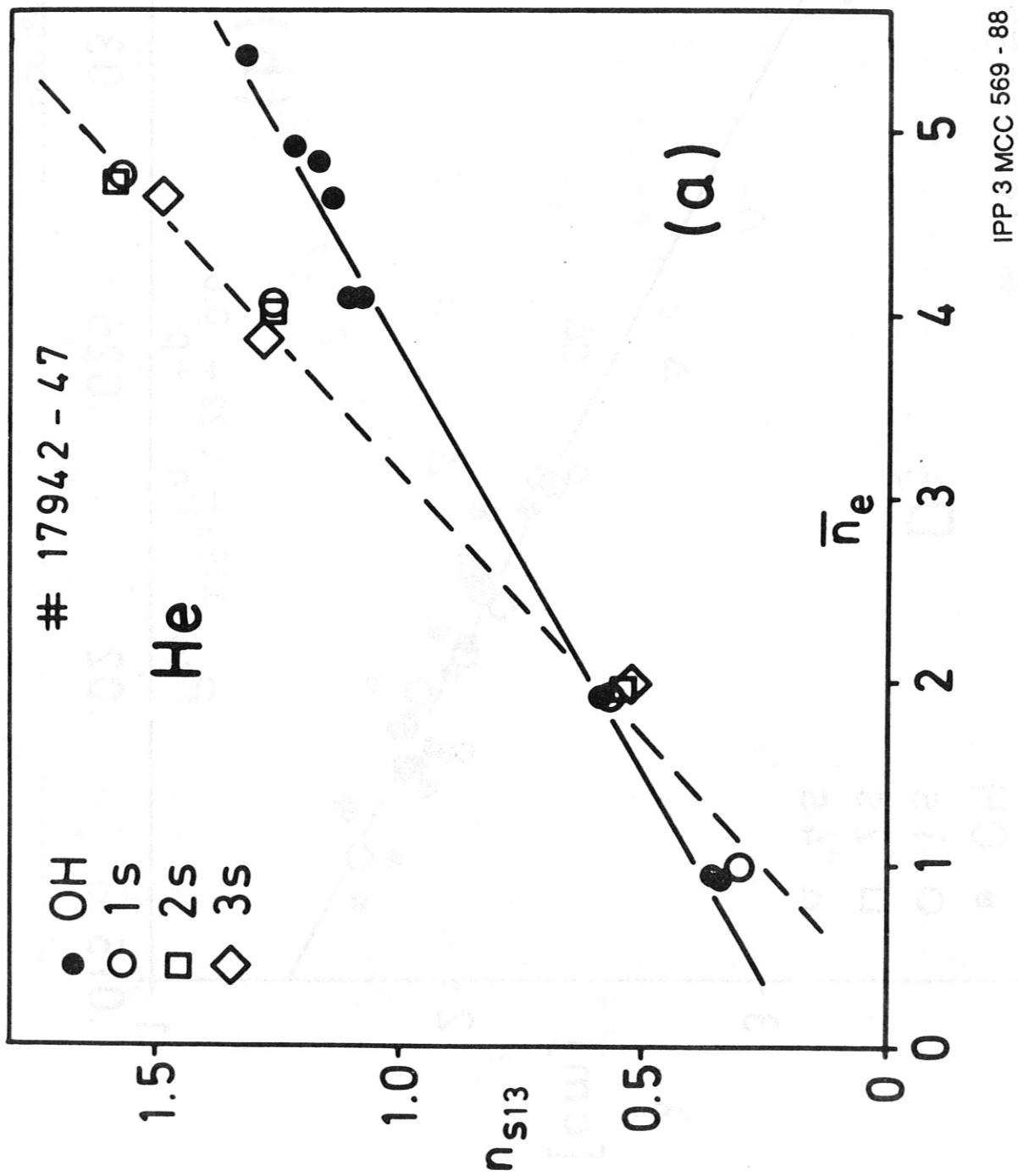
• OH
○ 1s
□ 2s
◇ 3s
He
17942 - 47
(a)
n_{s13}
$\bar{n}_e$
0
0.5
1.0
1.5
0
1
2
3
4
5
IPP 3 MCC 569 - 88

Fig.5a

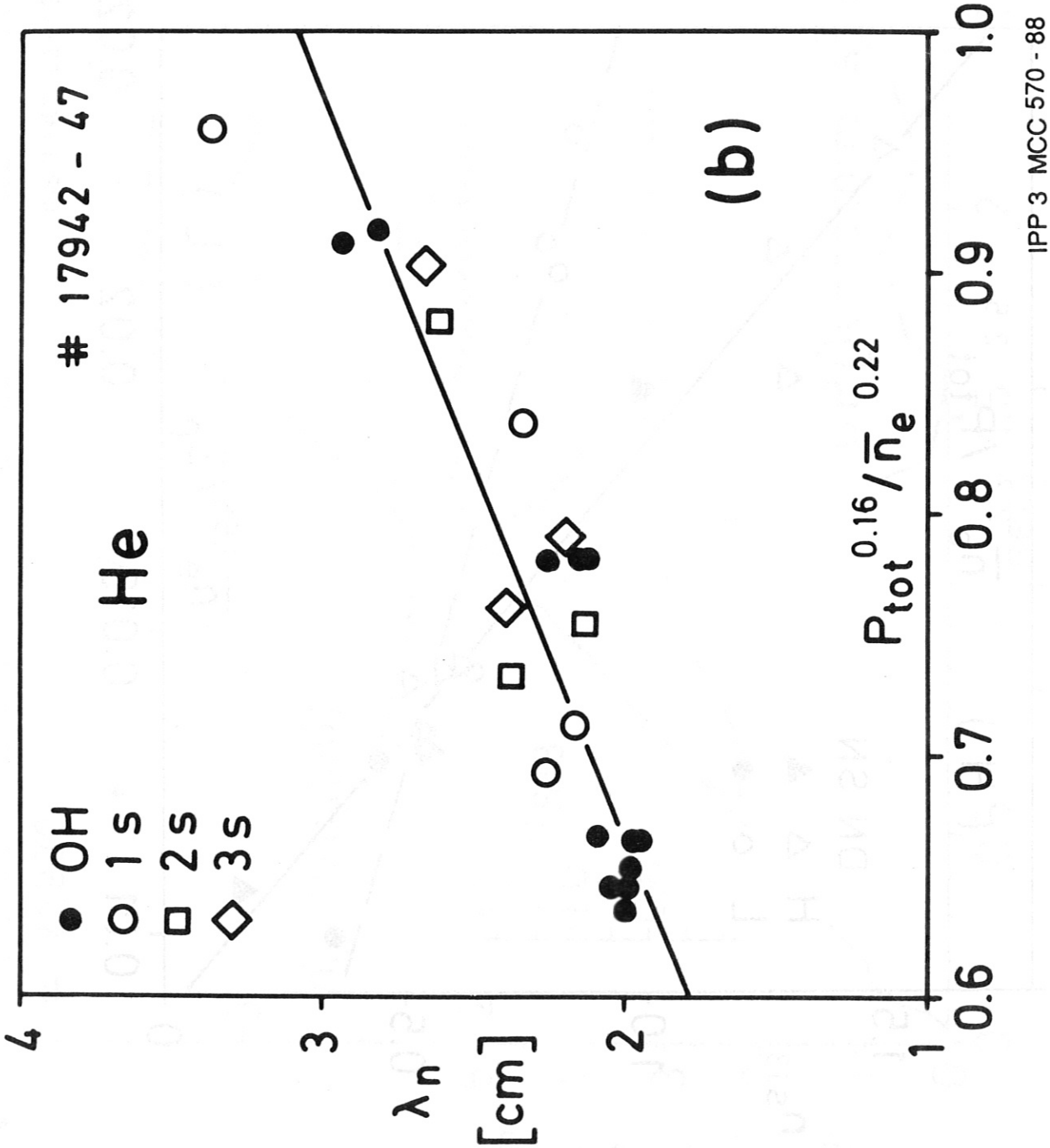
17942 - 47
He
(b)
OH
1s
2s
3s
λ_n [cm]
$P_{tot}^{0.16}/\bar{n}_e^{0.22}$
4
3
2
1
0.6
0.7
0.8
0.9
1.0
IPP 3 MCC 570 - 88

Fig. 5b

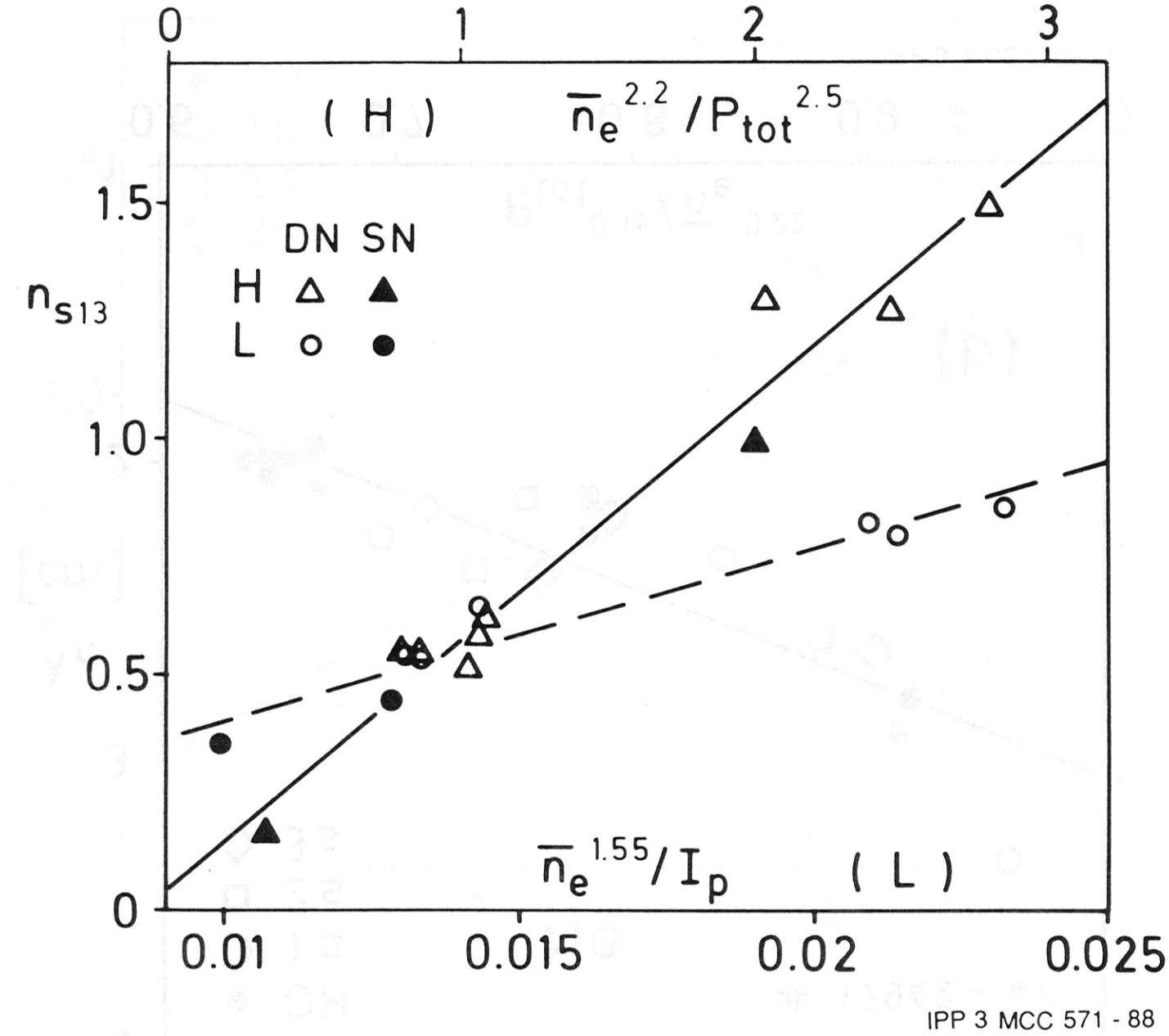
0
1
2
3
(H) $\overline{n}_e^{2.2}/P_{tot}^{2.5}$
1.5
1.0
0.5
0
n_{s13}
DN SN
H △ ▲
L ○ ●
$\overline{n}_e^{1.55}/I_p$ (L)
0.01
0.015
0.02
0.025
IPP 3 MCC 571 - 88

Fig. 6

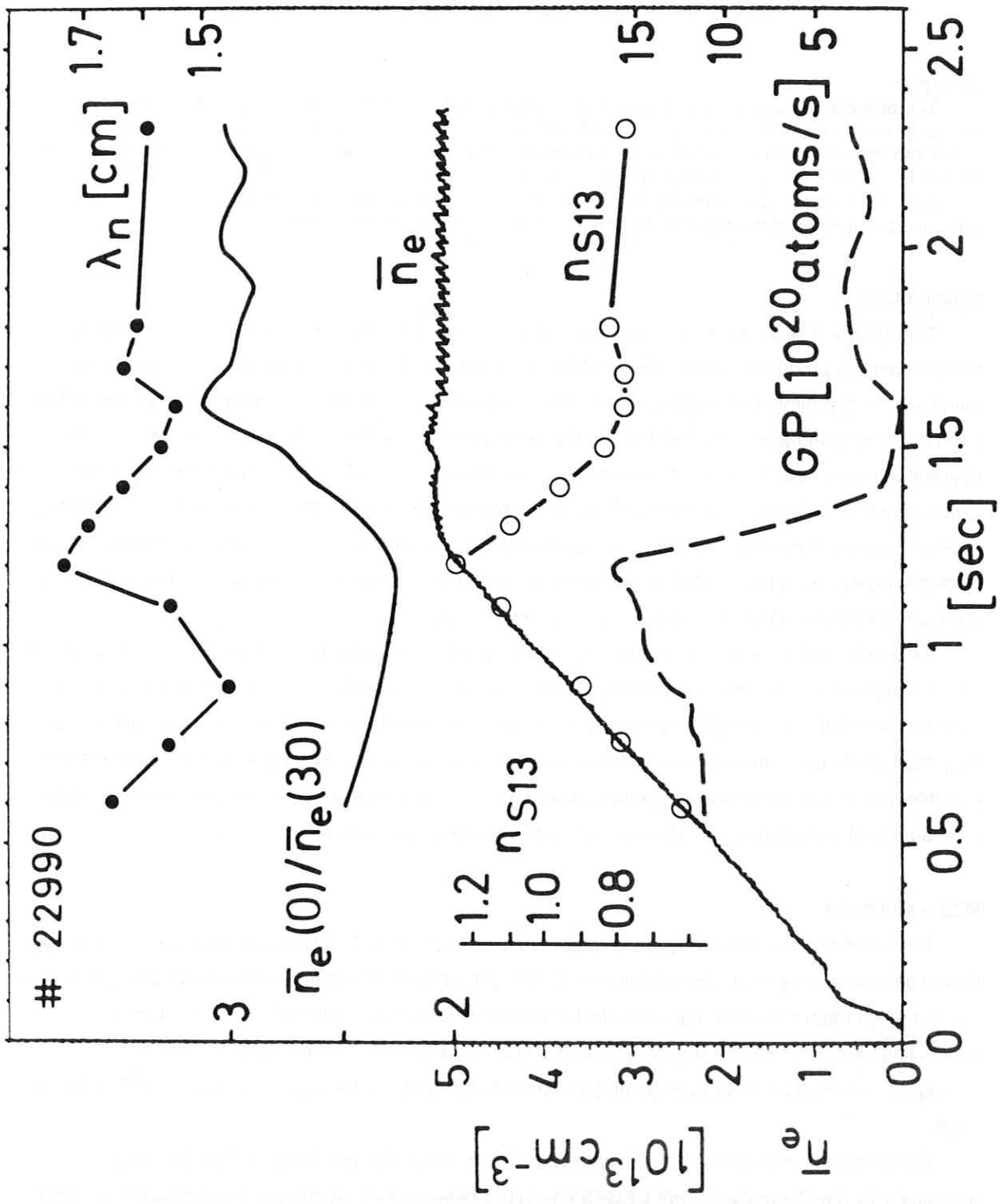

IPP 3 MCC 572 - 88

Fig. 7

Int. Workshop on PLASMA EDGE THEORY, Augustusburg (GDR), 26-30 April 1988
Proceedings to be publ. in CONTRIBUTIONS TO PLASMA PHYSICS (Akad.Verlag,GDR)

ASDEX Edge and Divertor Simulation and the Problem of Incomplete and Inaccurate Experimental Data

W. Schneider, J. Neuhauser, G. Haas, K. McCormick, N. Tsois, R. Wunderlich
Max-Planck-Institut für Plasmaphysik, D-8046 Garching, FRG

Abstract:

The one-dimensional hydrodynamic code SOLID coupled with the two-dimensional Monte Carlo neutral gas code DEGAS are used to simulate the scrape-off layer and divertor recycling region of the ASDEX tokamak. A numerical data base is created for the relevant parameter regime and compared to the limited amount of experimental data. A reasonable fit with ohmic data is obtained, assuming classical heat flow along field lines and allowing for varying divertor saturation. The problem of experimental errors on one side and deficiencies in the theoretical model on the other side are discussed.

Introduction:

The ASDEX divertor tokamak is running now since 1980 with ohmic and various external heating sources and has produced a large amount of data for a wide range of fusion relevant scenarios / 1 /. In parallel to the experimental program, analytical and numerical models for the edge and divertor region have been developed and applied to ASDEX, resulting in a qualitative understanding of the most prominent physical processes / 2, 3 /. A quantitative comparison is much more difficult, since the edge region is at least two-dimensional (with substantial three-dimensional perturbations), while the number and accuracy of the available edge and divertor diagnostics is still rather limited. In addition, no rigorous theoretical model for the edge plasma involving kinetic effects, electric currents and anomalous transport does exist as yet even in two dimensions and substantial simplifications are still required.

As an intermediate step, in the present paper we use the one-dimensional hydrodynamic code SOLID / 2 / together with the two-dimensional Monte Carlo neutral gas code DEGAS / 4 / to create a numerical data base for the ASDEX edge region by varying the power input, divertor pumping, etc. It will be shown that, despite of all the problems mentioned above, a simultaneous fit of various independent measurements is possible over a large parameter range. In turn, we can extract from these numerical solutions reasonable estimates for those parameters, which are difficult to measure experimentally.

Model and code:

The one-dimensional hydrodynamic scrape-off layer code SOLID / 2 / is used to describe the plasma flow and parameter variation along field lines. Classical fluid dynamics along field lines with different electron and ion temperatures is chosen and the electric current is set to zero. Optionally a non-local heat conduction model / 5 / can be selected. Cross field transport is not treated explicitly. Instead, a homogeneous sheath with an average perpendicular width as typical for experiment is used in the plasma code.

The neutral gas dynamics in the divertor chamber including the throat region is treated quite realistically by the Monte Carlo code DEGAS / 4 / in two dimensions (poloidal cross section). The required two-dimensional plasma input from SOLID is constructed by an approximate mapping procedure assuming a back-to-back exponential density and temperature profile across flux surfaces similar to the experimental one / 6 /. The source and loss terms calculated by DEGAS are then integrated radially and mapped back to SOLID. Usually three to four SOLID-DEGAS iterations are sufficient to get a stationary solution, the number of neutrals followed approaching one-thousand in the last iteration.

In spite of the obvious deficiencies of the plasma model compared to reality, this code package has a few attractive features. Especially, it relies on classical physics only, since anomalous plasma cross field transport is replaced by an experimental sheath width and no anomalous neutral effects are expected anyhow. As a consequence only very few free parameters remain for a stationary solution, e.g. the ion and electron power input across the separatrix and the divertor pumping (sticking coefficients). In addition, DEGAS provides a lot of useful output like divertor wall load and sputtering, which should only weakly depend on plasma details. For future applications SOLID may be optionally replaced by a two- dimensional multifluid code / 7 /, but the required interfaces are not yet written.

Results:

Typical ohmic ASDEX discharges with and without pellet injection have been used as initial experimental data base. As a guide line for the numerical parameter study, we used the experimental relation between midplane separatrix density n_s (to be fitted by SOLID) and neutral flux density Γ_0 (counted in molecules) in the divertor (a typical DEGAS quantity), where the former varied over one, the latter even over two orders of magnitude. A description of the corresponding experimental data and first numerical results for hydrogen are given in a recent pellet paper / 8 /. Since in the specific experiments deuterium was used, the measured neutral flux was multiplied by $\sqrt{2}$ as a first order correction for comparison.

Meanwhile, these simulations have been repeated and extended with deuterium and the conclusions obtained in / 8 / were confirmed. Figure 1 shows the original experimental deuterium data and selected numerical results for a specific parallel heat flux $q_{\parallel}=1.2*10^7$ Wm^{-2} as appropriate for high current, ohmic

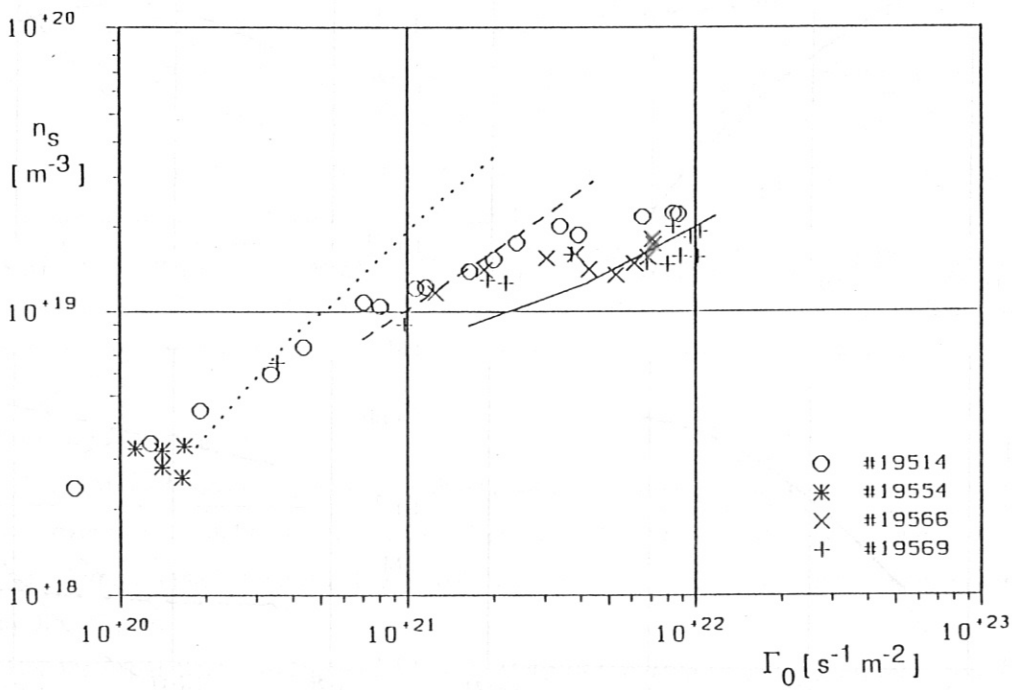

Fig. 1. Midplane separatrix density n_s as function of the neutral flux density Γ_0 in the divertor chamber (deuterium, $q_{\parallel}=1.2*10^7$ Wm^{-2}). Measured values for ohmic discharges (symbols) are compared to simulations for fixed power input, but varying atom and molecule sticking factors (..... .5, .1; _ _ _ .3, .03; ___ .01, .02).

ASDEX discharges and three different divertor pumping rates. In fact, a comparison with figure 15 in / 8 / practically yields coincidence, if the abscissa is shifted by $\sqrt{2}$. The intersections between the experimental data band and the calculated curves indicate that low midplane separatrix densities correspond to strong divertor pumping, while high densities coincide with nearly saturated divertor walls.

Apart from experimental and theoretical errors to be discussed later on, there is no further freedom for adjustment and therefore all other data calculated should fit with experiment also (including errors, they can in turn be used to optimize the fit). In figure 2, we show a variety of such quantities as function of the same Γ_0. Transferring the intersection regions from figure1 into all graphs of figure 2 (indicated by the thick dashed line), we may predict values for each parameter and compare with measured ones , e.g. from

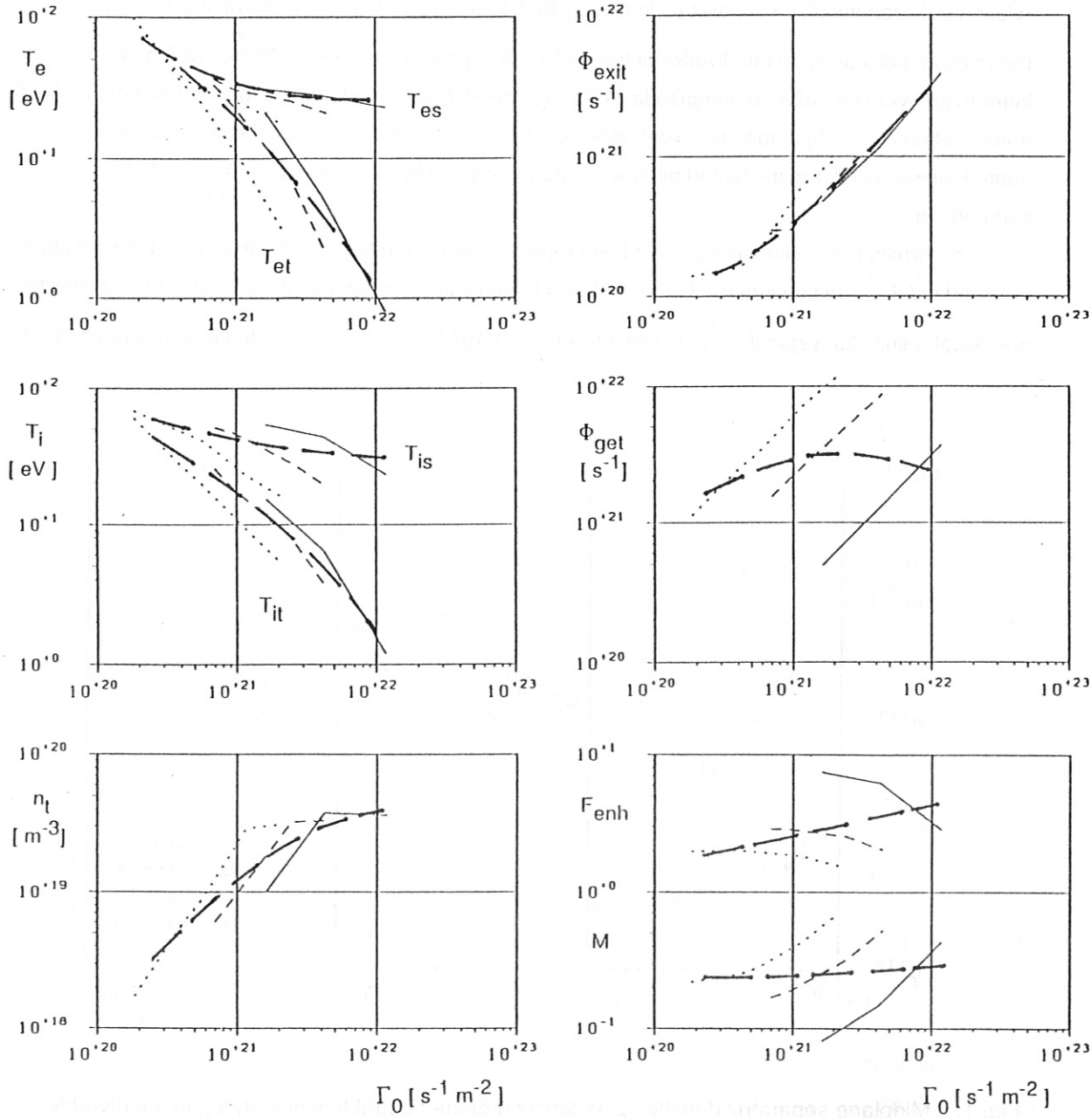

Fig. 2. Various edge and divertor quantities are shown for the same simulation runs as in fig.1, again as function of Γ_0. The intersection points between experimental and theoretical curves in fig.1 are transferred to fig.2 and connected by the thick, dashed line.

Langmuir probes / 9 / or edge laser scattering. In fact, the mid plane and target electron temperatures, T_{es} and T_{et}, and the divertor density n_t are close to the observed ones except probably for the lowest densities, where at least the divertor electron temperature is too high. Since the mean free path of heat conduction electrons becomes comparable to the field line length in this regime, the non-local heat conduction model was activated as alternative. The fit, however, turned out to be worse and partly no stationary solution was obtained, while at higher densities the local and non-local model converge anyway. Probably the effective energy flux limit introduced by the specific non-local model is too stringent.

The hydrogen ion temperature in the scape-off layer has not been directly measured. In addition, hot tail ions reported at low density / 10 / indicate deviations from a Maxwellian distribution, not included in a fluid model. In the simulation, the fraction of input power from the bulk plasma given to the ion channel (taken as 35 percent) influences the mid plane ion temperature T_{is} at low to intermediate density, but is not well-known in experiment.

There is also no direct measurement of particle fluxes and parallel flow velocity. We believe, however, that the DEGAS values derived from the above fit provide reasonable estimates e.g. for the neutral backflow Φ_{exit} from the divertor to the main chamber and the total gettering flux Φ_{get} (both in atoms/s for one outer divertor chamber), the sum of both being equal to the forward ion flux Φ_{D^+} into the divertor. However, the effective throat area derived from Φ_{exit} vs. Γ_0 turns out to be at the upper error limit of a rather indirect measurement / 11 /, and Φ_{get} (which includes bypass neutral fluxes in our model) is roughly twice the typical gas puff into the machine and would probably require some additional gas desorption at main chamber walls for explanation, even if the bypass flux is corrected for. This indicates that the calculated flux enhancement factor F_{enh} in the divertor (2....5) might be a lower limit and the calculated Mach number M at the throat ($\approx$ .25) an upper limit for the experimental value.

The DEGAS divertor sputtering output shows dominant ion sputtering at the target plate, which disappears when approaching the high density limit, where T_{et} is low. The neutral sputtering at divertor walls is usually substantially lower, but survives even close to the density limit. The suprathermal ion minority / 10 / might contribute also, but is not part of the model.

Meanwhile, a large numerical data base including additionally heated plasmas for the original ASDEX divertor chamber (as above) and the new, hardened divertor (for long pulse heating) has been created. Figure 3 shows a selection for the original geometry. Details must be given elsewhere.

Discussion and Conclusions:

As demonstrated above, a quite reasonable fit between our model and the nominal experimental data is obtained over a significant parameter range. Classical heat conduction seems to be appropriate, while remaining differences might be due to the simplified geometry in SOLID or a slightly wrong wall reflection model in DEGAS, etc.

Taking the experimental and numerical results of figure 1 and 3 as a basis, a few more conclusions may be drawn. Theoretical curves at constant divertor pumping are generally steeper than the measured ones. During a discharge the plasma density usually starts at low density and unsaturated divertor walls and evolves to some programmed plateau or the final density limit with increasing divertor saturation, the latter being obviously connected with the time integrated gas puff rather than with the instantaneous one / 11 /.

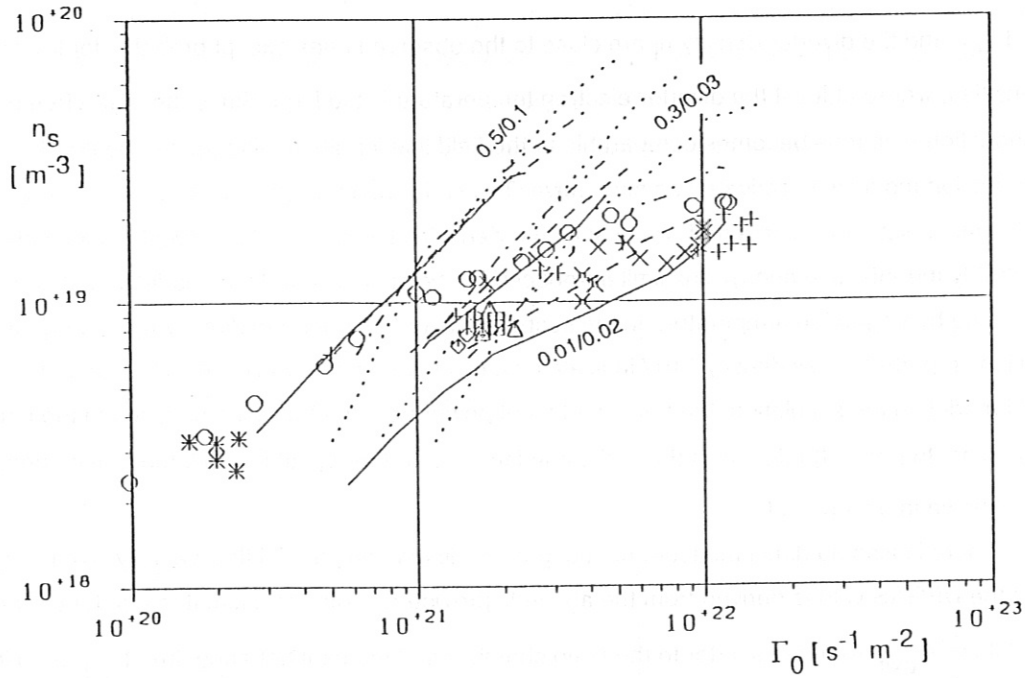

Fig. 3. Calculated midplane separatrix density n_s as function of the neutral flux density Γ_0 in the divertor chamber for different sticking coefficients (now indicated by numbers) as in fig. 1, but for four different power levels between ohmic and strong additional heating (___ $1.2*10^7$; _ _ _ $3*10^7$; _ . _ . _ $6*10^7$; ..... $12*10^7$ Wm^{-2}). The simulations are done with hydrogen in this case. The experimental points for ohmic and neutral injection are partly for deuterium, in which case Γ_0 has been scaled to hydrogen.

A similar result was reported from PDX / 12 /. This global picture picture suggests that the n_s <--> Γ_0 relation should not be unique in experiment even at constant power input to the edge, but depend on the specific discharge scenario. It is also important to note that, as in experiment and as predicted by analytical models / 13 /, the theoretical curves exhibit an upper edge density limit at given power and divertor saturation, determined by the recycling power limit ($T_{et} \approx 5eV$). Theoretically, this edge density limit can be improved moderately by raising the power or by increasing the divertor pumping (or bypass flux) and hence the total particle fluxes in the edge. The latter may, however, strongly influence central plasma confinement and enhance MHD activity, causing eventually discharge termination before the edge density limit is reached.

The fairly consistent picture outlined above must be checked with respect to errors and their impact on our conclusions. Deficiencies in the model were already discussed above, but the experimental problems are probably more severe. Apart from the unavoidable errors in existing diagnostics, the major points are uncertainties in the magnetic configuration, substantial poloidal and toroidal asymmetries together with the lack of sufficiently detailed measurements of the crucial parameters.

Specifically, the separatrix position in the equatorial plane is determined magnetically in ASDEX (and most other divertor tokamaks) with an accuracy of about ±1cm. Compared to radial e-folding lengths of temperature and density of the same order in the separatrix vicinity, this means a significant additional error for these values. Specifically, a firm decision between classical and flux limited heat flow along field lines becomes questionable, because the expected difference in T_{es} at low densities is comparable to the error. Since most parameters are expected to be continuous across the separatrix, a non-magnetic determination

is in principle difficult. A possible way out is to take the measured divertor plasma pressure near the separatrix, to assume Te≈Ti and pressure constancy along field lines and to determine the mid plane separatrix position from the radial pressure profile there / 5 /. A more direct separatrix determination relies on non-relativistic supra-thermal electrons, which are expected to flow to the target plate predominantly in a narrow layer close to the separatrix and are detected by Langmuir probes / 9, 14 /. There are, however, strong indications from non-axisymmetric target load in ASDEX, probably caused by suprathermal electrons during lower hybrid current drive / 14, 15 /, that the edge is slightly helical (deviation at least several millimeters) and even ergodized near the separatrix, making the combination of edge profile measurements at different toroidal positions doubtful in principle. The same is true with respect to the localized gas puff and the observed toroidal and up-down asymmetry of the divertor recycling, resulting in pressure variations in the scape-off layer, which may cause a complicated three-dimensional flow pattern. The local flow velocity, in turn, is one of the many edge quantities, which are difficult to measure even at easily accessible points.

Nevertheless, there seems to be a good chance for a reasonable, global understanding of the most prominent mechanisms governing the edge physics, using models like the one outlined above. A more detailed investigation not only requires much more elaborate numerical (eventually three-dimensional) models, but also a significant improvement of the number and quality of edge diagnostics. On the other hand, the crucial question of impurity generation and transport in the edge seems to depend strongly on these details, making edge physics a challenging item also in the future.

Acknowledgements: The authors wish to thank their collegues from the ASDEX team and THEORY 3 for many helpful discussion.

References:

/1/ M. Keihacker and the ASDEX-Team; Nucl. Fusion **25**,1045 (1985)
/2/ W. Schneider, D.B. Heifetz, K. Lackner, J. Neuhauser, D.E. Post, K.G. Rauh; J. Nucl. Mater. **121**,178 (1984)
/3/ Y. Shimomura, M. Keilhacker, K. Lackner, H. Murmann; Nucl. Fusion **23**,869 (1983)
/4/ D.B. Heifetz et al.; J. Comp. Phys. **46**, 309 (1982)
/5/ K. Lackner et al.; in Plasma Physics and Controlled Nuclear Fusion Research1984, Vol.1, IAEA, Vienna, p.319 (1985)
/6/ D. Heifetz et al.; 11th Europ. Conf. on Contr. Fusion and Plasma Physics, Europhysics Conf. Abstracts **7D**, 389 (1983)
/7/ M. Krech et al.; this conference
/8/ M. Kaufmann et al.; Nucl. Fusion (accepted for publication, 1988)
/9/ N. Tsois et al.; 14th Europ. Conf. on Contr. Fusion and Plasma Physics, Europhysics Conf. Abstracts **11D**, 658 (1987)
/10/ F. Wagner; Nucl. Fusion **25**, 525 (1985)
/11/ G. Haas et al.; J. Nucl. Mater. **121**, 151 (1984)
G. Haas et al.; J. Nucl. Mater. **145-147**, 519 (1987)
/12/ D.B. Heifetz et al.; J. Nucl. Mater. **121**, 189 (1984)
/13/ K. Lackner et al.; Plasma Phys.and Contr. Fusion **26(1A)**,105 (1984)
/14/ J. Neuhauser et al.; Bull. Am. Phys. Soc. **32**, 1839 (1987)
/15/ H. Rapp et al.; Proc. 14th Symp. on Fusion Technology, Avignon 1986, p.595

Comparison of Recycling in the ASDEX Divertor before and after Hardening

G.Haas, W.Poschenrieder, J.Neuhauser, S.Kaesdorf, ASDEX-Team, NI-Team
MPI für Plasmaphysik, Garching/FRG, EURATOM Association

Key words: ASDEX, poloidal divertor, recycling of hydrogen, fuelling

Abstract

The original ASDEX-divertor was not capable to dissipate the heat load of long pulse NBI and ICRH. In a partial reconstruction termed hardening, new water-cooled divertor components were installed. The modified divertor geometry resulted in some significant changes, e.g. in gas consumption and divertor pressure. Difficulties in obtaining a good H-mode are possibly connected to the modified recycling behaviour. However, a new regime with improved ohmic confinement (IOC) and reduced recycling is now found.

Introduction

The previous ASDEX-divertor design was not capable to withstand the high energy load of the extended heating pulses of the NBI and ICRH available now in ASDEX. The divertor plasma had been dumped on uncooled titanium collector plates and local melting had already occurred. Therefore, a new divertor was designed and installed in 1986. Its magnetic configuration was practically the same, while the chamber geometry, the cooling and the materials used were significantly changed. Fig.1 shows a comparison of the old and the new design. The new divertor not only has water cooled collector plates, but the total structure shielding the multipole coils against the plasma is water cooled. Moreover, this shielding structure now almost completely surrounds the divertor plasma, thus dividing the divertor volume into three subvolumes: the two inner volumes in front of the collector plates (Ia, Ib) and the outer volume (II). Owing to the design, there is some transparency of these shields resulting in a conductance for H_2 of about $1*10^5$ l/s between volumes (Ia +Ib) and volume II and of $3*10^5$ l/s between volume II and the plasma chamber. In the former divertor no separation in between the plasma fan and the divertor dome existed and the conductance to the main plasma chamber other than the divertor slits itself had been made small ($<10^5$ l/s) by closing off all openings (bypasses). The width of the divertor slits is now 3.6 cm which is narrower than before (6cm / 3.7 cm) and the H_2 slit conductance without plasma is about $1.2*10^5$ l/s for each divertor.
The pumping panels of the old divertor which provided a large area for Ti-gettering also had to be removed. In the new divertor Ti-gettering is now performed by simply

depositing Ti from Ti-balls onto the walls of volume II.

Results and discussion

Gas consumption and particle balance

One of the most obvious results with the new divertor was a drastic reduction by a factor of about 2 in the amount of fuelling gas required to build up and sustain the plasma. For a standard discharge ($\bar{n}_e = 2.9*10^{13}cm^{-3}$, $I_p = 320$ kA, $B_t = 2.17$ Tesla, $t_{FT} = 2$ sec) we now typically require 30 mbarl D_2, including the fuelling gas necessary for sustaining the plasma during the density flattop.
In fig. 2 we show this correlation by plotting the amount of gas necessary for building up the plasma versus the line average density for two discharges before and after hardening the divertor, respectively and we also compare this amounts of gas with the particle contents, which we find in the plasma and in the divertor volumes. The above mentioned reduction in the fuelling gas consumption is clearly seen. Furthermore, we find now typically 50 % (ohmic discharges) of the total gas puffed into the vessel in these volumes, in contrast to less than 20 or 30 % in the old geometry. This difference is plausibly explained by the more than ten times smaller surface area seen by the divertor plasma and bombarded by energetic hydrogen atoms (up to 50 eV) as compared with previous conditions. It is well known that atomic hydrogen has a high binding energy on all metal surfaces and can be released essentially by recombination. Thus, even in cases where no absorption of molecular hydrogen on metal surfaces is observed, strong reversible pumping of atomic hydrogen is found. Quite clearly, this is the cause of the large amount of fuelling gas missing in the particle balance during the discharge. As formerly shown /1/, a quantity of gas, equivalent to the missing part, is released in the first few minutes after a shot. This still holds true now at least for discharges without carbonized walls. However, in the new divertor with pumping capacity restricted according to the much smaller surface area in regions Ia and Ib, we reach kind of a saturation already during the plasma build up phase in contrast to the old configuration.
Another significant difference to the situation before is the very small effect on fuelling when Ti is evaporated. The amount of fuelling gas now shows almost no increase, whilst gettering in the old divertor would more than double the amount of gas required to sustain the plasma density. This is well in line with the explanation already given above. In the old divertor the fresh Ti surfaces were directly accessible to atomic hydrogen, resulting in a very high pumping speed. Now the gettering surfaces no longer see atoms and are restricted to pump molecular hydrogen, obviously, at much lower rate. However, a decrease in Z_{eff} is observed after gettering indicating a reduction of impurity gases (mainly of CO as observed during the discharge).

Exhaust and compression ratio

As a consequence of the high conductance between volume II and the plasma chamber and the conductance restrictions between volume (Ia, Ib) and volume II, the gas pressure measured in volume II is lower than ever before and its overlinear dependence on the plasma density is now less pronounced. Fig.3 shows a comparison of divertor pressures as a function of $\bar{n}_e$. Clearly, the new design has the smallest exhaust efficiency and compression ratio comparing the pressure measured in a port on the plasma chamber to that measured in the divertor.

There is still some difficulty in threading the plasma through the narrower divertor slits, because of the present, not yet optimised current distribution in the divertor coils. Fig.4 shows the divertor pressure as a function of the ratio of divertor coil current to plasma current. No maximum is obtained within the accessible range of parameters, as was formerly the case. This leads to enhanced recycling at the divertor throat aperture, which renders the compression ratio more susceptible to plasma position and plasma current. At high plasma currents and probably smaller scrape-off layer width the divertor pressure increases and approaches the values of the old divertor with "wide slits and bypasses".

Gas desorption due to additional heating

The fact, that the divertor plasma is now surrounded by surfaces, which are saturated with hydrogen nearly during the whole shot, has not only consequences for the gas puff demands. It causes strong bursts of gas desorption every time the heating power is increased. As an example we show in fig.5 the development of the neutral particle density during NBI in volume Ia and II. In this case a NBI power of 1.35 MW was applied. The neutral density in volume Ia rises immediately by a factor of nearly 20. Due to the much larger outer divertor volume, however , the slower increase of the neutral density in volume II by a factor of about 2 is more important for the particle balance. It turns out that during these desorption bursts between 70 and 100% of all the gas brought in during the OH-phase prior to the NBI pulse is present as particles in the divertor and the plasma. The same behaviour was found with NBI powers as low as 300 KW. Another hint, that nearly all the gas is desorbed in such a burst, is the fact, that the neutral density reaches a new equilibrium on a higher level very soon after the start of the NBI.
This is in contradiction to the behaviour in the old divertor, where the pressure decreases during NBI up to the highest power and independent of H- or L-mode, showing, that the walls were by far not saturated with hydrogen and could absorb the additional flux of energetic hydrogen atoms. The only exception were discharges with carbonized wall. There the pressure shows a very slow increase, which continues during the whole NBI pulse.

H-mode and IOC-regime

It appears that the new divertor has a detrimental effect on achieving the H-mode. The parameter range, in which it can be obtained, is strongly restricted and the achievable confinement is poor compared to the former condition. Whether this is due to the larger bypasses will be tested by reducing these for the next experimental phase.

The loss of a good H-mode is at least partly set off by discovering a new regime for OH-discharges in ASDEX, which does not show the usual saturation of energy confinement at higher densities. This regime called IOC (Improved Ohmic Confinement) appears to be connected with the reduced fuelling rate of the present ASDEX. It shows significant effects also on divertor pressure and recycling fluxes. Fig.6 depicts typical IOC discharge conditions. The electron density was programed with three plateaus and controlled by feedback. During the first density plateau we see also in the divertor pressure (p_D) a plateau, however , the ramp up to the second density plateau is marked by an overshoot and a relaxation to a lower pressure value. The effect is still stronger at the third plateau. This reduction in pressure which marks the transition to the IOC regime is connected with a decrease in plasma density in the scrape off layer/2/. This effect is also seen in the fluxes still closer to the wall, as measured by the sniffer probe. The electron current (Γ_e) at a bias of +10 V onto the collector of the sniffer as well as the ion fluxes (Γ_I) measured by the mass spectrometer on the sniffer probe (scanning H_2, HD, D_2) are decreasing during the subsequent plateaus in spite of increasing plasma density. It is also interesting to note that the external gas puff (dQ_g/dt) is practically zero over a large fraction of the last plateau, indicating together with the reduced recycling flux in the divertor a high particle confinement, too. If IOC shots are plotted in a divertor pressure to $\bar{n}_e$ graph (Fig.7), we see that in this regime, which seems to set in only above $\bar{n}_e > 2.5 * 10^{13} cm^{-3}$, the divertor pressure tends to saturate. With well carbonized walls and also with H_2 and uncarbonized walls, this regime was not yet found. In this case we obtain a more quadratic relationship similar to what we have always found with the former divertor. Until now it is not clear if and how far the IOC regime can be identified with regimes in OH discharges found on other experiments which show also an improved confinement. /4 /However, it is obviously different from an H-mode, since the shape of the density profile is triangular rather than rectangular.

Conclusion

Comparing the results obtained with the old and new divertor, it is certainly surprising that the occurrence of improved confinement regimes like the H-mode or the IOC-regime depends on what, at first glance, seems to be a minor modification of the machine. Since the magnetic configuration is essentially the same as before, the

change in the plasma behaviour appears to be a consequence of the different recycling. The latter is characterized by a substantially reduced divertor wall pumping and hence gas consumption, and also by increased neutral gas leakage (bypass) from the divertor dome into the main chamber.
There are also typical features which are qualitatively unchanged, like the asymmetry in the fluxes entering the divertor. Still, higher energy and particle fluxes are going to the lower divertor for the standard polarity of plasma current and toroidal field./3/

References:

/1/ Poschenrieder, W. et al., J. of Nucl. Mat., 111&112 (1982), 29
/2/ McCormick, K. et al., this conference
/3/ Fussmann, G. et al., J. of Nucl. Mat., 121(1984), 164
/4/ Alikaev, V. et al., Plasma Phys. and Contr.Fusion, 29 (1987),1295

Figure captions

Fig. 1 New divertor geometry

Fig.2 Gas consumption (integrated gas puff) and particle balance during plasma build up phase for two discharges in the old and the new divertor design, resp.

Fig.3 Divertor pressure (measured in a pumping port with a mass spectrometer) as a function of plasma density $\bar{n}_e$ for the various divertor modifications used on ASDEX.(narrow slits: 3.7 cm, wide slits: 6 cm, new design: 3.6cm)

Fig.4 Divertor pressure as a function of the ratio divertor coil current to plasma current I_{MP}/I_P (I_p=320 KA, B_t=2.17 Tesla, $\bar{n}_e=3*10^{13}cm^{-3}$, double null)

Fig.5 Neutral density in the divertor volumes Ia and II during a discharge with NBI. The maximum NBI power is 1.35 MW.

Fig.6 Signals relevant for recycling under IOC conditions.
$\bar{n}_e$: plasma density;
p_D: divertor pressure;
Q_g: quantity of fuelling gas admitted;
Γ_e: electron current collected by a sniffer probe near the wall at +10 V bias;
Γ_I: ion flux collected by same probe (RGA-scan over H_2, HD, D_2).

Fig.7 D_2-divertor pressure in dependence on $\bar{n}_e$ for a carbonized wall (normal OH confinement) and for the IOC-mode (plateau values)

Old design

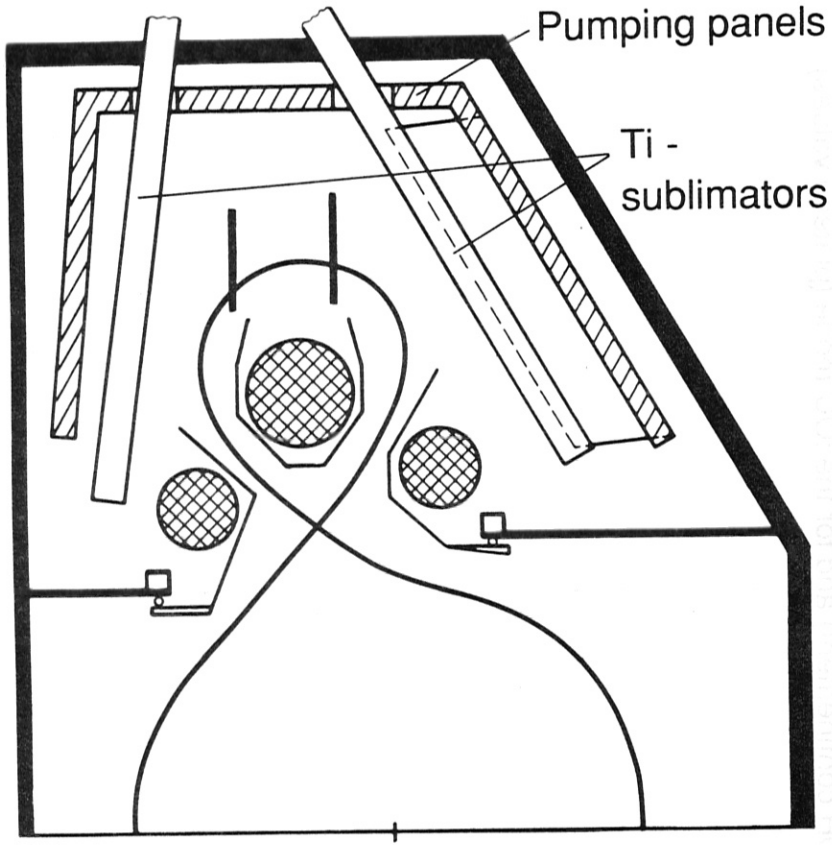

New design

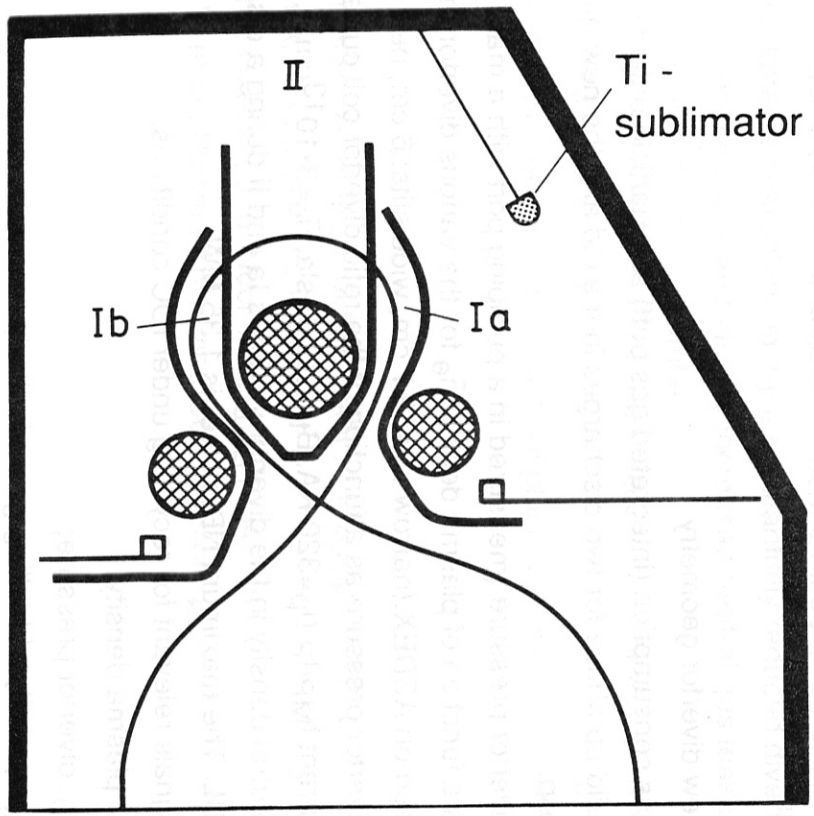

Fig.1

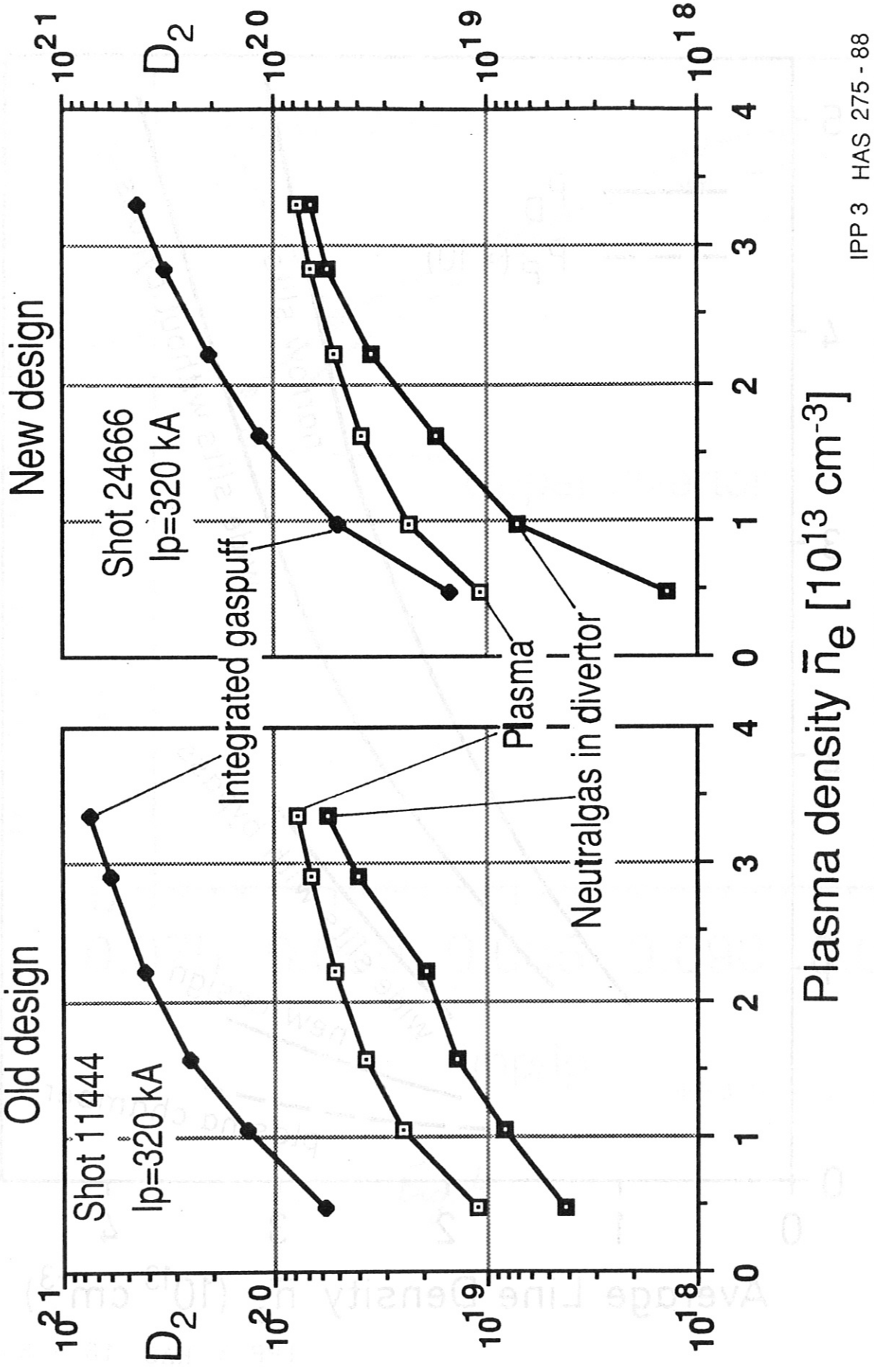

IPP 3 HAS 275 - 88

Fig. 2

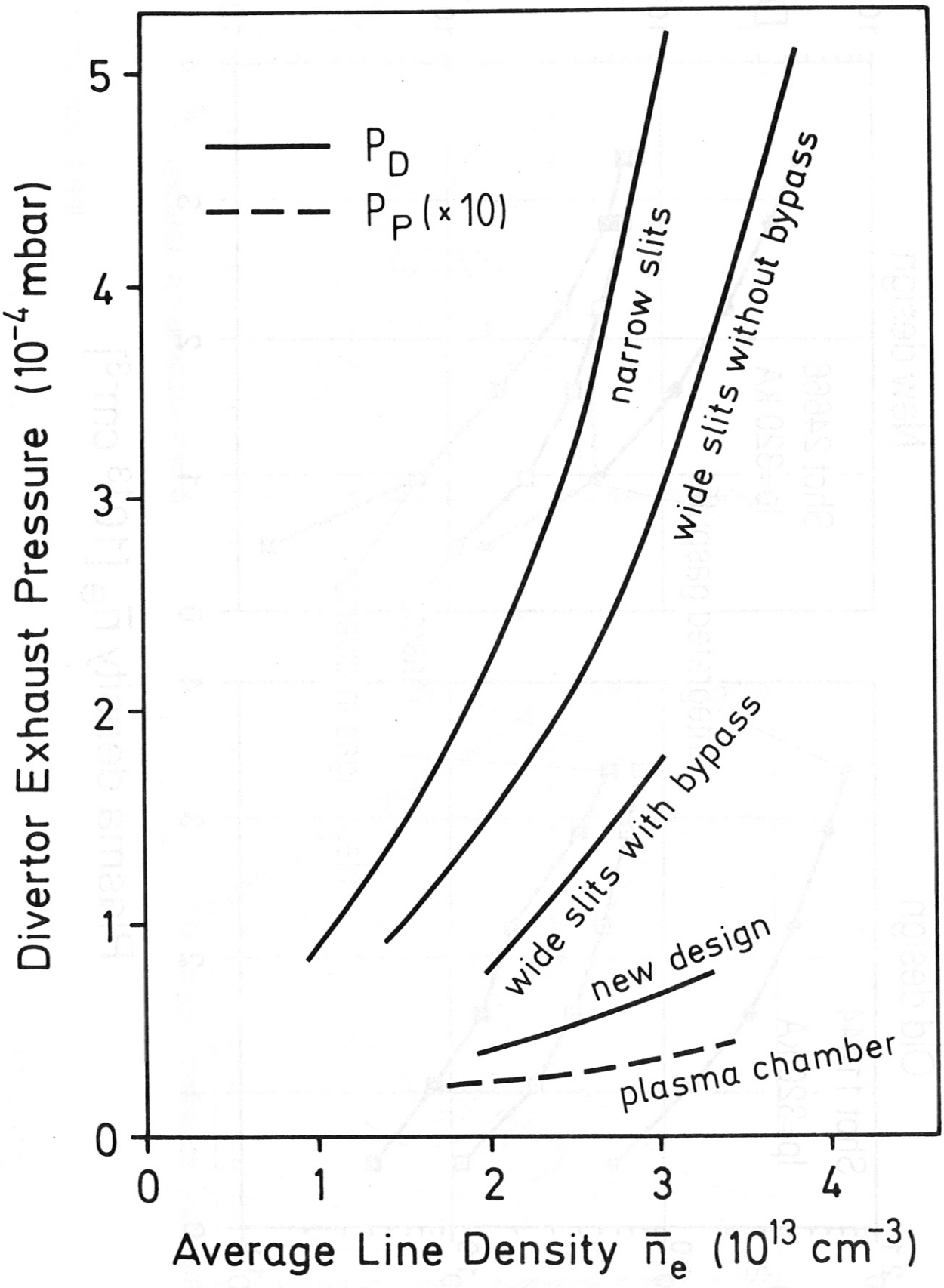

IPP 3 HAS 13 - 88

Fig. 3

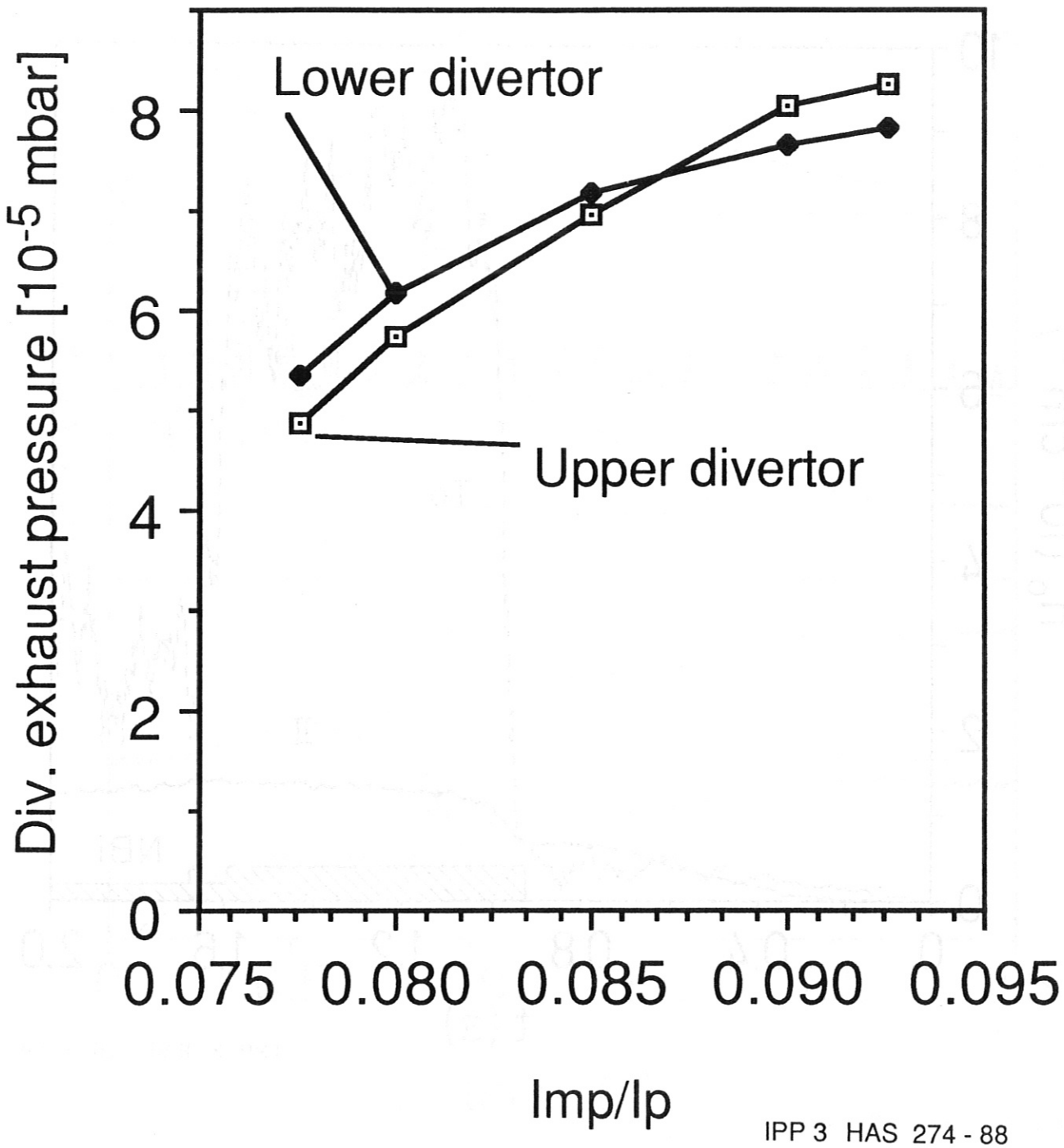
Lower divertor
Upper divertor
Div. exhaust pressure [10-5 mbar]
0
2
4
6
8
0.075
0.080
0.085
0.090
0.095
Imp/Ip
IPP 3 HAS 274 - 88

Fig. 4

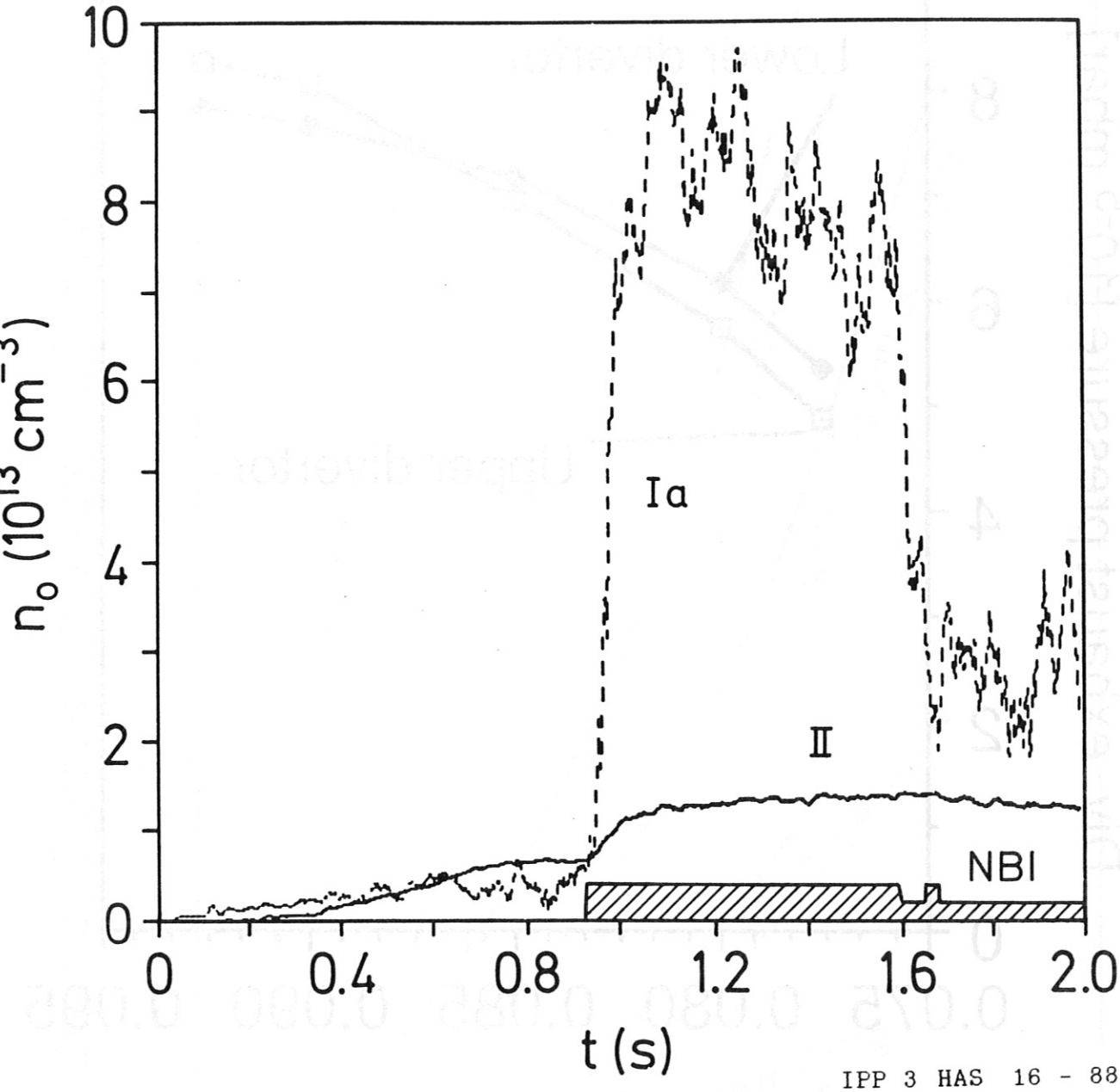

Fig 5

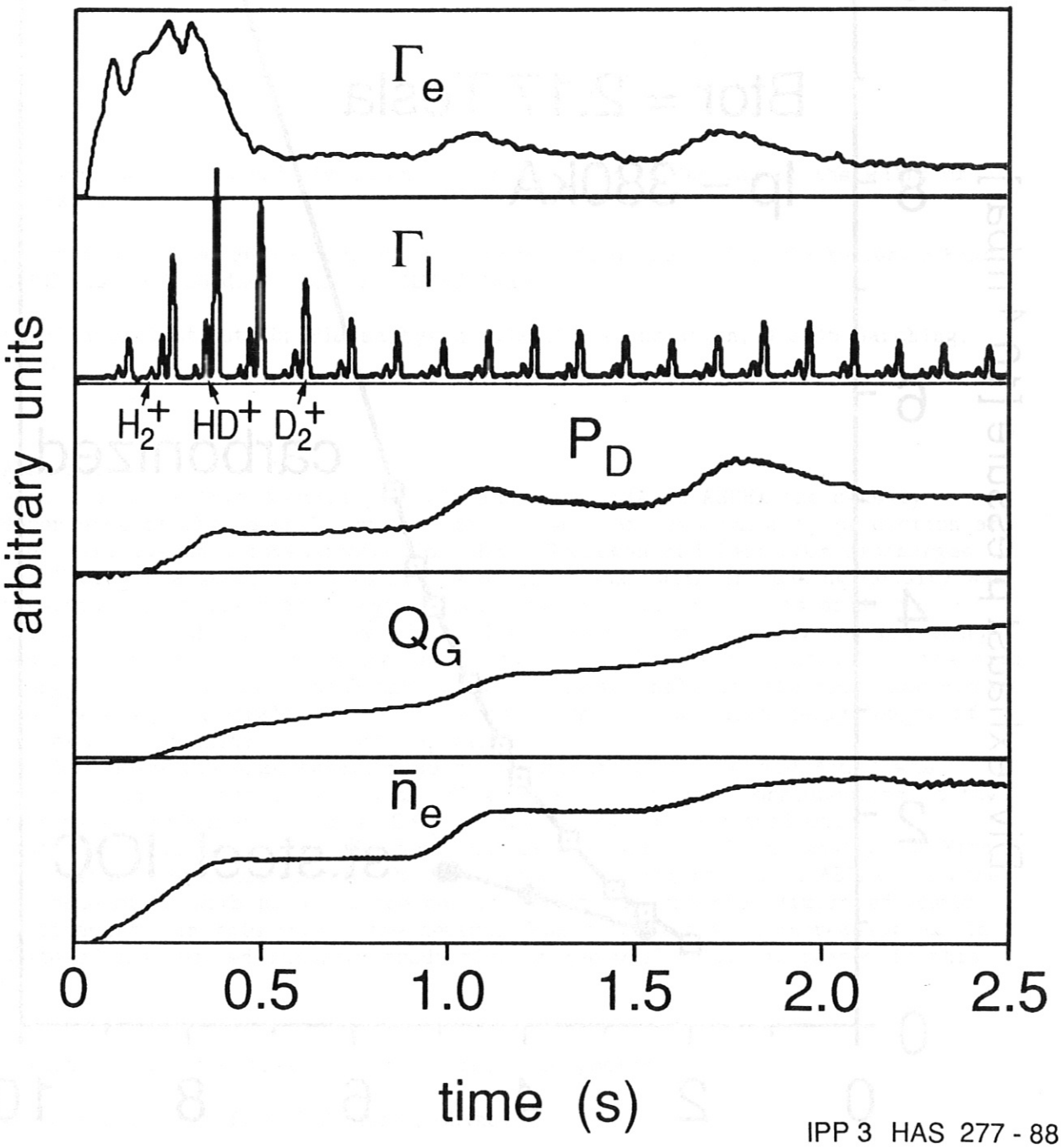

IPP 3 HAS 277 - 88

Fig. 6

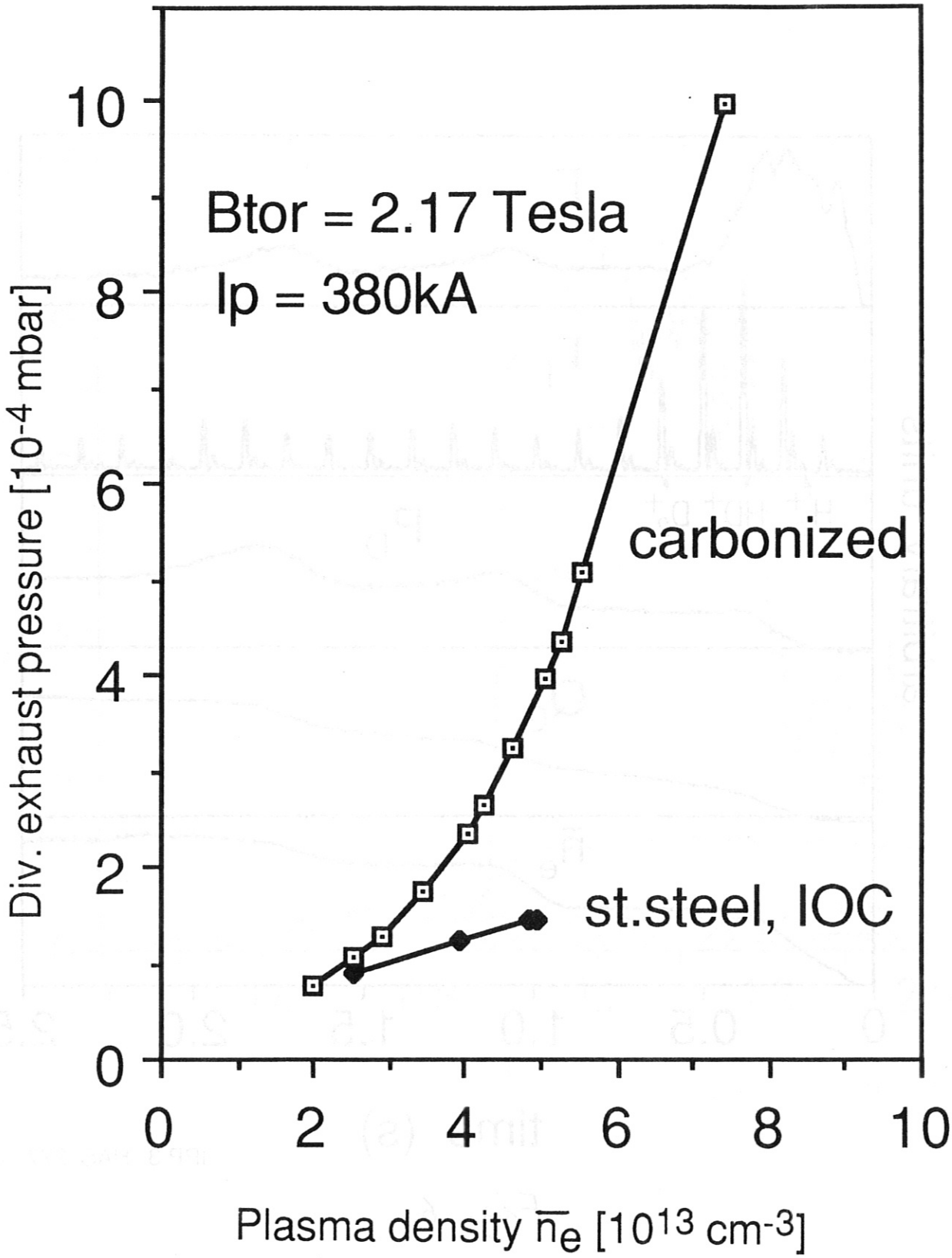

IPP 3 HAS 273 - 88

Fig. 7

The low energy neutral fluxes and their impurity production at the walls of ASDEX +.

H.Verbeek, V.Dose, Fu J.K.*, O.Gehre, J.Gernhardt, G.Janeschitz, E.R.Müller, H.Röhr, K.H.Steuer, F.X.Söldner, and the ASDEX-team.

Max-Planck-Institut für Plasmaphysik, EURATOM-Association, D-8046 Garching, F.R.G.

Abstract
With the Low Energy Neutral particle Analyser LENA at ASDEX the density dependence of the neutral flux, its mean energy and its impurity production at the walls has been investigated for Ohmic Hydrogen and Deuterium discharges. For Hydrogen a large increase of the neutral flux with increasing density was observed, while the mean energy of the neutrals decreases. This holds for Hydrogen over the whole range of densities. At constant density the low energy neutral flux increases with the safety factor q. This is in contrast to the high energy flux as measured with the charge exchange analyser. The flux increase of the low energy neutrals can be correlated with the increased decay length of the electron density for higher q-values.
For Deuterium the same behavior up to densities of $n_e \simeq 3.5 \times 10^{13} cm^{-3}$ was observed. For higher densities the flux behaves different corresponding to the different confinement regimes. Only in the regime of saturated Ohmic confinement, known so far, the flux increases further with increasing n_e. With the operational conditions of the new divertor configuration in ASDEX a further increase of τ_E with n_e up to the density limit was observed (improved Ohmic confinement). In this regime the neutral flux saturates with increasing n_e. In spite of the reduced impurity production at the walls, Z_{eff} increases in this case.

+ This version includes all figures from the poster.

* Guest scientist from IPP, Hefei, China.

Introduction

At the Garching divertor Tokamak ASDEX a low energy neutral particle analyzer based on time-of-flight techniques (LENA) is installed [1]. This is capable of measuring energy distributions of charge exchange (CX)-neutrals in the range of 10 to 1400 eV/amu. This energy range is most important for the plasma wall interaction i.e. impurity production and recycling [2,3].

For the measurement of an energy distribution with statistical relevance an integration time of ≃ 100 ms is required. In many cases, however, it is sufficient to know integrated quantities as the total particle flux, its mean energy , and the impurity influx caused by sputtering due to these neutrals. An effcient procedure for the computation of such integrals has recently be devised [4]. Its application allows for time resolutions of 1 ms during a shot and provides these data shortly after each shot.

In the past experimental period of ASDEX with the modified divertor configuration DV-2 the dependence of the neutral flux ,ϕ, its mean energy, $\langle E \rangle$,and the corresponding impurity influx, ϕ_{Fe}, on the main plasma parameters $\bar{n}_e$, (line integrated electron density) and q (safety factor) have been investigated for Ohmic discharges in a non-carbonized machine.

Results

In Fig.1 the neutral hydrogen flux and its mean energy are shown as function of n_e for different values of q.The data were taken from a series of hydrogen discharges when both $\bar{n}_e$ and J_{Plasma} (Plasma current) had reached plateau values. ϕ is increasing more than linearly with increasing $\bar{n}_e$ and the increase is larger the larger q is. At the same time $\langle E \rangle$ is decreasing.The higher the flux the lower is $\langle E \rangle$.

-=====-

Also ϕ_{Fe} is increasing with $\bar{n}_e$ but not as strongly as ϕ. No significant dependence of ϕ_{Fe} on q was observed.
Deuterium discharges show a behavior, which is different in some cases. (Fig. 1a) The $\bar{n}_e$-dependence of the neutral flux together with <E> for deuterium shots with q=2.75 are shown in Fig.2. Here two cases can be distinguished: If $\bar{n}_e$ is ramped up by the controlled gas valve the neutral flux increases almost linearly with $\bar{n}_e$ and <E> decreases simultaneously (dashed curves). If, however, the density is controlled such that a flat top is reached, the flux decreases and reaches a much lower level. These plateau values are indicated by filled dots connected by the solid lines in Fig.2. This occurs at densities $\bar{n}_e$ >3.5 10^{13} cm^{-3}. It corresponds to the recently discovered regime of Improved Ohmic Confinement (IOC) [5,6] . In this regime the particle confinement time τ_E increases further with increasing n_e while it levels off in the Saturated Ohmic Confinement regime (SOC), known so far. Whether the IOC regime is reached depends on the combined effects of gas puffing, recycling from the walls, and backstreaming from the divertor [6].
In some cases ϕ decreases further during the $\bar{n}_e$-flat-top. This is indicated in Fig.2 by dots connected by arrows at constant $\bar{n}_e$. If, after the plateau n_e is further increased by puffing more gas, ϕ increases rapidly and <E> falls. i.e. the discharge returns to SOC..
In Fig.2a the corresponding sputtered Fe-Flux from the walls is shown as a function of $\bar{n}_e$ for the 2 cases of SOC and IOC.
For two discharges the time development of ϕ, <E>, and ϕ_{Fe} together with a number of relevant signals is shown in Fig.3.
For #22985 (left in Fig.3) the density was controlled to a plateau of $\bar{n}_e$ = 1.44 $10^{13}cm^{-3}$ until 1.14 s and then ramped up to the density limit of $\bar{n}_e$ = 4.1 $10^{13}cm^{-3}$ at 2.3 s. The flux increases almost linearly as $\bar{n}_e$ is ramped up linearly.

-=====-

At the same time <E> decreases linearly. The sputtered Fe-atom flux, ϕ_{Fe}, increases less than linearly with $\overline{n}_e$. The intensity of a characteristic O^{VI} line measured spectroscopically increases , Z_{eff} calculated from the Bremsstrahlung in the IR region is decreasing, and β_p (derived from the Shavranov shift) is increasing with decreasing slope.
For #22987 (right in Fig.3) the density reached a plateau of 4.39 $10^{13}cm^{-3}$ from 1 to 1.7 s followed by a second plateau at $\overline{n}_e$=5.15 $10^{13}cm^{-3}$ from 2 s on. (However, after 2.2s J_{plasma} was already decreasing and the data are no longer interpretable.)
In #22897 ϕ is rising as n_e is ramped up. After reaching the flat top of $\overline{n}_e$, ϕ is decreasing to a much smaller value from where it continues decreasing slightly until $\overline{n}_e$ is increasing again. <E> shows the opposite behavior: it is minimal where ϕ has maxima and vice versa. ϕ_{Fe} still shows the maxima of ϕ, whereas less pronounced. Almost the same trace as ϕ shows the O^{VI}-signal. Z_{eff} and β_p show minima where ϕ and ϕ_{Fe} have maxima.

Discussion

In this paper the dependence of ϕ and <E> on $\overline{n}_e$ is discussed for Ohmic discharges. ϕ and <E> depend also strongly on the position of the plasma as a whole and of the separatrix and also on the mode of gas puffing and pellet injection.
The lower the energy of the detected CX-neutrals is, the more they originate from edge regions. As the total neutral flux ~~neutral flux~~, ϕ, is dominated by the neutrals with the lowest energies measured [4] it depends strongly on edge parameters.
The strong increase with q (Fig.1) is due to the increase of the decay length of n_e beyond the separatrix, while the density at the separatrix $n_e(s)$ stays roughly constant when q is increased [7]. The CX-flux measured with the carbon resistance probe also increases with q [8]. However, the

-=====-

high energy CX-flux as measured with stripping analyzers decreases with increasing q. This effect is also visible in the decrease of <E>, since <E> is dominated by the neutrals with the highest energies detected by LENA [4]. The sputtered Fe-flux, ϕ_{Fe} does'nt show any significant dependence on q.

This behavior is in contrast to that observed at PLT [9]. In the range of densities discussed here, ϕ at PLT is almost constant, while <E> decreases strongly. There is also a slight decrease of ϕ when q is increased. Apparently limiter (PLT) and divertor (ASDEX) tokamaks behave different in the neutral emission.

Deuterium discharges show generally a similar dependence on q as shown for Hydrogen in Fig.1. However, when the IOC regime, so far discovered for deuterium only, is reached, ϕ as a function of $\overline{n}_e$ levels off as shown in Fig.2 . Also <E> saturates.

This is more clearly seen in Fig.3: With #22985 (left half of Fig.3) a typical SOC-shot is shown. ϕ increases with $\overline{n}_e$ up to the density limit, while <E> decreases simultaneously. . β_p i.e. the energy content of the plasma is rising with decreasing slope, the latter being due to the saturation of τ_E. It is interesting that the sputtered Fe-flux from the walls, ϕ_{Fe}, increases less than linearly with n_e. This is due to the decrease of <E> and therefore also of the sputtering yield.

It is seen from Fig.3 that the O^{VI}-signal is increasing stronger than linear with $\overline{n}_e$. The O^{VI}-radiation originates from a plasma shell close to the edge. Its intensity is proportional to the O-density and the excitation in this shell. The O-density is due to desorption from the walls by the neutral flux. As it can be assumed that the desorption yield is independant of the energy in this range, the O-influx should be proportional to ϕ and therefore also to $\overline{n}_e$. In this case also the excitation is roughly proportional to

-=====-

$\bar{n}_e$. This explains the strong rise of the O^{VI}-signal with increasing $\bar{n}_e$.
In these Ohmic shots with rather high density Z_{eff} is dominated by light impurities namely O and C [10]. In #22985 Z_{eff} decreases with increasing $\bar{n}_e$ in spite of the fact that the O-influx increases. This reflects the deterioration of the confinement. For an explanation, however, the discussion of a detailed impurity transport model is necessary.
In shot #22987 (right half of Fig.3) the IOC regime is reached at≃ 1s. When the density is slightly increased by further gas puffing at ≃ 1.7s the discharge returns to SOC. After turning into the IOC regime the flux decreases to a much lower level while <E> becomes larger than before. Because of the paticular control of $\bar{n}_e$ in this shot the gas valve opens again at ≃ 1.7s and a second maximum in ϕ occurs. Also ϕ_{Fe} has two maxima, whereas <E> has minima at the same times. It is remarkable that the O^{VI}-signal closely follows ϕ. Though both ϕ_{Fe} and the O^{VI}-signalshow maxima at about 1.0 and 2.0 s, Z_{eff} shows minima at these times. Apparently there is an accumulation of impurities in the plasma during the IOC regime. The improved energy confinement is accompanied by improved particle confinement [5,6]. Equilibrium is reached at ≃ 1.2 s. This shows up in the enhanced energy content (β_p) between 1.2 and 1.7 s. This effect is stronger than the reduced influx of impurities.

Finally it should be mentioned that in this operational period of ASDEX the LENA was mounted in close proximity to a large protection limiter, which was positioned 4cm from the separatrix. After installation of this limiter the neutral flux increased by a factor of ≃ 50. Thus ϕ, as measured at the present location, is dominated by the neutral atom density due to the recycling at the limiter. Therefore, the absolute values of ϕ are not representative for the whole Tokamak.

-=====-

Conclusions

The low energy neutral flux increases strongly with increasing $\bar{n}_e$ and, at constant $\bar{n}_e$, with increasing q. However, for Deuterium discharges the neutral flux depends on the particular confinement regime of the plasma. As observed in the IOC regime the flux is reduced when the energy confinement increases (Fig. 4). This reflects the dominant role of the recycling (mainly on the protection limiter) on the neutral flux. Recycling is the main source of the neutral atom density responsible for the production of CX-neutrals.

With the decrease of the neutral flux to the walls the impurity production there by sputtering and desorption decreases. Though the impurity influx during the IOC regime is reduced, Z_{eff} increases. Because of the increased particle confinement time the impurity concentration in the plasma increases.

-=====-

References

[1] H.Verbeek, J.Phys.E:Sci.Instrum. 19(1986),964

[2] H.Verbeek et al. J.Nucl.Mat.145-147(1987),523

[3] R.Behrisch,J.Roth,G.Staudenmaier,H.Verbeek
Nucl.Instr.Meth.Phys.Res.B18(1987),629

[4] V.Dose, H.Verbeek, App.Phys.Lett. 51(1987),229

[5] E.R.Müller et al. 15th EPS-Conf.on Controlled Fusion and Plasma Heating Dubrovnik (1988) Europhysics Conf.Abstr.12B (1988) 19

[6] F.X.Söldner et al. submitted to Phys.Rev.Lett.

[7] K.McCormick et al. J.Nucl.Mat.145-147(1987),2154)

[8] G.Staudenmaier and W.R.Wampler this Conf.

[9] D.N.Ruzic, D.B.Heifetz, S.A.Cohen, J.Nucl.Mat.145-147(1987),527

[10] K.H.Steuer et al. 15th EPS-Conf.on Controlled Fusion and Plasma Heating Dubrovnik (1988)Europhys.Conf.Abstr.12B (1988) 31

Figure captions

Fig. 1 Neutral particle flux (open symbols) and its mean energy (filled symbols) as function of the line integrated density $n_{\bar{e}}$
for different q values of Ohmic Hydrogen discharges.

Fig. 1a Same as Fig. 1 for Deuterium. (No IOC-shots are included in this figure.)

Fig. 2 Neutral particle flux (dots, left scale) and its mean energy (circles, right scale) as a function of $n_{\bar{e}}$ for deuterium discharges. Broken curves: density ramp up, solid curves: density flat top.

Fig. 2a Sputered Fe-flux from the walls as a function of $n_{\bar{e}}$

Fig. 3 Time dependence of the neutral flux, the line averaged density, the mean energy, sputtered Fe-flux, intensity of a characteristic O^{VI}-line, Z_{eff}, and β_p
during ASDEX shots #22985 (left) and #22987 (right).

Fig. 4 τ_E as a function of the D^0-flux to the walls.

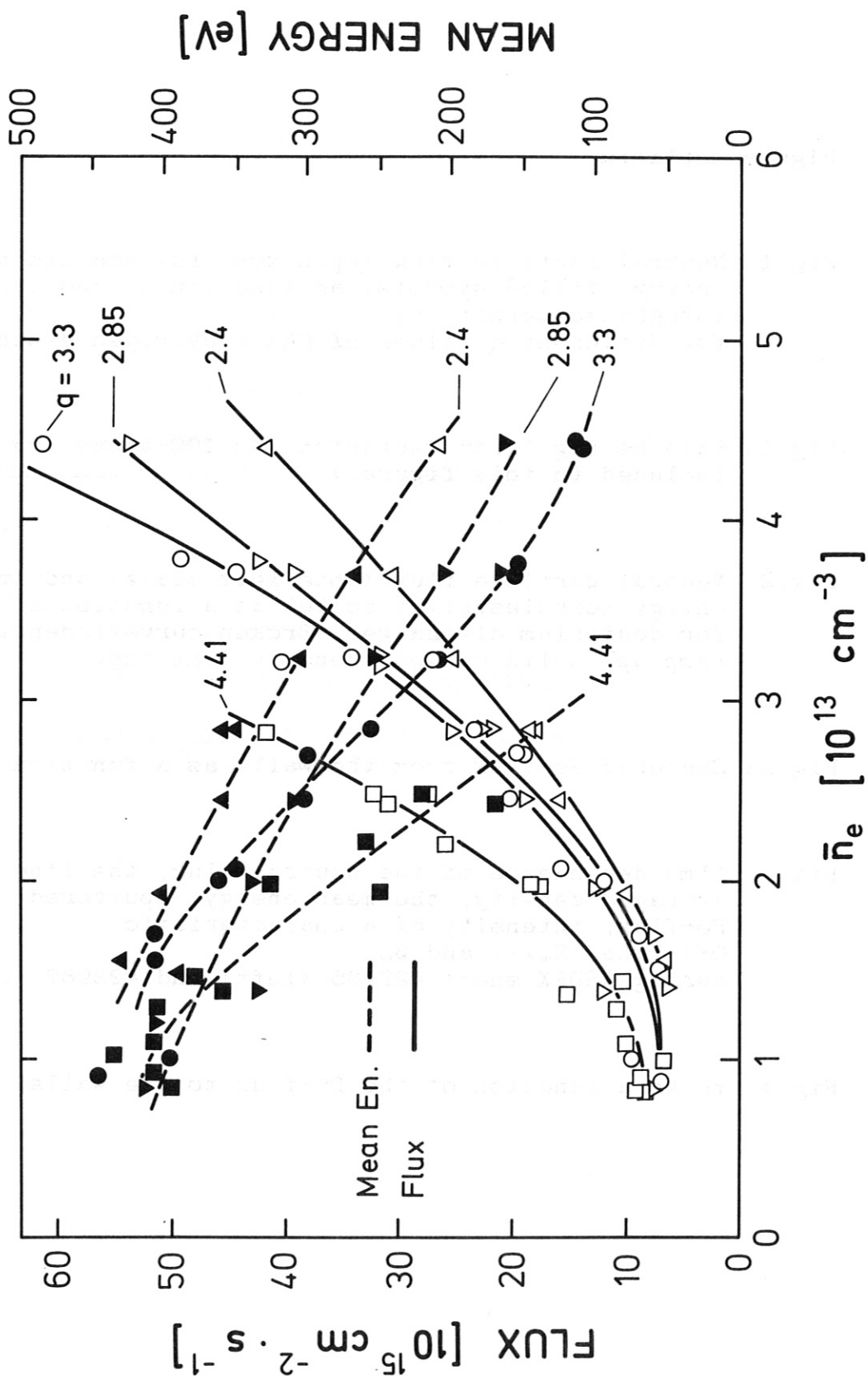

Fig. 1 Neutral particle flux (open symbols) and its mean energy (filled symbols) as function of the line integrated density $\bar{n}_e$ for different q values of Ohmic Hydrogen discharges.

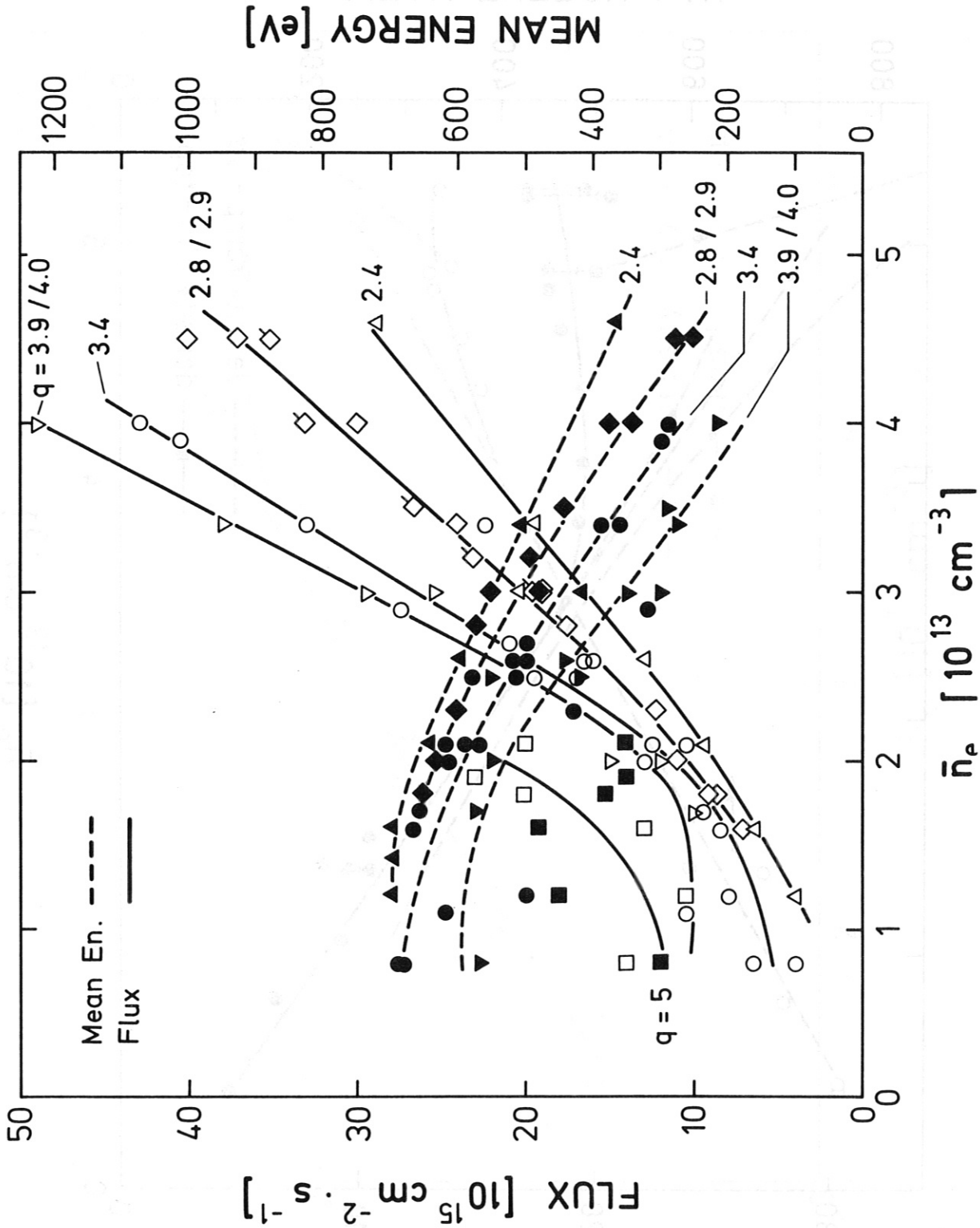

Fig. 1a Same as Fig. 1 for Deuterium. (No IOC-shots are included in this figure.)

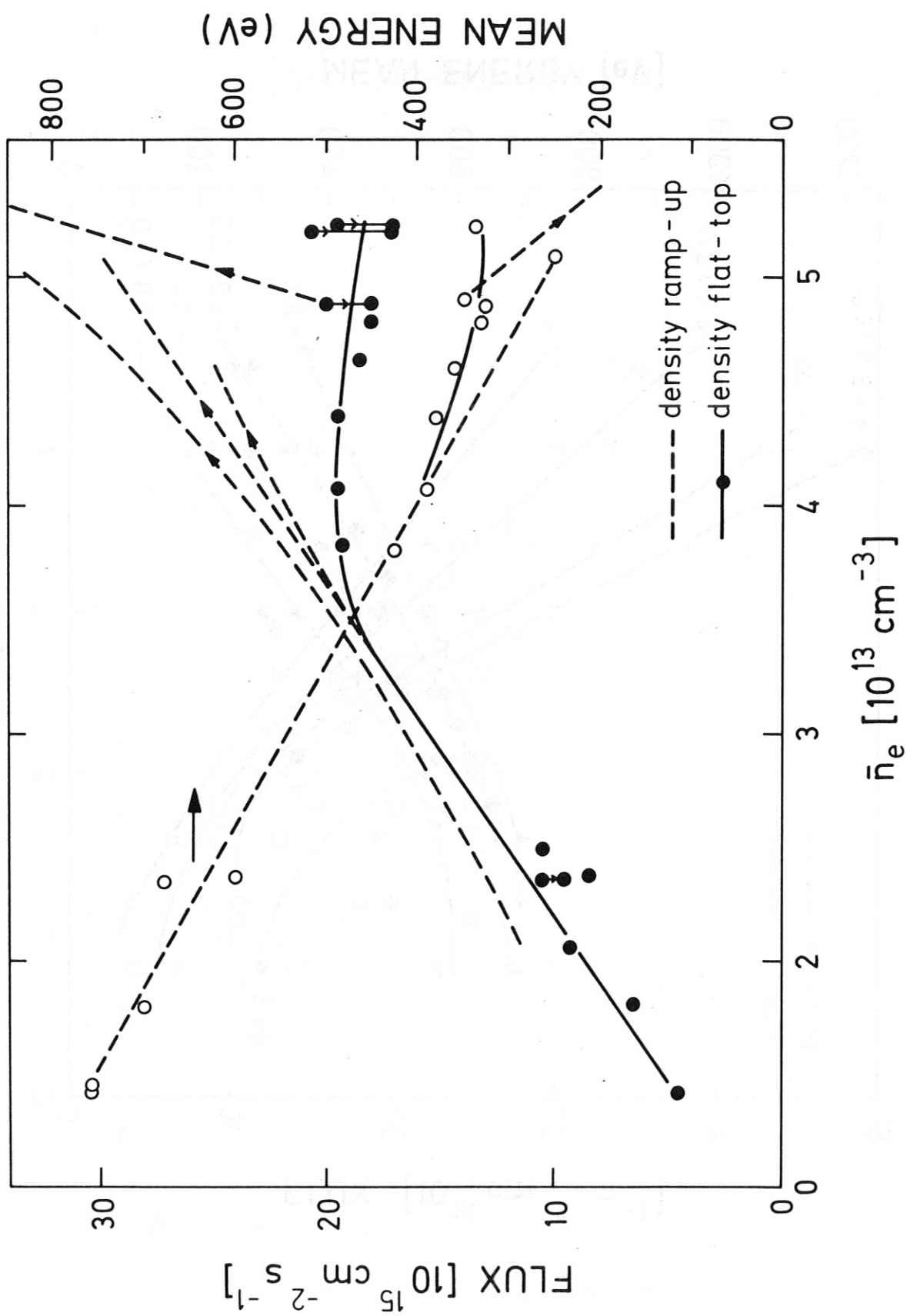

Fig.2 Neutral particle flux (dots, left scale) and its mean energy (circles, right scale) as a function of n_e for deuterium discharges. Broken curves: density ramp up, solid curves: density flat top.

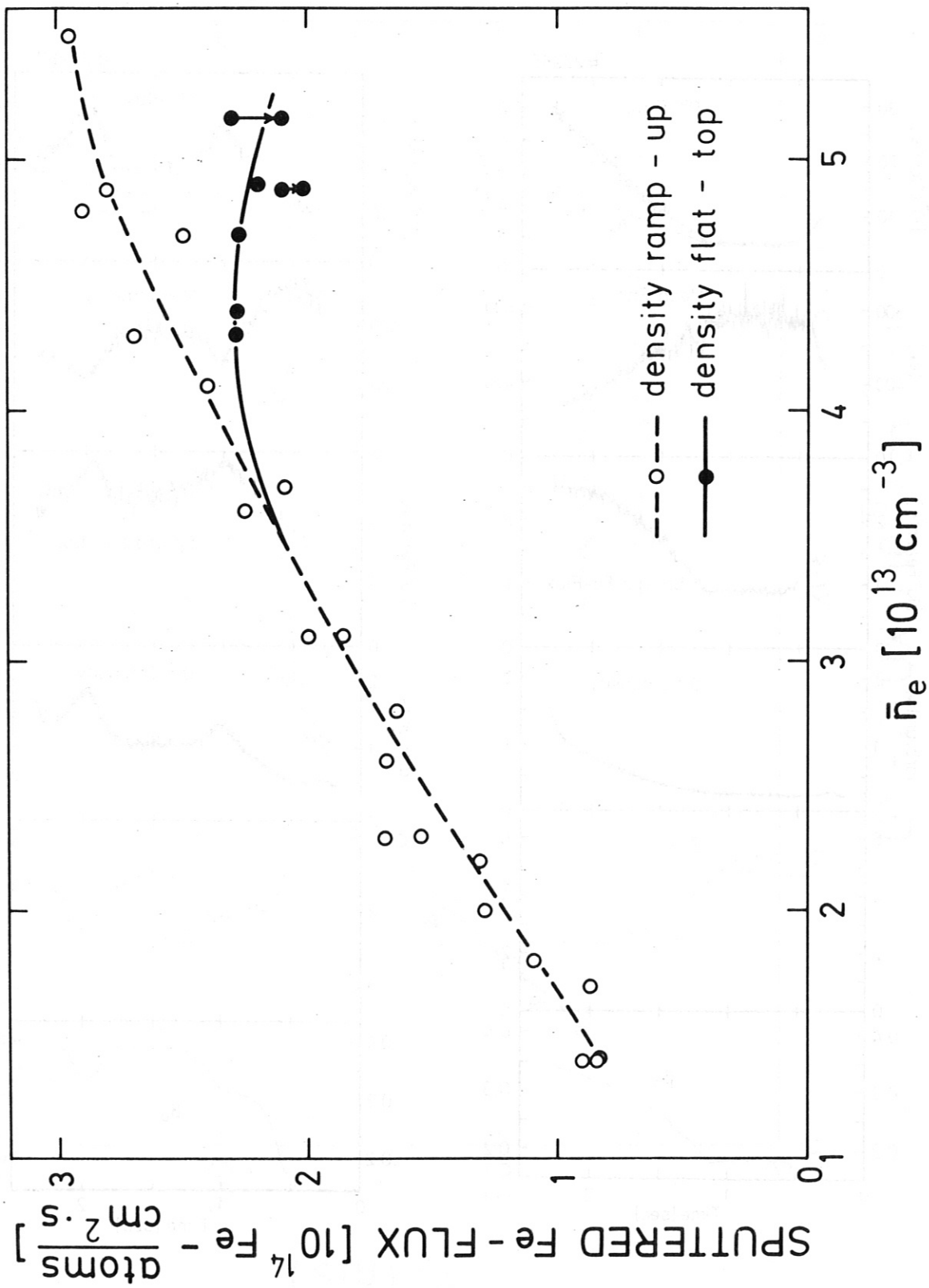

Fig. 2a Sputered Fe-flux from the walls as a function of n_{vw}

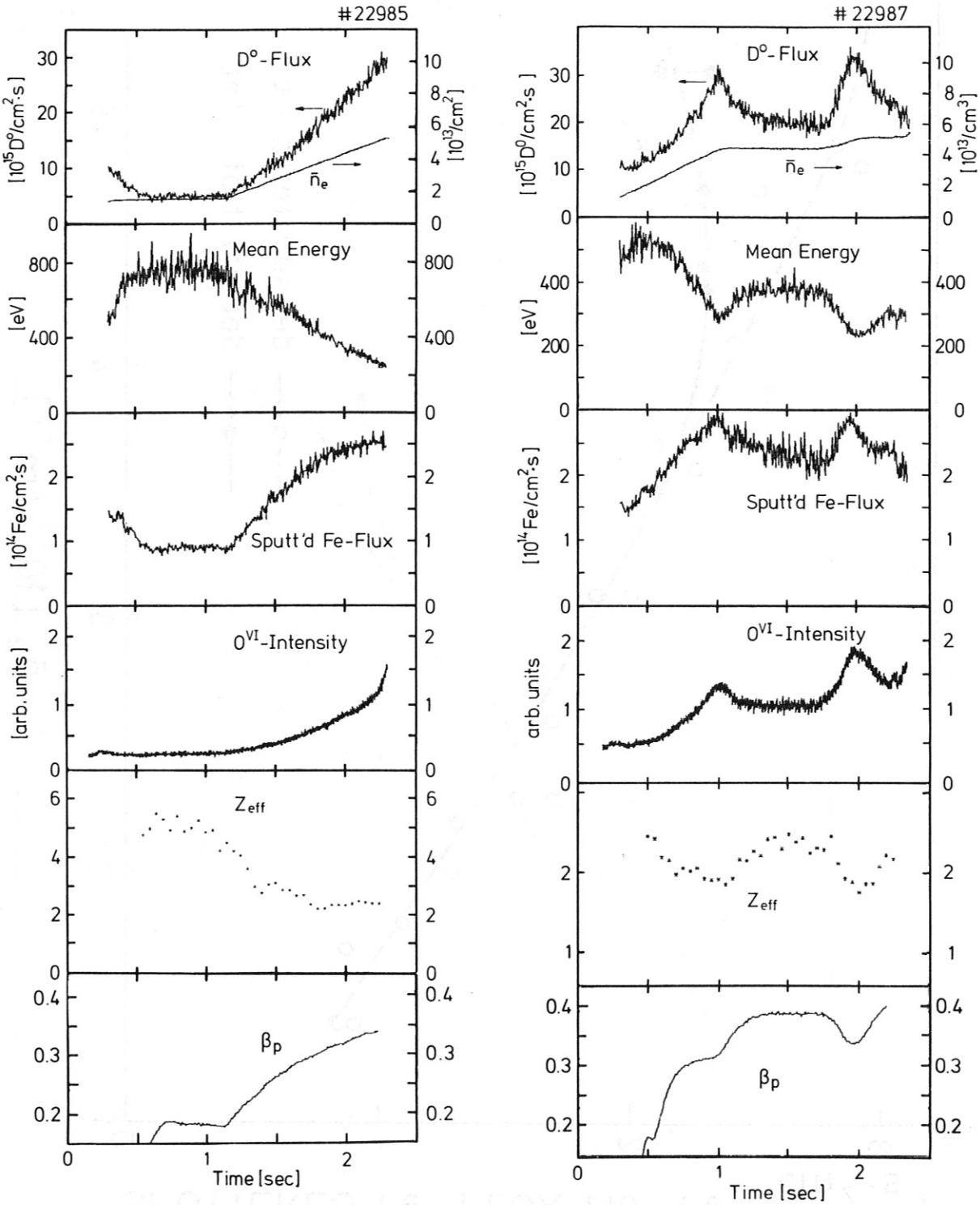

Fig.3 Time dependence of the neutral flux, the line averaged density, the mean energy, sputtered Fe-flux, intensity of a characteristic O^{VI}-line, Z_{eff}, and β_p during ASDEX shots #22985 (left) and #22987 (right).

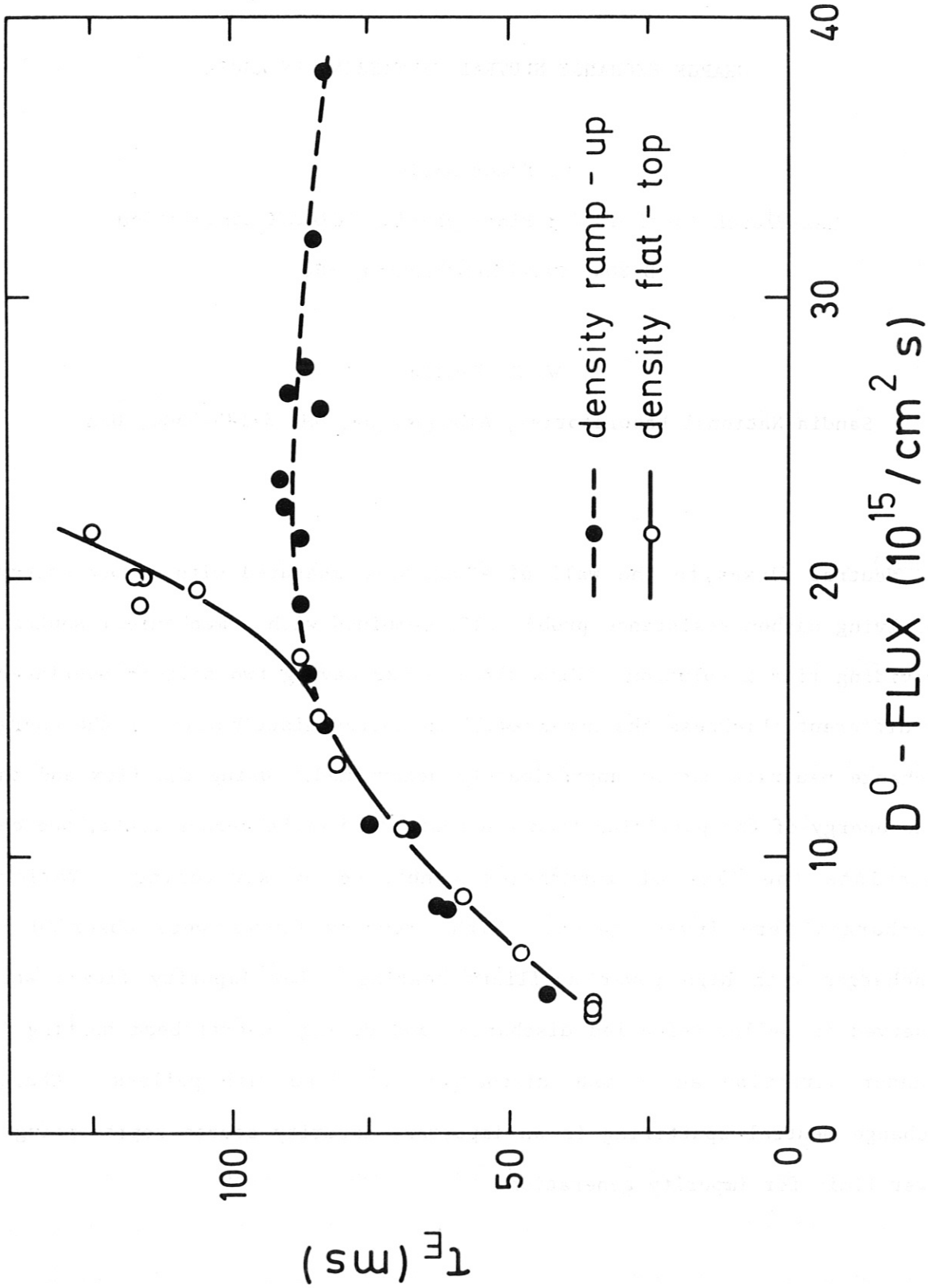

Fig. 4 τ_E as a function of the D^o-flux to the walls.

CHARGE EXCHANGE NEUTRAL SPUTTERING IN ASDEX

G. Staudenmaier

Max-Planck-Institut für Plasmaphysik, EURATOM Association

D-8046 Garching/München, FRG

W. R. Wampler

Sandia National Laboratories, Albuquerque, NM 87185-5800, USA

Neutral fluxes to the wall of ASDEX were measured with a new energy-resolving carbon resistance probe, CRP, combined with a mechanical shutter, providing time resolution. With the new CRP having two silicon overlayers of different thickness the non-Maxwellian energy distribution of the charge exchange neutrals can be approximately determined. Using the flux and the mean energy of the particles from the resistance probe measurements, one can calculate the flux of impurities generated by sputtering. Various discharges were investigated. High impurity fluxes were observed in discharges with high power auxiliary heating. Low impurity fluxes were observed in pellet-refuelled discharges and during neutral beam heating in counter direction and H-mode discharges refuelled with pellets. Charge exchange neutral sputtering is an important impurity source representing a lower limit for impurity generation.

1. INTRODUCTION

Charge exchange neutrals generated in a magnetically confined plasma flow to the walls unaffected by the size and shape of the confining magnetic field. Impinging on the wall, they generate impurities by sputtering and desorption /1,2/. Although less than 1% of a monolayer per second is eroded, the total impurity flux obtained from the whole wall area is large enough to be the dominant source of metal impurities in ohmically heated deuterium discharges in ASDEX /2/ and a dominant source in almost all discharges.

Charge exchange fluxes are measured with an energy-resolving carbon resistance probe, CRP, /3-5/. The charge-exchange-sputtered impurity flux is calculated from the neutral flux and its mean energy using sputtering data /6/. In a previous study /2/ the mean energy and flux of charge exchange neutrals incident on the wall in ASDEX were measured using carbon resistance probes. In this paper the investigations on ASDEX are continued with an improved CRP which measures the flux and the mean energy in two energy intervals. Moreover, a mechanical shutter was used to select distinct phases of the discharge and to limit the total flux to the CRP. A variety of discharges with different plasma parameters, different refuelling and auxiliary heating are investigated.

2. EXPERIMENTAL

To measure the charge exchange neutral flux Γ and its mean energy $\bar{E}$, an energy-resolving carbon resistance probe is used /3-5/. The resistance change ΔR of a thin evaporated carbon film in the case of low bombardment fluences $\phi < 2 \times 10^{15}$ cm^{-2} is given by $\Delta R/R_o \simeq (\alpha/\rho_o \tau) \varepsilon \phi E$, where R_o is the non-bombarded resistance of the film with a thickness τ and a resistivity

ρ_o, E is the energy of the incident particle and ε is the fraction of this energy which produces damage in the carbon. ε depends on the particle species and is 0.3 for deuterium and 0.2 for hydrogen. For the probes used in this study τ ~ 150 nm and R_o ~ 130 Ω. Energy resolution is achieved using a thin insulating silicon overlayer over part of the carbon film. The particles lose some of their energy in passing through the overlayer and therefore cause a smaller resistance change in the carbon layer beneath. The mean particle energy is evaluated from the ratio of the resistance change with the overlayer ΔR(Si) to that with no overlayer ΔR as described in Refs. 3 and 4. Since the charge exchange neutrals are not monoenergetic, the calibration of resistance change versus particle energy was calculated for a Maxwellian energy distribution.

In previous experiments /2/ carbon resistance probes with a single overlayer thickness were used. In this study we used probes with two overlayer thicknesses, 4 and 20 nm. The region with the thicker overlayer is only sensitive to particles with energies above about 1 keV, while the region with the thinner overlayer responds to particles with energies down to about 100 eV. Thus the two regions of the probe provide a measurement of the flux and mean energy of particles in two energy intervals. The true particle energy distribution was approximated by two Maxwellian distributions, one for energies below 1 keV and one for energies above 1 keV, with characteristic energies chosen to reproduce the measured resistance changes. The minimum detectable change of resistance was about ΔR = 0.1 Ω corresponding to a particle fluence of about 2 x 10^{13} D/cm^2 in the present study. This is about 5 times less sensitive than the probes used in the previous study /4/. The different sensitivity is due to the different carbon thickness.

The CRP is positioned at the outside wall in the midplane of ASDEX. It views almost the whole plasma surface, having a direct line of sight to the probe. Roughly 90% of the neutral particles measured with the CRP originate from a plasma region of $r/a \geq 0.75$ where r is the radial position and a is the radius of the last closed flux surface or separatrix. In fact, the CRP measures exactly that neutral particle flux in the relevant energy range for sputtering (about 100 eV to about 1 keV) which erodes this particular wall area. To obtain this information from a conventional neutral particle analyzer requires a poloidal and toroidal scan. A scan in poloidal direction needs several identical discharges, and a toroidal scan is often not possible simply because of lack of free space. This advantage of the CRP is offset by several disadvantages, above all its lower sensitivity and the fact that the resistance change saturates already at a fluence of 2×10^{15} D/cm^2, corresponding to only about 10 ohmic discharges. Moreover, for Maxwellian distributions of low temperature the saturation fluence might be even smaller, while for higher temperatures ($kT \geq 800$ eV) the saturation fluence is higher. However, the charge exchange flux at these high energies contributes only little to the charge exchange sputtering.

Time-resolved flux measurements can be achieved by two methods: (i) The probe resistance is recorded periodically during the discharge. This method was applied at TFTR /7/. (ii) A mechanical shutter in front of the CRP allows the probe to be exposed during an interesting and well-defined phase of the plasma discharge. The exposure time should be long enough to obtain a measurable resistance change, but not too long to prevent rapid saturation. In this work a shutter was used with exposure times ranging from 0.25 to 1.5 s. The time needed to open or close the shutter completely is about 25 ms. Obviously, with a combination of the two methods good time resolution an optimum life time of the CRP can be achieved.

3. RESULTS AND DISCUSSION

Figure 1 shows particle energy distributions obtained from the new CRP for some typical discharges. In ohmic discharges the charge exchange neutral flux in the energy range from about 100 eV to about 1 keV is characterized fairly well by one low-temperature Maxwellian distribution. During 1.3 MW neutral beam heating a higher-energy tail above about 1 keV appears with a Maxwellian temperature of about 800 eV for co-injection (line-averaged density $\bar{n}_e = 2.8 \times 10^{13}$ cm^{-3}) and kT = 700 eV for counter-injection with a high density of $\bar{n}_e \simeq 8 \times 10^{13}$ cm^{-3}. Co-injection and counter-injection refer to the direction of the injected neutral beam particles with respect to the plasma current. For pellet-refuelled discharges with $\bar{n}_e \simeq 7 \times 10^{13}$ cm^{-3} the neutral fluxes are much lower. A combination of pellet refuelling with 2 MW neutral beam heating produces very high densities (density limit as high as 1.3×10^{14} cm^{-3}) and the high energy neutral flux is reduced. This is a consequence of the opacity of the plasma to neutrals. At high densities practically all neutrals generated near the core undergo further charge exchange interactions at larger radial positions where the plasma temperature is lower.

Impurity fluxes are estimated by multiplying the charge exchange fluxes from the CRP measurements with the sputtering yield for a Maxwellian energy distribution. Yields for iron (representative of a stainless steel wall) sputtered with deuterium range from $Y = 10^{-2}$ for kT = 100 eV to $Y = 3 \times 10^{-2}$ for kT = 500 eV /6/. If the wall is carbonized, the carbon flux sputtered by charge exchange neutrals has at least the same magnitude as the metal flux, since the sputtering yield including chemical effects is comparable in size, i.e., $Y = 2 \times 10^{-2}$ to 3×10^{-2} almost independent of energy in the energy range from 20 eV to about 1 keV /8/. Moreover, carbon and oxygen can

be released from metal walls and carbonized walls by charge-exchange-neutral-induced desorption. Desorption yields for a monolayer coverage of CO or oxygen can be as high as sputtering yields or higher /9/. However, exact data are still required for the surface conditions in tokamaks.

For constant plasma density it is observed that the charge exchange neutral flux and the resulting impurity flux both increase with increasing safety factor, $q(a) = (B_t/R)(B_p/a)$, as depicted in Fig. 2, while the mean energy evaluated from the CRP measurements remains nearly constant ($\bar{E} = 2$ kT $\simeq$ 400 to 500 eV for ohmic heating and about 800 eV for neutral beam heating). B_t and B_p are the toroidal and poloidal magnetic field strengths and R and a are the major and minor radii of the plasma. In ohmic discharges the q(a) variation was achieved by varying the toroidal field B_t, while the plasma current was kept constant. In the case of neutral beam heating both B_t and I_p were varied. For all three curves, two for ohmic discharges and one for neutral beam heating, the slope of the curves is the same. The difference in the absolute values for the two series of ohmic discharges is due to two different confinement regimes /10/. During neutral beam heating the impurity release is higher compared with ohmic heating alone.

The behavior of impurity release by charge exchange neutrals can be related to properties of the scrape-off layer density profile. The density profile can be described by the density at the separatrix $n(a) \simeq 0.29\ n_e$, where n_e is the line-average electron density of the plasma, and the exponential density decay length $\lambda_n = \text{const}\ q(a)^{\alpha}$, which depends on the safety factor /11/. For ohmic discharges $\alpha = 0.35$ gives the best fit. Note that $\alpha = 0.5$ corresponds to the change in λ_n as a consequence of the varying midplane-divertor plate distance L: $\lambda_n = (D_\perp L/v'')^{0.5}$, where $D_\perp$ is the

perpendicular diffusion coefficient and $v_{\parallel}$ the global streaming velocity along the field lines in the scrape-off layer. The density from the above model:

$$\frac{n(r)}{n(a)} = \exp\left[- \frac{(r - a)}{\lambda_n q} \right]$$

with $\lambda_n = 1.29\ q^{0.35}$ for ohmic discharges is plotted versus the safety factor q in Fig. 2 at the radius r of the protective limiter 5 cm outside the separatrix which is the most protruding part of the wall close to the CRP. Auxiliary heating increases λ_n but the dependence of λ_n on q remains unchanged /12/. Figure 2 shows that the impurity flux density due to sputtering by charge exchange neutrals at the wall has the same dependence on safety factor as the plasma density at the protective limiter which is likely to be the major source of neutrals to the plasma near the CRP. The idea here is that a smaller safety factor gives a steeper density gradient at the plasma edge and therefore less neutral recycling and less sputtering at the wall.

The most dramatic changes in impurity production were found during auxiliary heating. As previously reported /2/, charge exchange sputtering increases with the total power deposited in the plasma (ohmic power and absorbed neutral beam power and absorbed RF power) by more than one order of magnitude, as shown in Fig. 3 by full symbols. In the meantime, the divertor geometry has been modified and consequently the gas refuelling and recycling properties have also been changed. But sputtered impurity fluxes are not affected, as can be seen from Fig. 3. From spectroscopy we know that the increase of impurity concentration from ohmic heating to the L-phase of neutral beam heating is caused by enhanced impurity production, for example due to increased charged exchange sputtering /13/. Also during ICRH the charge exchange sputtering increases with heating power as observed

in other experiments /14/. If the RF power absorbed in the plasma is taken to compute the total power (instead of the power to the antennae used in /2/), the same dependency as for neutral beam heating is observed. However, during ICRH a much higher impurity content in the plasma compared to neutral beam heating at the same power level is inferred from spectroscopic data /13/. Increase of ion sputtering or changed transport could explain this discrepancy.

Discharges having reduced charge exchange sputtering were found: these are pellet refuelled ohmic and neutral beam heated discharges, H-mode (high confinement) discharges and discharges with neutral beam injection in the direction counter to the plasma current /15/. The lowest values of charge exchange sputtering were measured during pellet-refuelled H-mode discharges at high heating power and high density ($\bar{n}_e \simeq 8 \times 10^{13}$ cm^{-3}). This might be due to the reduced exponential density decay length ($\lambda_n \simeq 1$ cm) at the plasma boundary /16/.

The different values of impurity release for constant heating power (cf. Fig. 3) are partly due to the described q(a) variation and to the different line-averaged densities. Results obtained with the low energy neutral particle analyzer LENA show that the neutral fluxes increase with density while the mean energies decrease at the same time, so that the slope of charge exchange sputtering versus $\bar{n}_e$ decreases with increasing density /17/.

Recent analysis of deposited metal impurities on long term samples exposed to about 700 discharges indicated mean deposition rates of about 10^{13} Fe/cm^2 s /18/. This is in good agreement with the erosion rates by charge exchange neutral sputtering estimates from the CRP measurements (see Fig. 3). Both results indicate that in ASDEX a considerable amount of metal impurities are generated by charge exchange sputtering.

Finally, it should be pointed out that the power transported to the wall by charge exchange neutrals plotted versus the total heating power yield about the same pattern as shown in Fig. 3 for the charge exchange sputtering. The lowest power of 1 to 2 mW/cm^2 was observed for ohmic heating and pellet-refuelled H-mode, while for high power neutral beam heating the power rises up to about 100 mW/cm^2. However, the power lost via charge exchange neutrals in the main plasma chamber of ASDEX remains always below 1% of the total heating power, which is still small compared to the radiated power of 15% of the heating power measured by bolometry /19/.

Although charge exchange neutrals carry only a small fraction of the heating power these particles produce a significant source of metal impurities in the main plasma chamber of ASDEX. Discharges with good confinement properties have lower charge exchange sputtering at the wall, but the good confinement results in accumulation of impurities such that the impurity content of the plasma becomes too high despite the reduced influx of impurities to the plasma /20/.

ACKNOWLEDGEMENTS

The authors gratefully acknowledge the ASDEX team for providing data and for extensive discussions. In particular, we want to thank J. Neuhauser and H. Verbeek for clarifying discussions. This work was performed at Max-Planck-Institut für Plasmaphysik and at Sandia National Laboratories. The work at Sandia National Laboratories was supported by the U.S. Department of Energy under contract number DE-AC04-76DP00789.

REFERENCES

1. D. E. Voss and S. A. Cohen, J. Nucl. Mater. 93&94 (1980) 405.
2. G. Staudenmaier and W. R. Wampler, J. Nucl. Mater. 145-147 (1987) 569.
3. W. R. Wampler, J. Nucl. Mater. 128&129 (1984) 951.
4. W. R. Wampler, J. Vac. Sci. Technol. A3 (1985) 1067.
5. W. R. Wampler and S. A. Cohen, Nucl. Fusion 25 (1985) 771.
6. J. Bohdansky, Data Compendium for Plasma Wall Interactions, Nucl. Fusion, special Issue (1984) p. 61.
7. W. R. Wampler, to be published.
8. J. Roth, J. Nucl. Mater. 145-147 (1987) 87.
9. A. Koma, Ed., Inst. of Plasma Physics, Nagoya University, Nagoya Japan, Report IPPJ-AM-22 (1982).
10. E. R. Müller, F. X. Söldner, G. Janeschitz et al., 15th Europ. Conf. Contr. Fusion and Plasma Heating, Dubrovnik, 16-20 May 1988.
11. K. McCormick, Z. A. Pietrzyk, H. Murmann et al., J. Nucl. Mater. 145-147 (1987) 215.
12. K. McCormick, Z. A. Pietrzyk, H. Murmann et al., Europhys. Conf. Abstr. 11D, part II (1987) 666.
13. G. Fußmann et al., J. Nucl. Mater. 145-147 (1987) 96.
14. S. A. Cohen, S. Bernabei, R. Budny et al., J. Nucl. Mater. 128&129 (1984) 280.
15. O. Gehre, O. Gruber, H. D. Murmann et al., Phys. Rev. Lett. 60 (1988) 1502.
16. Max-Planck-Institut für Plasmaphysik, Garching, FRG, Annual Report 1987, p. 22.
17. H. J. Verbeek et al., this conference.
18. Wen Min Wang, J. Roth, R. Behrisch et al., this conference.

19. E. R. Müller, M. Keilhacker, K. Steinmetz et al., J. Nucl. Mater. 121 (1984) 138.

20. G. Fußmann et al., this conference.

FIGURE CAPTIONS

Fig. 1. Energy distribution of charge exchange neutrals for various discharges measured at the main chamber wall using carbon resistance probes for an ohmically heated (OH) discharge, for discharges with 1.3 MW neutral beams injected in co-direction (CO) and counter-direction (ctr), and for pellet refuelling with ohmic heating and two MW neutral beam heating.

Fig. 2. Impurity flux density released by charge exchange sputtering at the wall estimated from the CRP measurements versus cylindrical safety factor q(a) for different ohmic discharges ($\bar{n}_e = 4.5 \times 10^{13}$ cm^{-3}) and a series of neutral beam heating in co-direction ($\bar{n}_e = 2.8 \times 10^{13}$ cm^{-3}). For comparison the density variation at the radial position of the protruding protective limiter being close to the carbon resistance probe is plotted.

Fig. 3. Sputtering by charge exchange neutrals calculated from CRP measurements versus total heating power for various discharges: Ohmic heating (o), neutral beam heating in co-direction (Δ) and in counter direction (∇), (◇) H-mode, ion cyclotron heating (□) and lower hybrid heating (⊠). Pellet refuelled discharges are marked by a cross (+). For comparison fluxes evaluated from spectroscopic data are given (◐). Open symbols are used for the new divertor geometry while full symbols mark results obtained during the old divertor configuration of ASDEX.

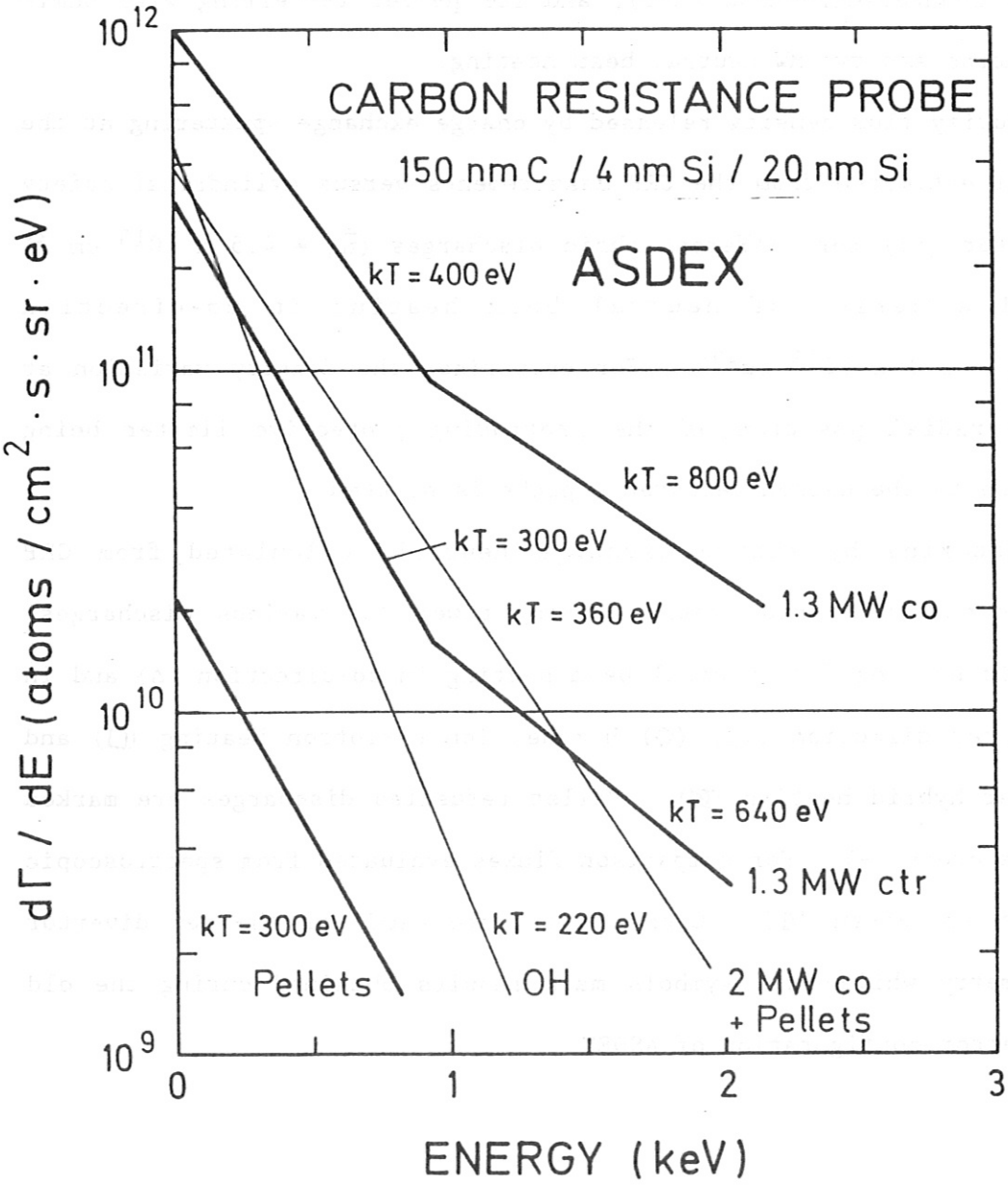
CARBON RESISTANCE PROBE
150 nm C / 4 nm Si / 20 nm Si
ASDEX
kT = 400 eV
kT = 800 eV
kT = 300 eV
kT = 360 eV
1.3 MW co
kT = 640 eV
1.3 MW ctr
kT = 300 eV
Pellets
kT = 220 eV
OH
2 MW co
+ Pellets
10^{12}
10^{11}
10^{10}
10^{9}
0
1
2
3
ENERGY (keV)
dΓ / dE (atoms / cm^2 · s · sr · eV)

Fig. 1

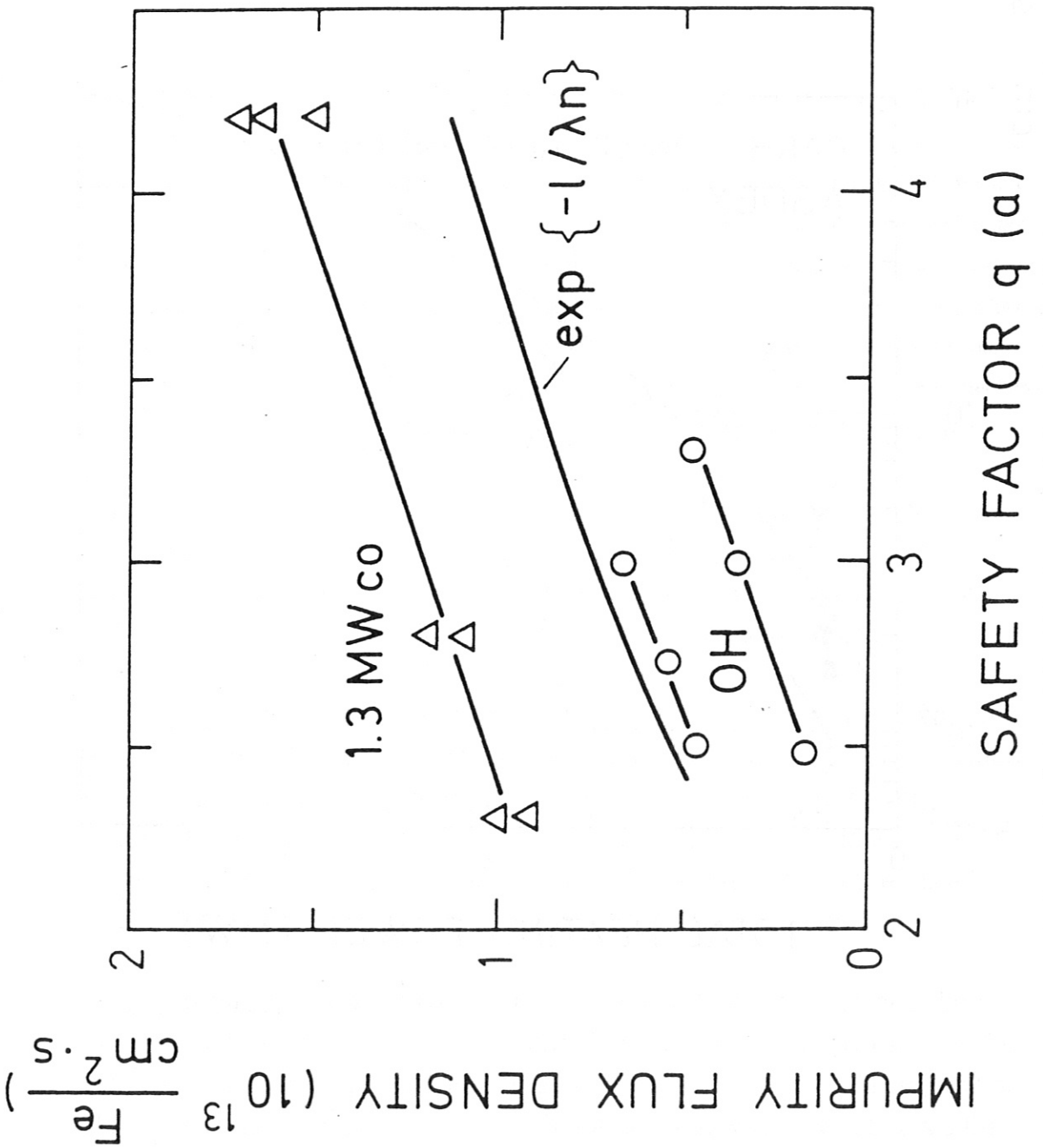
IMPURITY FLUX DENSITY (10^{13} $\frac{Fe}{cm^2 \cdot s}$)
SAFETY FACTOR q (a)
2
1
0
2
3
4
1.3 MW co
exp {-1/λn}
OH

Fig. 2

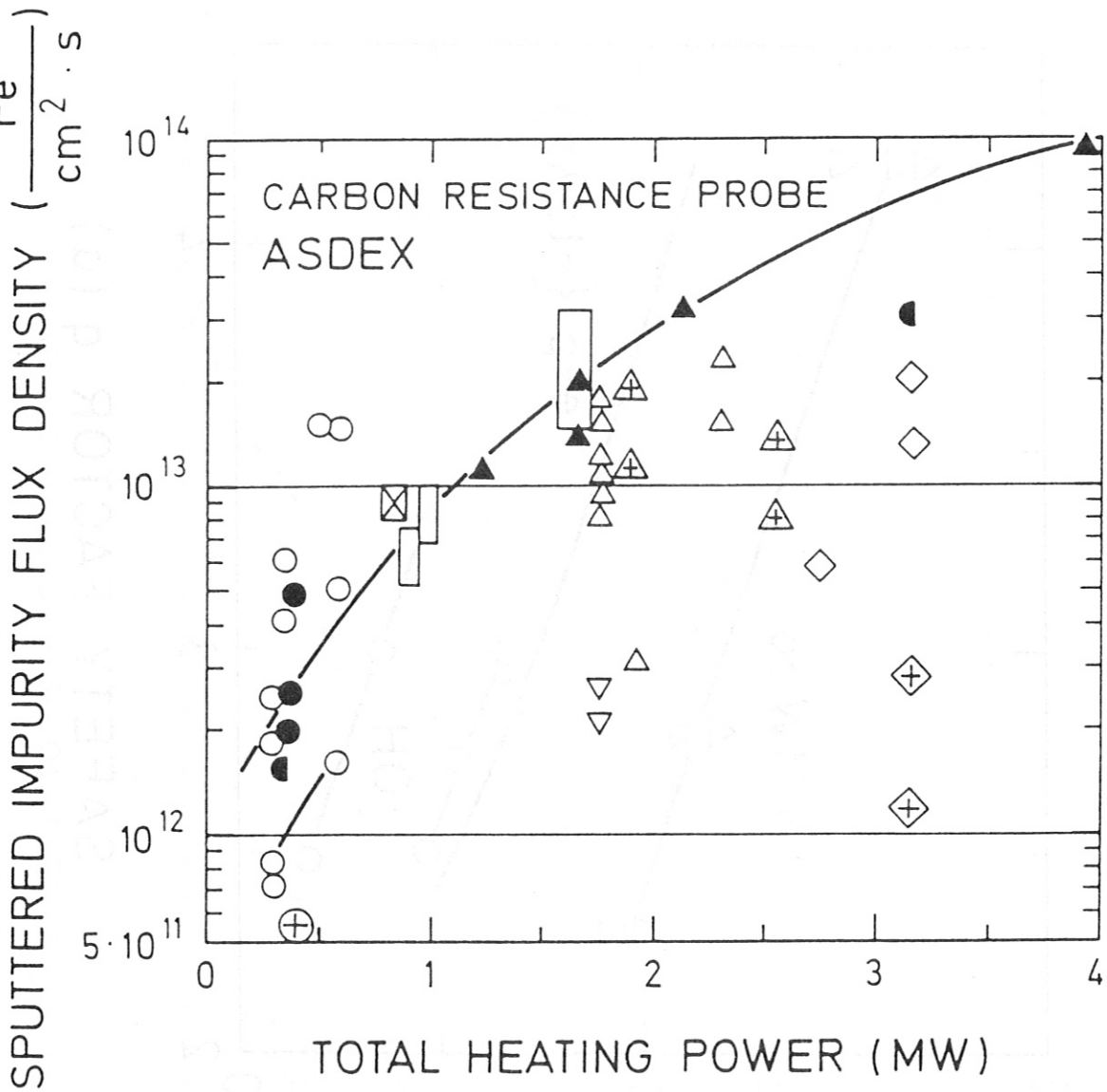
SPUTTERED IMPURITY FLUX DENSITY (Fe / cm² · s)
CARBON RESISTANCE PROBE
ASDEX
10^14
10^13
10^12
5·10^11
0
1
2
3
4
TOTAL HEATING POWER (MW)

Fig. 3

Erosion and Retention of the target plate material in the ASDEX Divertor

G. Janeschitz, G. Fussmann, J. Hofmann, L.B. Ran*, H.R. Yang*,
J. Roth, E. Taglauer, ASDEX, NI, ICRH -Teams
Max Planck-Institut für Plasmaphysik, EURATOM Association, Garching, FRG
* Southwestern Institute of Physics, Leshan, P. R. of China

ABSTRACT: In this paper we describe experiments undertaken to evaluate the retention of target produced impurities in the ASDEX divertor. The titanium divertor plates have recently been replaced by water-cooled copper plates. Since copper is a material not previously present inside the ASDEX torus, a unique possibility existed to study the transport of the target plate material from the divertor chamber into the main plasma. By spectroscopic measurement of the Cu flux emerging from the target plate and of the Cu density in the main plasma, the retention is assessed. We find a poor retention (R=1) for low n_e ($n_e < 3.0*10^{13}cm^{-3}$) but a substantially improved one (R>30) at high densities. During additional heating (NI, ICRH) at the same density as in the OH case, the retention is lower, but approaches similar values at slightly higher densities. The retention seems to be independent of the heating power.

Introduction : In this paper we report on experiments carried out to investigate the capability of the divertor for retaining metallic impurities produced by sputtering at the neutralizer plates. Previous investigations /1/ indicated a very poor retention in the case of low density ($n_e \leq 2*10^{13}cm^{-3}$) beam heated L- discharges.
A major reconstruction of the ASDEX divertor was undertaken in 1986 to allow long pulse heating (6MW, for 10sec.). In this connection the previous titanium divertor plates were replaced by water cooled copper plates - a material not previously used inside the torus vessel. This situation therefore offered a unique possibility to study the transport of the target plate material from the divertor chamber into the main plasma.

Cu flux measurements : The Cu flux profiles in front of the target plate were determined by absolutely calibrated visible spectroscopy (3247 Å Cu I line) using a scanning mirror for the spatial resolution (Fig. 1). The position of the separatrix, which coincides with the position where we observe the maximum Cu flux, depends on the ratio of the current in the divertor multipole coils to the plasma current. Cu flux profiles were measured during three different series of plasma discharges with current ratios I_{mp} / I_p = 0.64, 0.68 and 0.72. The full width at half maximum of the two profiles with higher current ratio is 2 cm while the one with a current ratio of 0.64 is 3 cm. The broader profile can be understood by the smaller

poloidal angle at which the proton flux hits the target plate.
We find a substantial increase (> factor 5) in the eroded target fluxes of copper compared with titanium /2/, in rough agreement with the ratio of the sputtering yield coefficients for Cu and Ti. At medium densities ($n_e \approx 3*10^{13} cm^{-3}$) we measure a total Cu flux of $1.2*10^{19} sec^{-1}$ ($\Gamma_{Cu} = 8.2*10^{14} cm^{-2} sec^{-1}$). The corresponding H^+ -flux onto the plates is estimated at $3*10^{22} sec^{-1}$ (T_i = 12 eV, ΔZ = 2 cm) /3/. From this we deduce a sputtering yield ($\gamma_{Cu}^{H} \approx 4.0*10^{-4}$) which appears compatible with measured Cu -yields for H^+./4/ The Cu fluxes decrease monotonically with n_e (Fig. 2) . This behaviour is expected from the enhanced recycling and flux amplification processes in the divertor which reduce the temperature in front of the plate. In a carbonized machine, however, the enhanced carbon influx seems to cool the plasma edge, particularly at low densities, which results in a Cu flux almost constant with n_e (Fig. 2).
We find two times higher Cu fluxes for D^+ plasmas than H^+ plasmas (carb. wall), which compares well with fluxes measured by a collector probe in the upper divertor /5/. This result is also in agreement with expectations, because the D^+ flux onto the divertor target plates is up to a factor of 10 smaller than in hydrogen ($3*10^{21} sec^{-1}$) /3/, while the sputtering yields of Cu for deuterium are a factor of 20 higher than for hydrogen (T_i = 12 eV , $\gamma_{Cu}^{D} = 8*10^{-3}$) /4/. If we compare the two cases(H^+,D^+) with metallic walls we find a much larger difference (approx. factor 4) which is not yet understood.
During additional heating with neutral beams (1.3MW) the Cu fluxes are roughly an order of magnitude above those in ohmically heated plasmas. We also find a factor of 1.3 higher fluxes in case of D^0 injection into deuterium compared to H^0 into deuterium, while pure ICRH reveales a factor of 3 lower Cu fluxes compared to the H^0 beams. In all three heating scenarios the fluxes increase linearly with the heating power.

Cu particle content in the plasma : The absolutely measured Cu XIX line intensity (273.4 A) is compared with a calculated Cu XIX intensity which is obtained from a time dependent impurity transport code using measured n_e and T_e profiles. From this comparison the Cu density profiles and the total number of Cu atoms N_{Cu} in the main plasma is obtained. The Cu particle content determined this way decreases monotonically with increasing line average density similar to the fluxes measured in the divertor. However, the decrease of N_{Cu} with rising electron density is much more pronounced than the density dependence of the Cu fluxes in the divertor, indicating a growing retention capability of the divertor with rising n_e. (Fig. 3)
In the case of neutral beam heating (1.3MW, H^0-injection) the Cu particle

content is roughly a factor of 10 higher than in the ohmic case (Fig. 3),corresponding well to the Cu flux measurements. The dependence on the line average density is similar to ohmic heated plasmas, which indicates a comparable retention capability. As already described for the Cu fluxes, the Cu particle content also rises linearly with heating power, independent of the heating method, and we find slightly higher Cu densities in the case of D^0 injection compared to H^0, ICRH reveals the lowest N_{Cu} of all three heating scenarios.
In deuterium discharges we find a factor of two higher Cu particle content compared with a pure hydrogen plasma, which is in good agreement with the ratio of the Cu fluxes in these cases.
Vertical shifts of the plasma column as small as $\Delta Z = \pm 1$ cm, used to make a transition between double null and single null configuration, are found to result in large reductions (factor of 3) of the Cu particle content in the bulk plasma. Hence for a given n_e, single null (top, or bottom) configurations are by far more favourable than double null configurations. These observations may be explained by the higher power loading of the active divertor in the single null cases which results in higher divertor densities (factor ≈1.5). As a consequence a reduction of T_i and Te and the total eroded Cu fluxes are expected, for which some evidence is found in the experiments (factor 0.7). In addition, however, an improvement of the impurity retention with growing $n_{e,Div}$ has to be assumed to explain the experimental findings.

Retention capability : To have a measure of the retention capability for target plate produced impurities we compare the probability for a Cu atom which is produced at the neutralizer plate to penetrate the main plasma, with the corresponding probability for a Cu atom originating from the main chamber wall. This retention factor R is not dependent on the particle confinement properties of the main plasma nor on the conditions (screening of impurity atoms) in the scrape off layer. In order to calculate this value we have to compare two different global confinement times for Cu.
Firstly, the Cu particle content in the plasma in connection with the measured total Cu flux originating from the target plates gives a modified global particle confinement time τ^*.

$$\tau^* = N_{Cu} / \Phi^{Div}_{Cu}$$

- which describes the probability that a Cu atom produced at the target plate enters the main plasma. (Fig. 4)
Secondly, we obtain the global confinement time τ_p for Cu atoms originating at the main chamber wall from the impurity transport code.

$$\tau_p = N_{Cu} / \Phi^{wall}_{Cu}$$

This confinement time relies on a calculation procedure which is based on extensive experimental experience. In the case of ohmic and neutral beam heated L discharges our results (impurity densities, Z_{eff} , Φ_{wall}) obtained from the above described comparison of impurity line intensity and code calculations are always in good agreement with both the measured Z_{eff} (via Bremsstrahlung radiation)/6/ and the global impurity influx obtained from the time of flight charge exchange diagnostic/7/.
The ratio between τ_p and τ^* is the above defined retention factor R

$$R = \tau_p / \tau^*$$

-which describes how much greater the probability is for a Cu atom born at the main chamber wall to enter the plasma, compared with a Cu atom originating from the target plate. Fig.5 displays the retention capability R versus density for ohmic and neutral beam heated (1.3MW) H^+ discharges in a carbonized machine. In the case of low densities ($n_e \leq 2.8*10^{13}cm^{-3}$), R is roughly unity, both for metallic and carbonized walls, which is in agreement with former investigations /1/. Retention improves considerably at densities above $n_e \approx 3*10^{13}cm^{-3}$ and reaches $R \approx 40$ at $n_e = 5*10^{13}cm^{-3}$ (ohmic heating). The shift of the retention curve to higher densities in the case of the carbonized machine could be explained by a lower plasma edge temperature due to the higher carbon influx, resulting in a lower divertor electron density and thus in a lower retention capability. During neutral beam heating the improvement of the retention starts at slightly higher densities compared with the ohmic case and displays a less pronounced density dependence (Fig. 5).
Another possible characterisation of the retention is the fraction of the Cu flux found to enter the main plasma. In order to calculate this fraction we have to divide the Cu particle content by the confinement time for Cu in the core of the plasma and compare the result with our measured Cu flux. From laser blow-off experiments we obtained τ_{Cu}=60 ms for ohmic heated- and approx. 30 ms for NI heated L- discharges, respectively. In case of the lowest density (poor retention: R≈1) we find that $\approx 1.5*10^{-1}$ of the measured Cu flux enters the plasma, while in case of high densities (R≈40) only $\approx 3*10^{-3}$ of the Cu flux is found in the plasma core (ohmic heating, carb. walls).
In deuterium discharges the retention is roughly the same as in pure hydrogen and displays a similar density dependence for both, ohmic and Ni heated plasmas.
During a power scan (0.6 to 2.4 MW) using neutral beam heating no significant dependence of the retention on the beam power could be

observed in spite of the fact that the Cu particle content and the Cu flux increases linearly with power. In other power scans (ICRH up to 2.5MW with and without additional beam heating (1.2MW)) the dependence of the retention capability on the two different heating beams (H^0 -injection, D^0 -injection) and on the combined NI , ICRH, as well as on the pure ICRH was investigated. The retainment does not seem to depend on the applied heating power, irrespective of the heating scenario (Fig 6). However, the absolute value of R seems to depend on the type of additional heating. The highest retention can be observed with D^0 beams followed by H^0 and pure ICRH. The combined ICRH with beam heating displays the same retention as the different beam types alone. The poorer retention in case of ICRH only could be explained by a cooler scrape off layer due to the enhanced impurity production, which results in a lower divertor density and therefore in a lower retention. Though the retention in the case of D^0 -beams is higher than in the two other heating scenarios, we find the highest Cu content and the highest Cu fluxes in this case, while during pure ICRH a factor of 3 less Cu is found in the plasma.

Summary : The Cu fluxes in the divertor obtained by absolutely calibrated visible spectroscopy are in good agreement with deposition probe measurements/5/ and with the expected fluxes calculated from the particle flux (H^+, D^+) impinging onto the divertor plates and from the sputtering yields for Cu. The measured flux, together with the Cu particle content in the plasma, enables a modified global particle confinement time τ^* for Cu to be calculated. Comparing the confinement time τ_p for Cu originating from the main chamber wall with τ^* allows a retention factor R to be deduced.
The retention factor R displays a strong density dependence in ohmic as well as in additional heated discharges (appr. unity for $n_e < 3*10^{13}cm^{-3}$, and $R \approx 40$ for $n_e \geq 5*10^{13}cm^{-3}$), but seems to be independent of the heating power. The single null divertor configuration displays a higher retention capability (appr. factor 2) at the same density compared to double null, which could be explained by the higher power load of the divertor in the single null case and therefore the higher divertor density, causing a better retention.

References :

/1/ G. Janeschitz, G. Fussmann, et. al. , NUCLEAR FUSION, Vol.26, No.12 (1986).
/2/ G. Fussmann, U. Ditte, W. Eckstein, et al., Journal of Nucl. Materials 128 & 129 (1984) 350-358.
/3/ G. Haas, J. Gernhardt, M. Keilhacker, et. al., Journal of Nucl. Materials

121 (1984) 151.
/4/ W. Eckstein, private communication.
/5/ E. Taglauer, A. E. Martinelli et. al., Proceedings of this conference.
/6/ K. H. Steuer, H. Röhr, D. E. Roberts, et. al., proceedings 15th EPS Conference on Controlled Fusion and plasma heating Dubrovnik 1988.
/7/ Verbeek et. al., proceedings of this conference.

Figure captions :

Fig. 1 : Experimental setup for the spectroscopic Cu flux measurements. The copper multipole shield and the scanning mirror as well as the calculated separatrix can be seen.

Fig. 2 : Total Cu flux plotted against n_e in the case of H^+, D^+, discharges (heated by both OH and NI($H^0 \rightarrow D^+$)) and under condition of carbonized and bare metal main chamber walls.

Fig. 3 : Total Cu particle content in the plasma for ohmic (metallic wall, carbonized wall) and NI heated discharges (carbonized wall, $H^0 \rightarrow H^+$) plotted against n_e.

Fig. 4 : τ_p calculated and $\tau^* = N_{Cu}^{pl.} / \Phi_{Cu}^{Div}$ for both ohmic and NI (1.3MW) heated H^+ discharges (carbonized wall).

Fig. 5 : Retention factor R ploted against n_e for ohmic (metallic wall, carbonized wall) and NI heated plasmas (carbonized wall) in H^+.

Fig. 6 : Retention factor R plotted against ICRH power for three different heating scenarios : ICRH+ NI(H^0), ICRH+NI(D^0) and pure ICRH in a mixed H^+, D^+ plasma (n_e= $3.5*10^{13} cm^{-3}$).

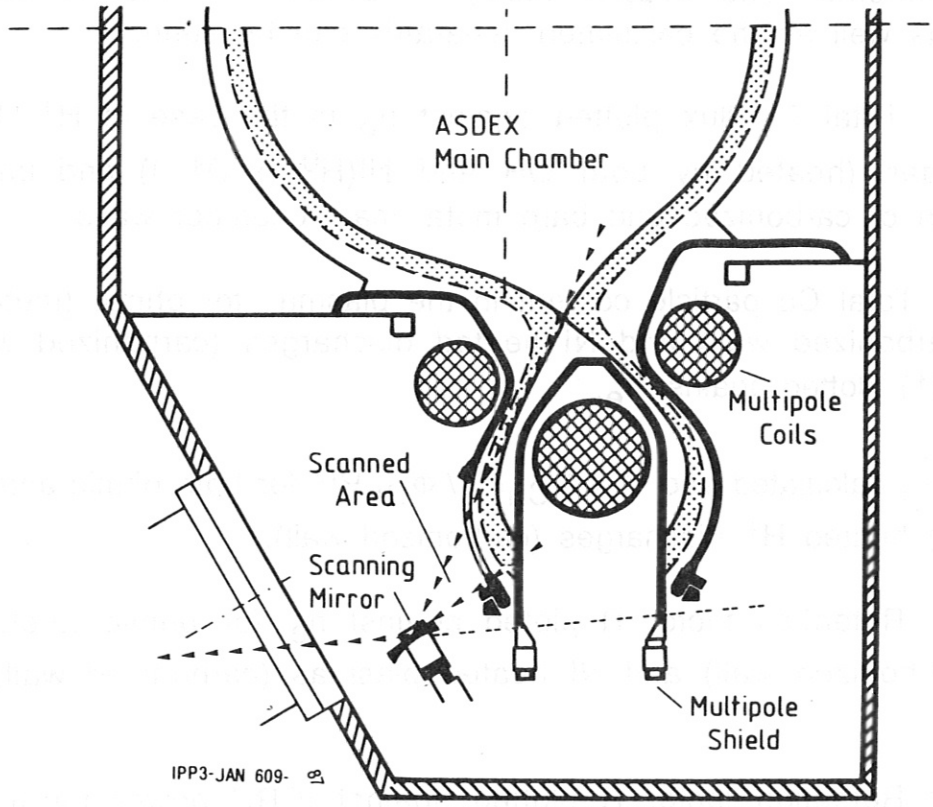

Fig. 1 : Experimental setup for the spectroscopic Cu flux measurements. The copper multipole shield and the scanning mirror as well as the calculated separatrix can be seen.

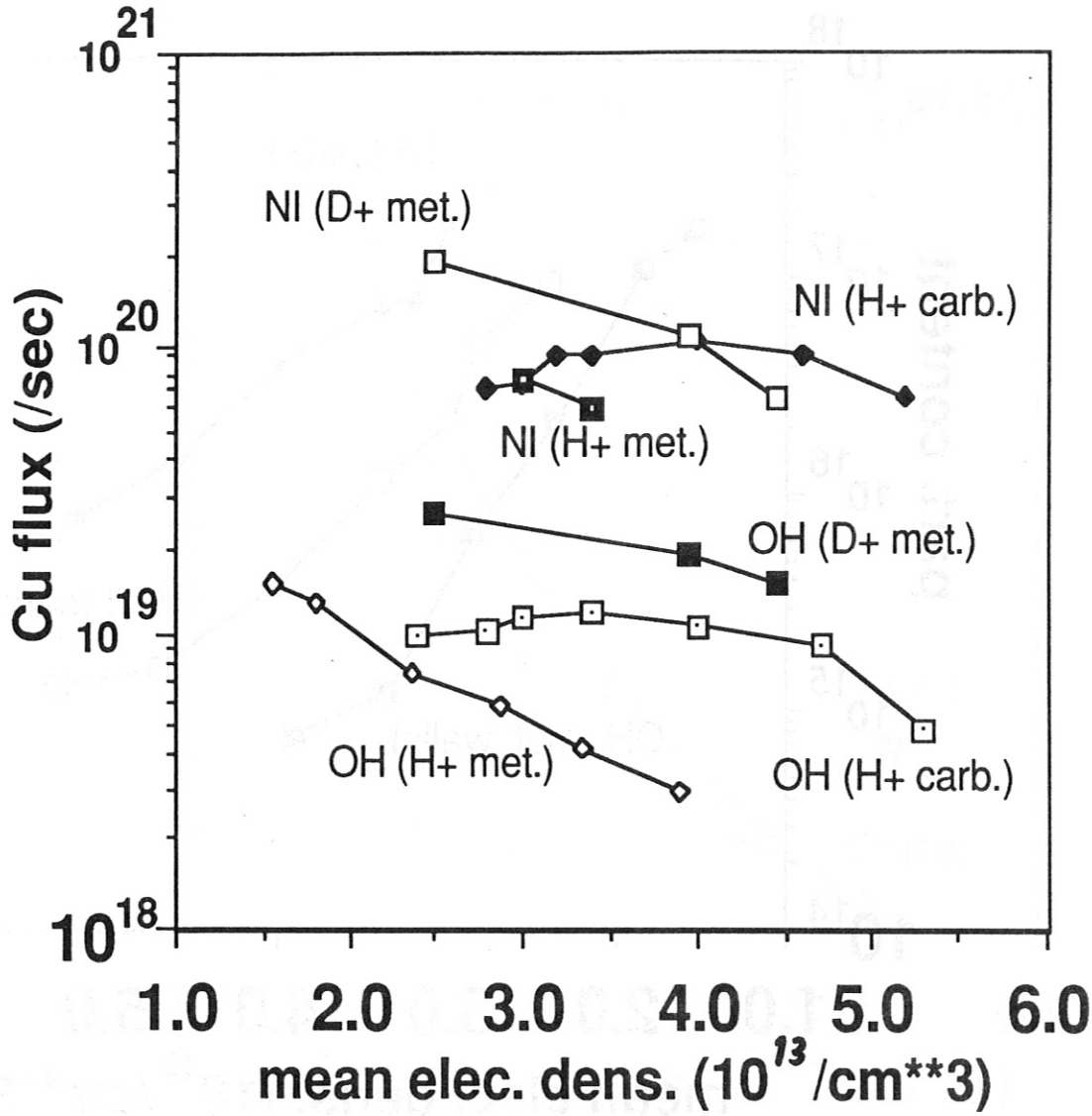

Fig. 2 : Total Cu flux plotted against n_e in the case of H^+, D^+, discharges (heated by both OH and NI($H^0 \rightarrow D^+$)) and under condition of carbonized and bare metal main chamber walls.

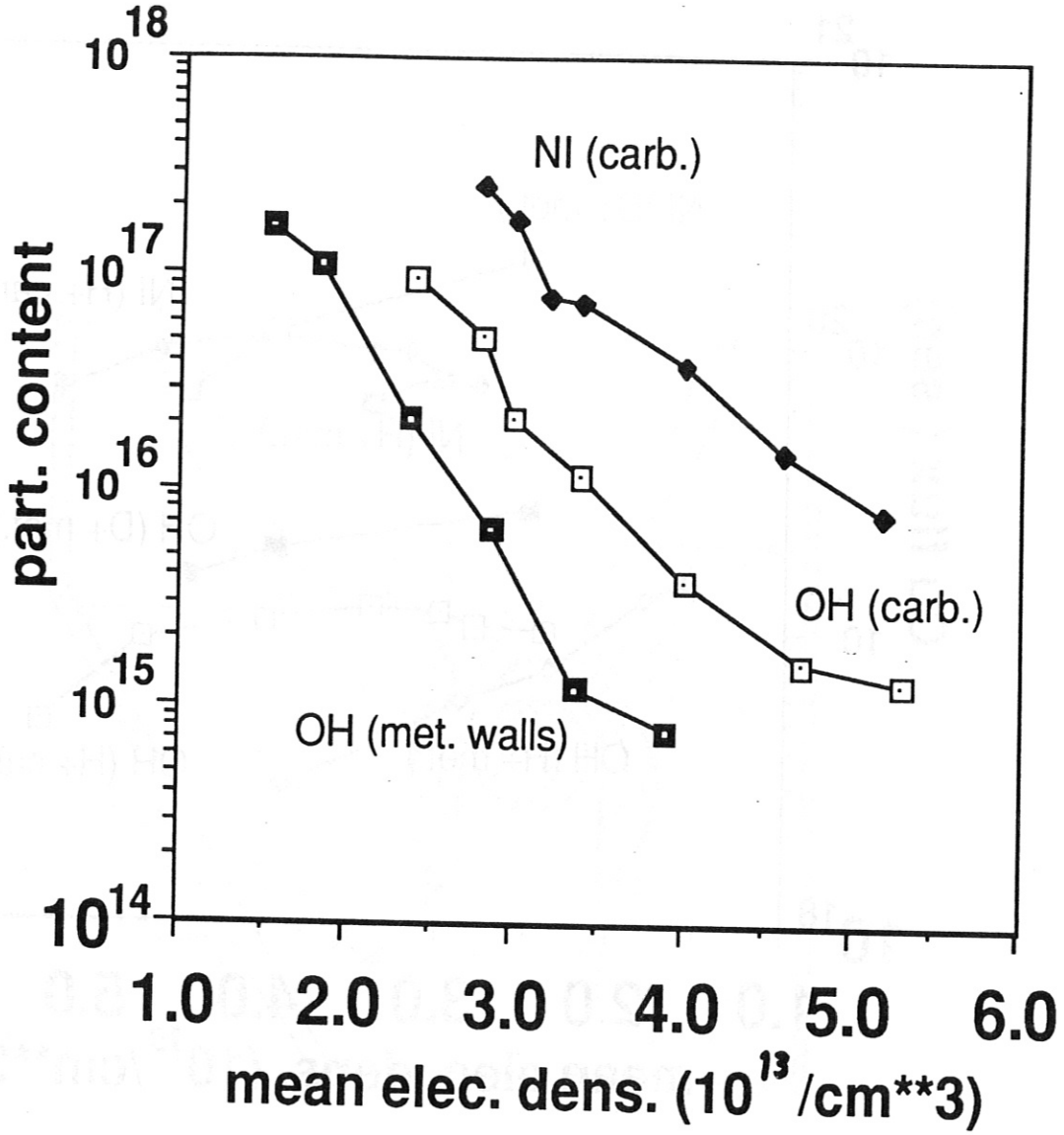

Fig. 3 : Total Cu particle content in the plasma for ohmic (metallic wall, carbonized wall) and NI heated discharges (carbonized wall, $H^0 \rightarrow H^+$) plotted against n_e.

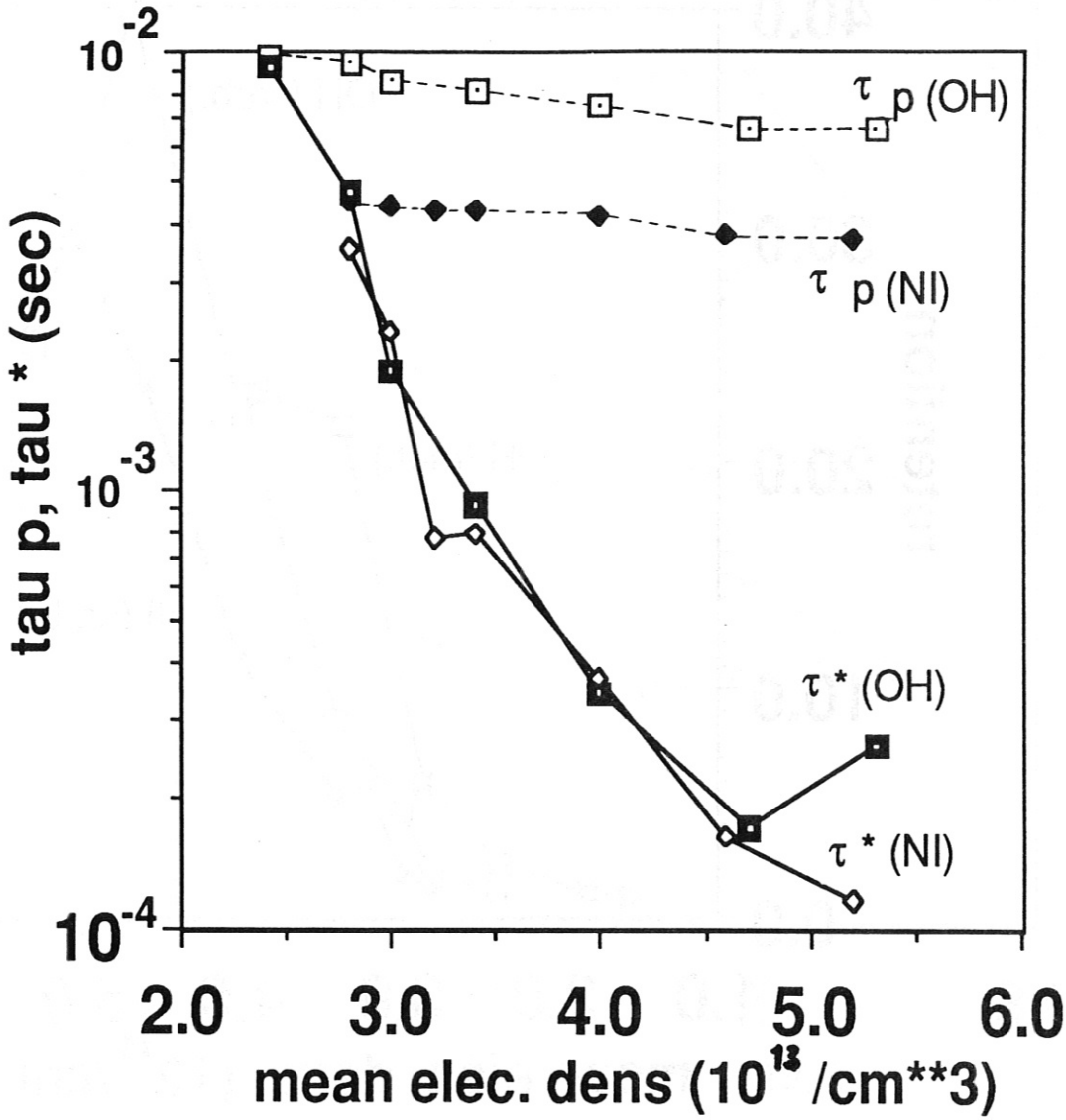

Fig. 4 : τ_p calculated and $\tau^* = N_{Cu}^{pl.} / \Phi_{Cu}^{Div}$ for both ohmic and NI (1.3MW) heated H^+ discharges (carbonized wall).

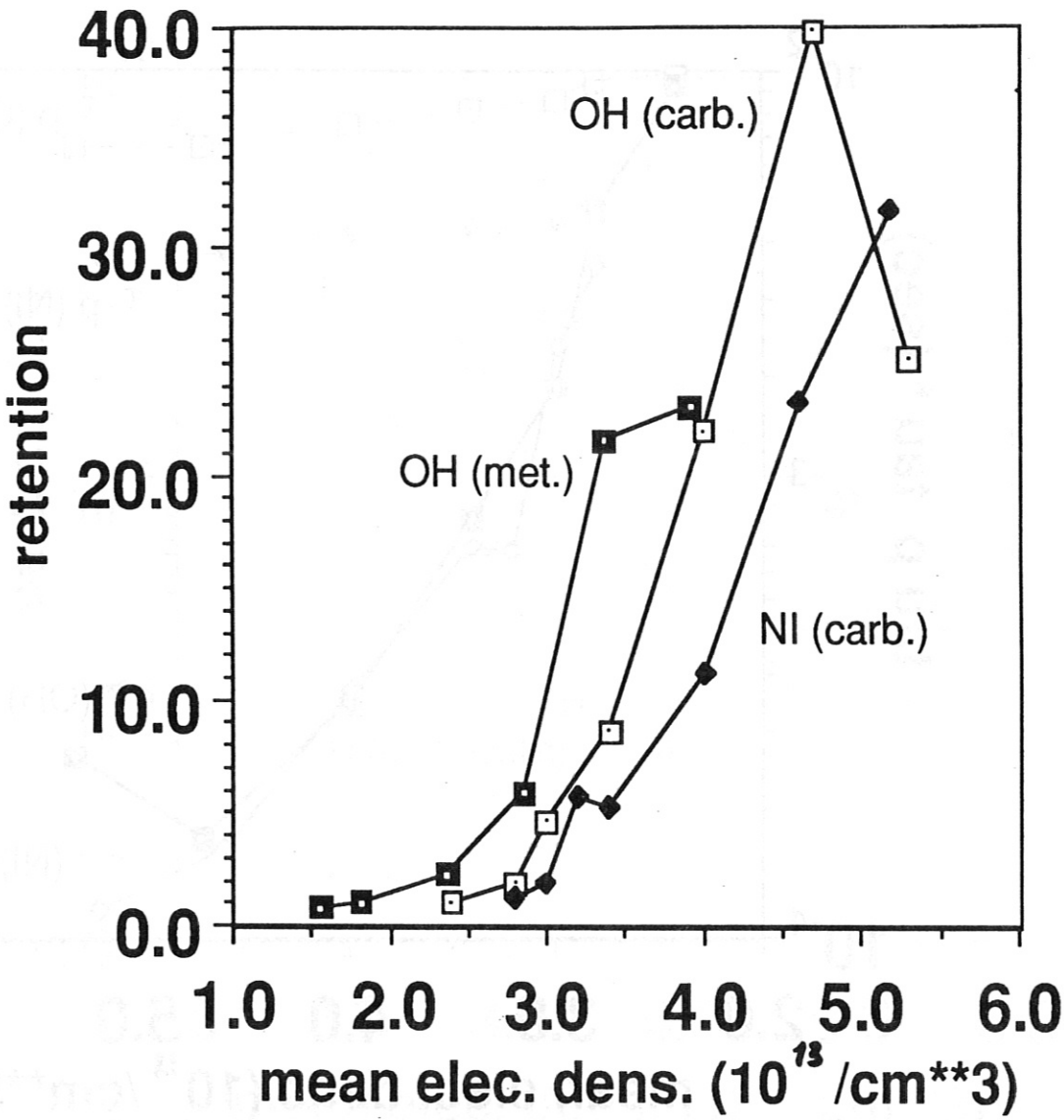

Fig. 5 : Retention factor R ploted against n_e for ohmic (metallic wall, carbonized wall) and NI heated plasmas (carbonized wall) in H^+.

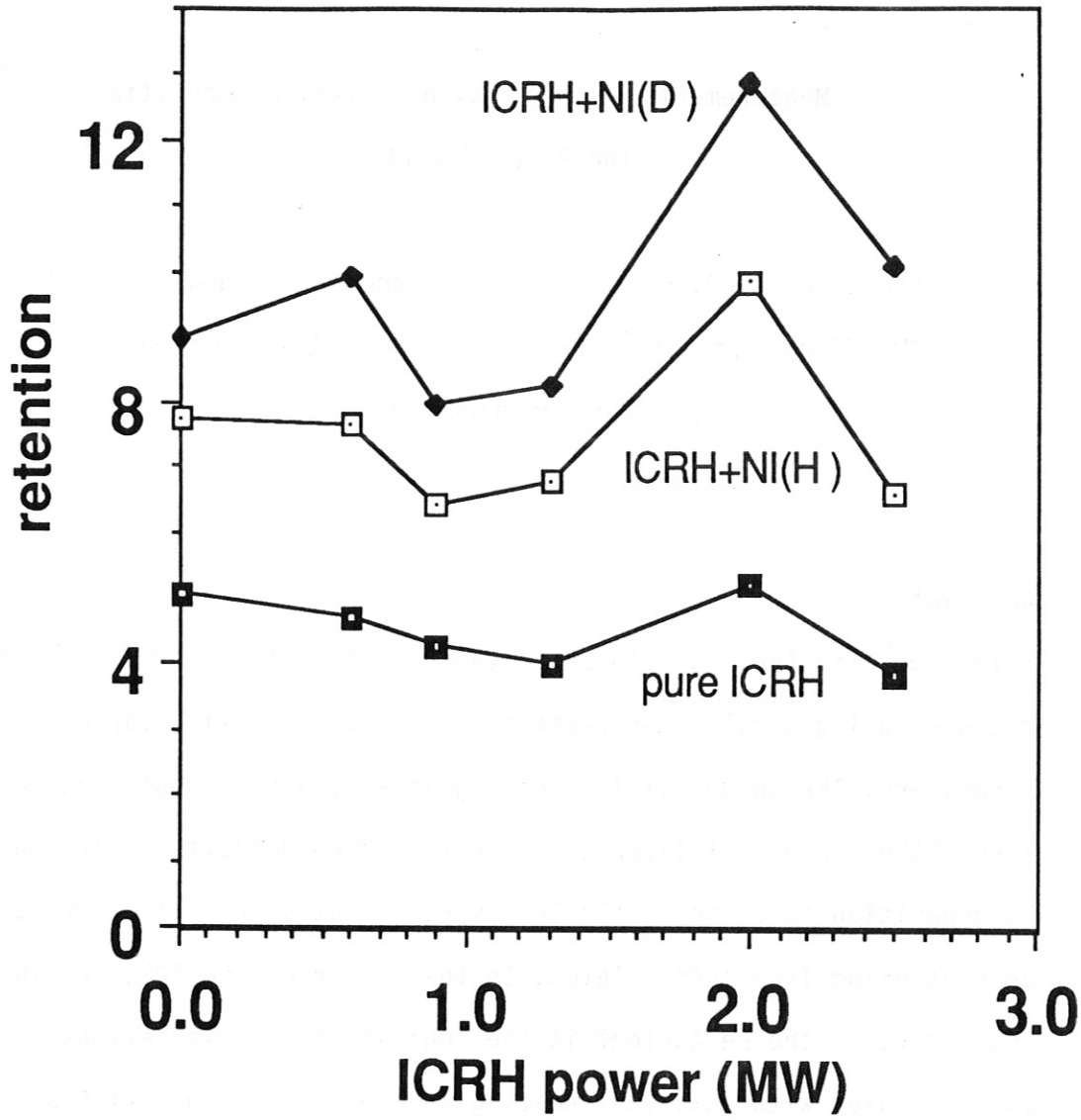

Fig. 6 : Retention factor R plotted against ICRH power for three different heating scenarios : ICRH+ NI(H^0), ICRH+NI(D^0) and pure ICRH in a mixed H^+, D^+ plasma (n_e= $3.5*10^{13}cm^{-3}$).

Measurements of the flux of metallic impurities to the ASDEX divertor plates

E. Taglauer, A.-P. Martinelli , G. Janeschitz, and the ASDEX Team

Max-Planck-Institut für Plasmaphysik, EURATOM Association,

D-8046 Garching/München, FRG

Abstract

Metal impurity (Fe, Cu) fluxes to the divertor plates of ASDEX were measured using a collector probe during discharges with various plasma parameters. The Cu deposition shows generally a different distribution across the scrape-off layer compared to the Fe deposition. The maximum Cu deposition is close to the Cu divertor plates indicating evaporation or sputtering from these plates. In the center of the SOL, Fe-fluxes are indicative of the Fe content in the central plasma. Variations of the Cu and Fe fluxes with auxiliary heating and vessel carbonisation are analysed and discussed in view of impurity production mechanisms.

Keywords: Surface probes; impurity fluxes; divertor; sputtering

1. Introduction

In the divertor tokamak ASDEX a time resolving collector probe has been used for some time to measure particle fluxes to the divertor plates /1/. It has been shown that the measured fluxes to the probe correlate directly with spectroscopic measurements in the central plasma. In particular, iron and also oxygen fluxes, derived from the spectroscopically measured central densities by a transport model calculation /2/ agreed very well with the fluxes measured with the collector probe /1-3/. Using the divertor probe it was thus possible to measure the total impurity influx into the ASDEX plasma for various discharge and auxiliary heating conditions. The "hardening" reconstruction of ASDEX /4/ resulted in some changes which are important in this context, see fig. 1: (i) the material of the divertor plates is now copper (water cooled) instead of titanium (ii) the collector probe is in an almost horizontal position which still allows measurements across the whole scrape-off layer, but also closer to the divertor plates than before.

In this paper results are presented of impurity flux measurements under the new conditions. The data contain time resolved measurements, flux distributions across the scrape-off layer and impurity fluxes as a function of neutral beam heating power. It turns out that the copper flux is much more predominant than the titanium flux in the previous divertor arrangement.

2. Experimental

The new probe has five papyex collector strips wound around the circumference of a cylindrical drum which is rotated behind a set of five apertures, each 4 mm in diameter. Rotation velocities of 10 to 40 mm/s thus correspond to a time resolution between 100 and 400 ms. The minimum distance of the apertures from the divertor plate is 12, 26, 40, 54 and 68 mm. This is sufficient to have the innermost aperture inside the separatrix (see fig. 1). The apertures face the magnetic field lines, which intersect the divertor plates at an angle of about 5^{o} to the surface. The orientation of these apertures is such that they do not connect to the divertor plates but to the main plasma with a connection length of about 15 m to the midplane.

After exposure the collector strips are removed from the probe and analysed by Rutherford backscattering (RBS) using a 2.5 MV accelerator. Generally, coverages between 1/10 of a monolayer (roughly the detection limit) and a few monolayers are detected.

3. Results

For a number of discharges in deuterium with neutral beam injection (NI) time resolved measurements were performed in which the time resolution is just enough to separate the ohmic from the injection phase /5/. The main discharge parameters were: $\bar{n}_e = 3 \cdot 10^{13}$ cm^{-3}, $I_{plasma} = 380$ kA, $B_t = 2.2$ T. For NI powers above approximately 1 MW the innermost strip may be deteriorated due to the high power deposition. Cu fluxes close to the divertor plates are up to a factor of 10 higher than Fe fluxes.

Figure 2 shows the lateral distribution of the deposited amounts of Cu and Fe for a series of identical discharges with 2, 4, 6 and 8 sources of the NI operating. It can be seen that there is an exponential decrease of the Cu flux with distance from the divertor plates with a 1/e value of about 0.8 cm. The Cu deposit reaches maximum values of about 2×10^{16} cm^{-2}, corresponding to a flux density of 3.2×10^{16} Cu cm^{-2} s^{-1} for a NI power of 2.4 MW. this can be converted /1/ into a total Cu erosion flux of 1×10^{20} Cu/s by integrating over the entire divertor configuration. The decrease of the Cu flux with distance is much steeper than the corresponding distribution of the Fe flux. This indicates the different sources, since Fe is expected to originate mainly from the edge plasma in the discharge chamber and Cu source are apparently the divertor plates. This difference in radial distribution is further corroborated in Fig. 3 which shows the lateral Cu and Fe distribution during the ohmic phase of the same series of discharges. The Fe distribution has a flat maximum at distances between 2.4 cm and 3.8 cm from the divertor plates. The corresponding total Fe fluxes of the order of 7×10^{17} s^{-1} compare favourably to values measured before for similar types of discharges. The vessel was carbonized for this series of discharges. Measurements with the vessel not carbonized for an otherwise comparable discharge with 1.2 MW NI gave the following results. The Fe-flux in the flat maximum region is a factor of 3 to 4 higher, the same holds for the Cu flux in this region of the SOL. The high value of the Cu flux very close to the divertor plates shows no big change. This indicates that the influence of carbonization is mainly on the sources in the main discharge chamber, as would be expected. The erosion of the target plates apparently is not

very much affected by carbonization which could cause variations of the parameters of the edge plasma.

The origin of the Cu fluxes is probably sputtering from the divertor plates. A rough estimate using D fluxes to the divertor plates of 3.6×10^{21} s^{-1} /6/ and calculated Cu sputtering yields of 1.1×10^{-2} for a plasma with 15 eV ion and electron temperature and a sheath potential of 3 kT /7/ gives a value of 4×10^{19} Cu s^{-1} for an ohmic discharge. This is slightly higher but still similar to the values obtained here.

The dependence of the Cu flux on NI power is plotted in Figure 4. A variation between 10^{+19} and 10^{20} s^{-1} is obtained in the range up to 2.4 MW. A similar dependence, but with values which are higher by about a factor of three is obtained from spectroscopic measurements /8/.

Comparing the Cu results to those obtained for Ti in the preceding divertor construction it is noted that the Ti values measured were only about 10 to 20 % of the measured Fe fluxes. This is due to two reasons: The previous measurements were taken at a distance of 3.5 cm from the divertor plates, where the flux of divertor material is already greatly reduced. Secondly, the sputtering yields for D on Ti are between a factor of 2 to 5 below those for Cu in the energy range of 10 to 100 eV, which is of relevance here. Therefore the present results are roughly consistent with those previously obtained and with the assumption that the flux of divertor material arises from sputtering by plasma particles.

Conclusions

Impurity fluxes in the divertor of ASDEX as measured with the collector probe are dominated by the copper flux from the divertor plates. Close to these plates they are more than a factor of 10 higher than the Fe fluxes from the main plasma.

The Cu fluxes decrease exponentially with distance from the divertor plates, whilst Fe exhibits a flat maximum inside the SOL.

The total Cu fluxes increase from 2×10^{19} s^{-1} for ohmic discharges to 10^{20} s^{-1} for 2.4 MW NI. These values can be accounted for by deuterium ion sputtering of the divertor plates.

Figure Captions

Fig. 1 Cross section of the upper half of the ASDEX tokamak showing the divertor after the "hardening" reconstruction and the position of the collector probe in the divertor.

Fig. 2 Lateral distribution of the Cu and Fe fluxes across the SOL for various amounts of NI heating power.

Fig. 3 Lateral distribution of the Cu and Fe fluxes across the SOL for the ohmic phase of the discharges of Fig. 2.

Fig. 4 Total Cu fluxes from the divertor plates as a function of NI heating power. Square symbols: spectroscopic measurments /7/. Open circles: measurements with the collector probe.

References

/1/ E. Taglauer, J. Nucl. Mater. 128&129 (1984) 141

/2/ K. Behringer, G. Fussmann, W. Poschenrieder, E. Taglauer and ASDEX Team, Proc. 11th Europ. Conf. Contr. Fusion and Plasma Physics, EPS (Geneva, 1983) 7D II p 467.

/3/ E. Taglauer and G. Staudenmaier, J. Vac. Sci. Technol. A5 (1987) 1352.

/4/ H. Rapp, H. Niedermeyer, M. Kornherr and ASDEX-Team in "Fusion Technology 1986", Vol. 1(Pergamon Press, Oxford, 1986) p.595

/5/ A.P. Martinelli, E. Taglauer and ASDEX Team, EPS Dubrovnik, 1988.

/6/ G. Haas, private communication

/7/ W. Eckstein, unpublished

/8/ G. Janeschitz et al., this conference.

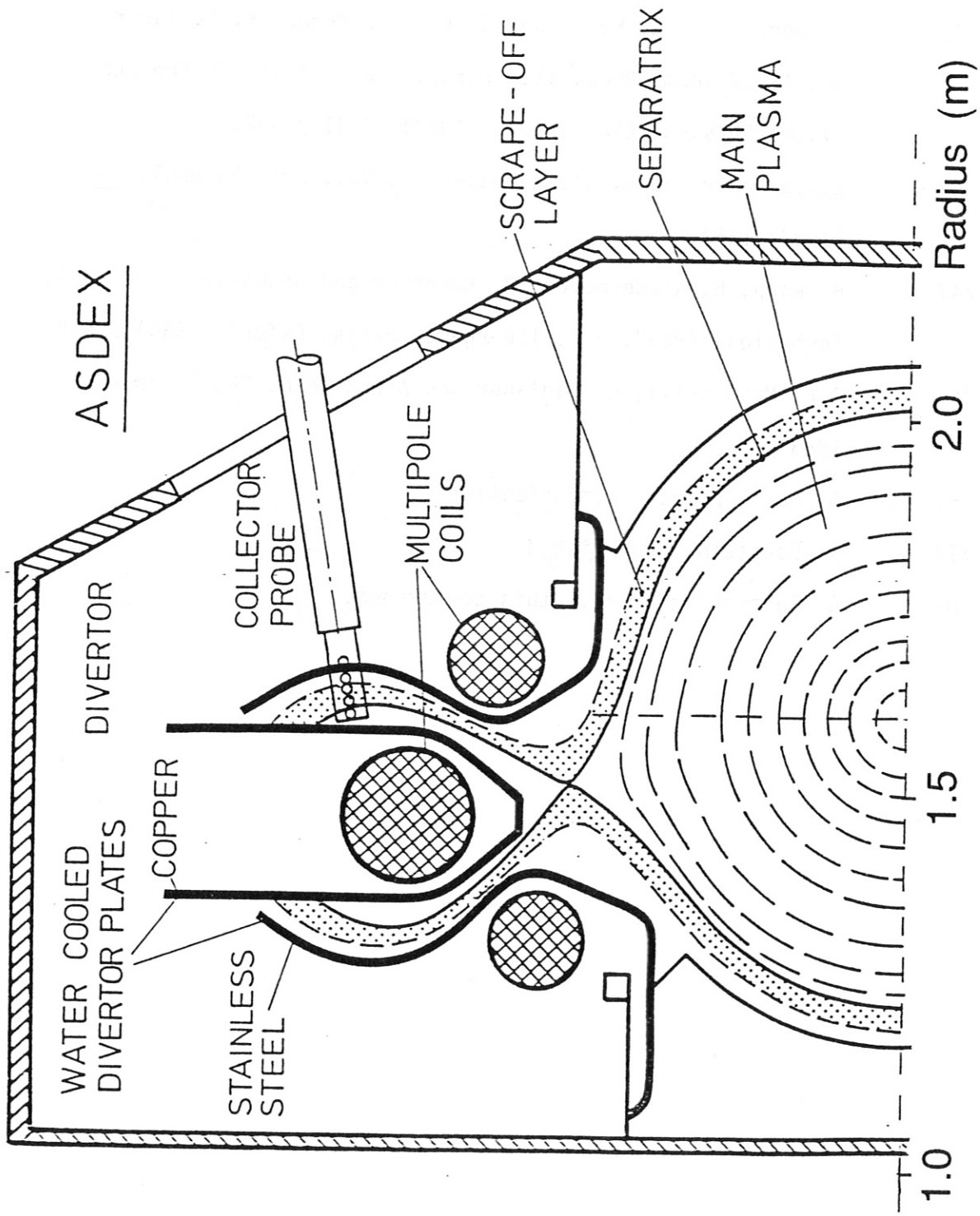
ASDEX
DIVERTOR
WATER COOLED
DIVERTOR PLATES
COPPER
STAINLESS
STEEL
COLLECTOR
PROBE
MULTIPOLE
COILS
SCRAPE-OFF
LAYER
SEPARATRIX
MAIN
PLASMA
1.0
1.5
2.0
Radius (m)

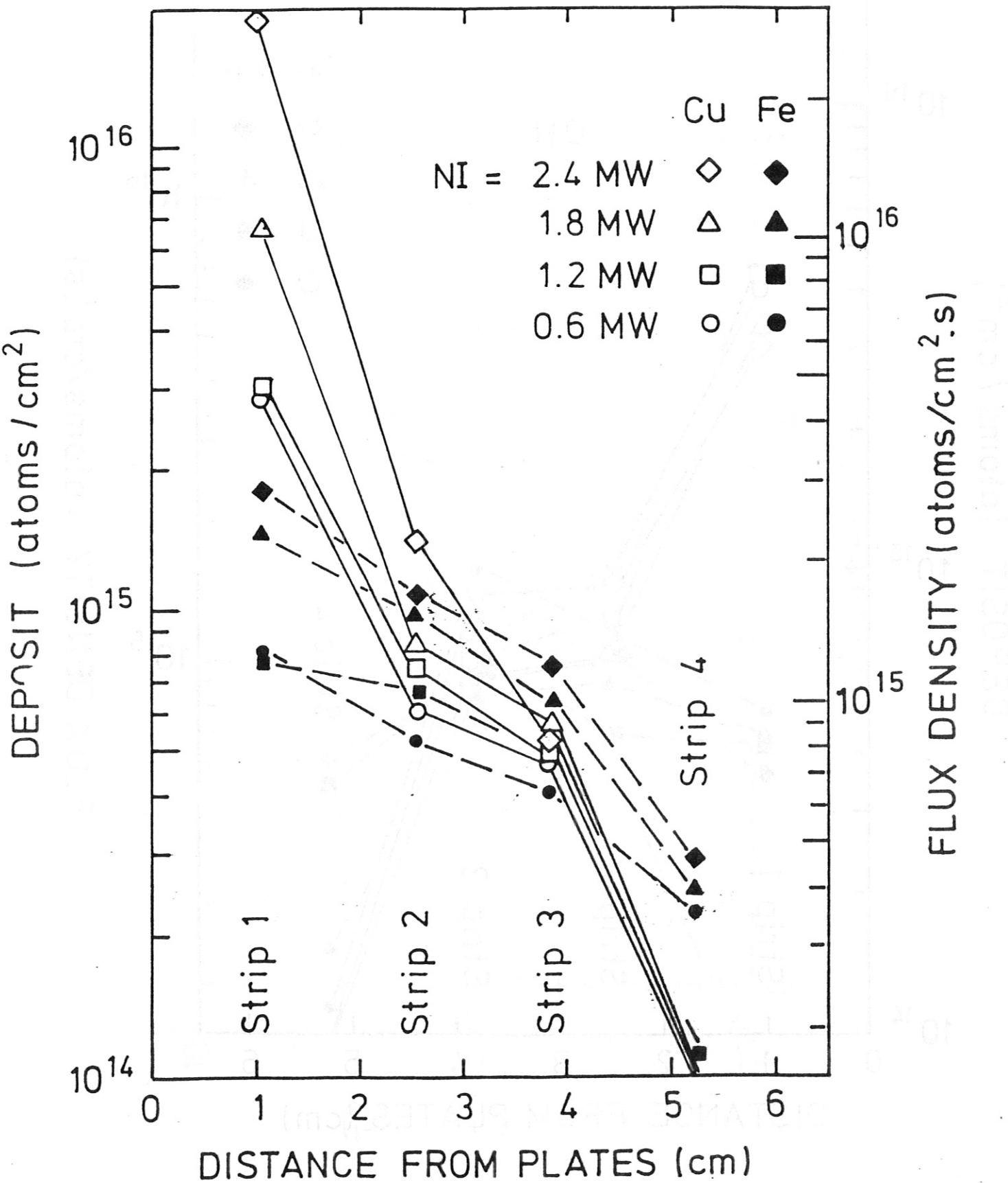
Cu Fe
NI = 2.4 MW
1.8 MW
1.2 MW
0.6 MW
Strip 1
Strip 2
Strip 3
Strip 4
DEPOSIT (atoms/cm²)
FLUX DENSITY (atoms/cm².s)
DISTANCE FROM PLATES (cm)
10¹⁶
10¹⁵
10¹⁴
0
1
2
3
4
5
6

Fig.2

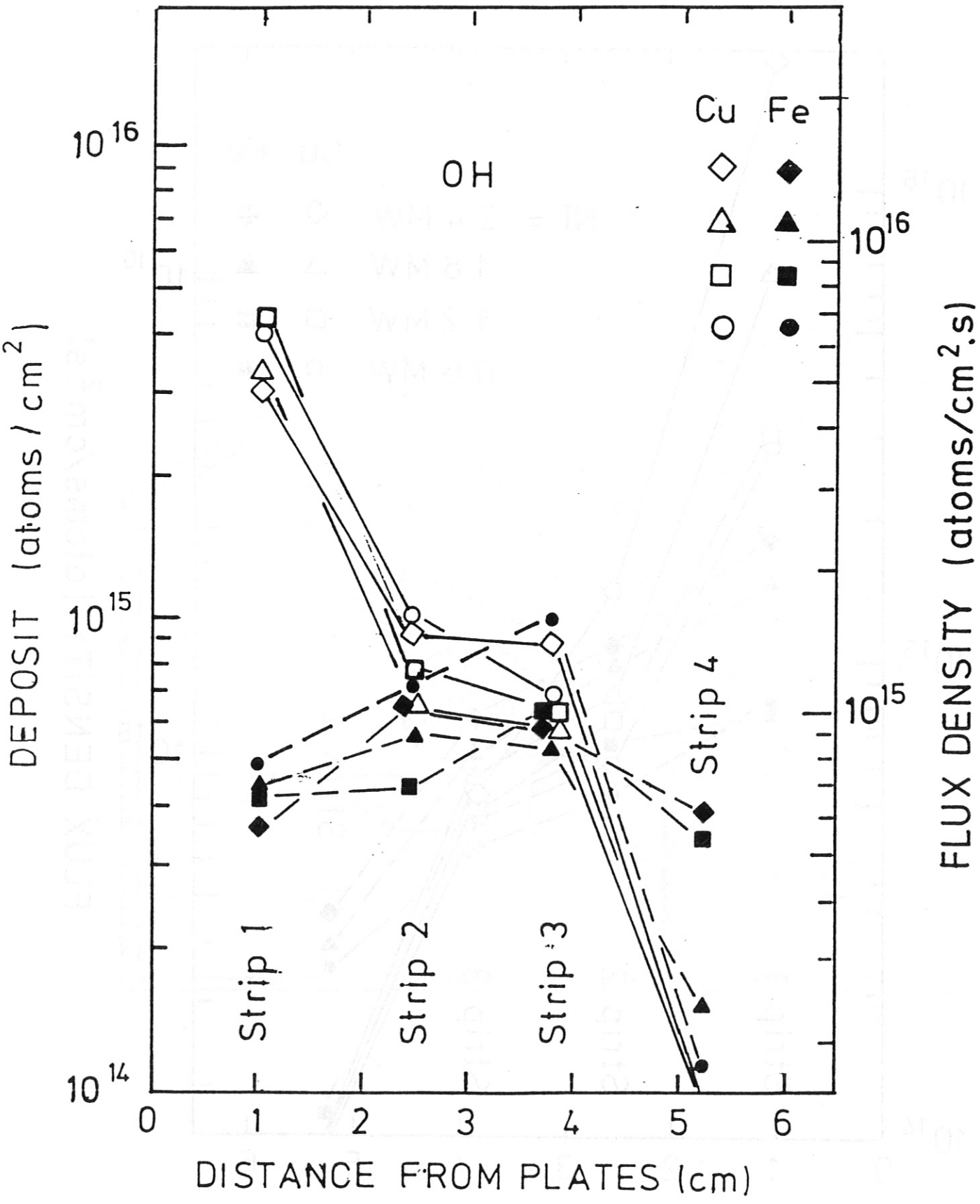
OH
Cu Fe
Strip 1
Strip 2
Strip 3
Strip 4
DEPOSIT (atoms / cm²)
FLUX DENSITY (atoms/cm².s)
DISTANCE FROM PLATES (cm)
10¹⁶
10¹⁵
10¹⁴
0
1
2
3
4
5
6

Fig. 3

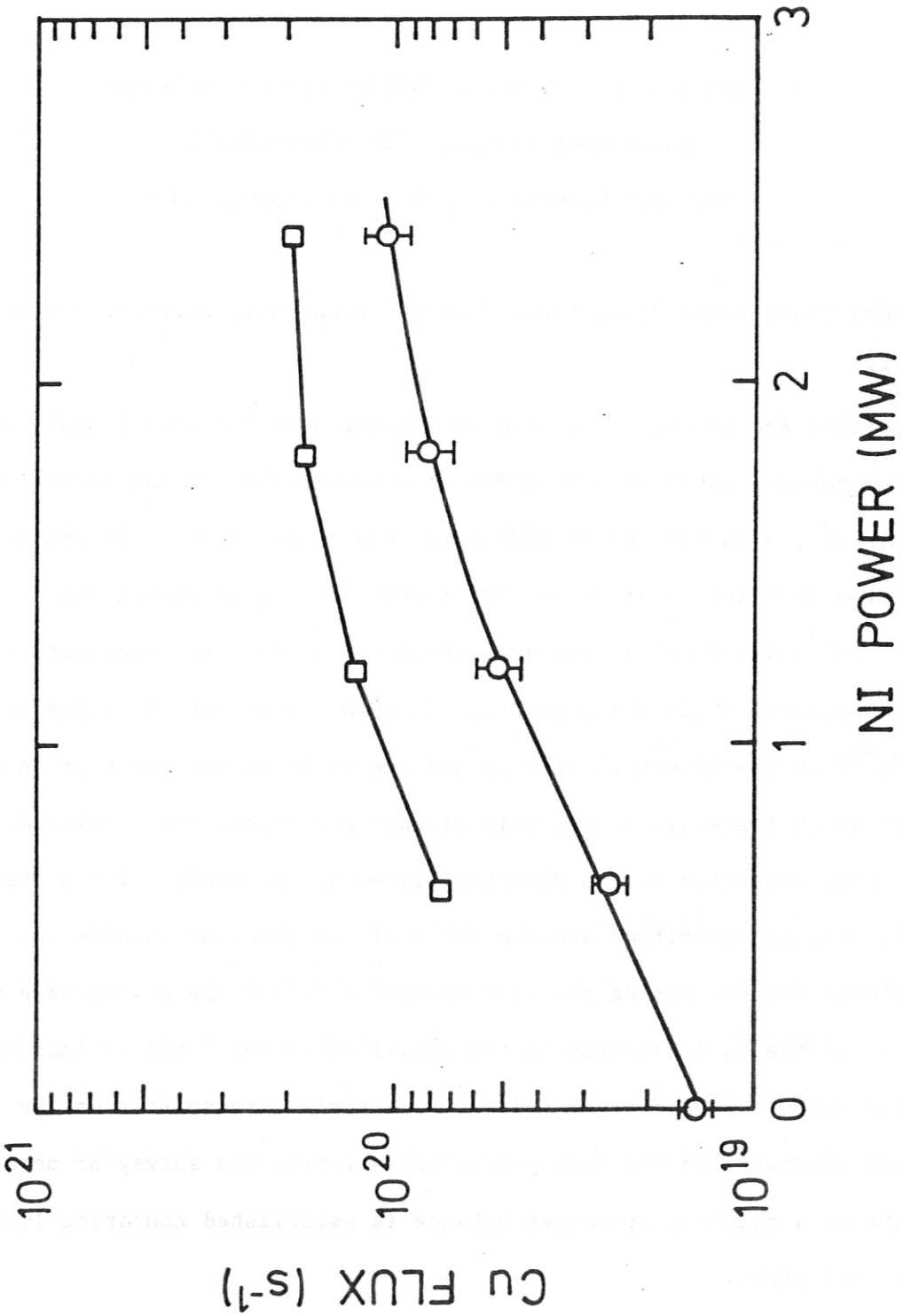

Fig. 4

Material transport at the vessel walls of the divertor tokamak ASDEX

Wen-Min Wang, J. Roth, R. Behrisch, G. Staudenmaier

Max-Planck-Institut für Plasmaphysik

EURATOM Association, D-8046 Garching, FRG

Keywords: Erosion and deposition, impurity transport, divertor retention

Abstract

Carbon tiles and probes, which had been mounted on the vessel walls of the divertor tokamak ASDEX during different experimental periods as well as the Ti divertor plates removed in 1986 have been analysed with respect to deposition of D and metal atoms. The lowest Fe, Ni, Cr deposition ($5\ 10^{15}$ cm^{-2}) was found at the area where the separatrix intersects the divertor plates, while the deposition is much larger (of the order of 10^{17} cm^{-2}) at the divertor entrance and the walls of the divertor chamber, as well as at the walls of the main discharge chamber. This indicates that metal atoms deposited at the divertor plates are re-eroded, while the final sink for plasma impurities are the walls of the divertor chamber and of the main plasma vessel. During the last operation period the plates were made from Cu and the Cu deposition on the vessel walls was found to increase with the number of discharges indicating material transport from the divertor chamber into the main plasma vessel. From the survey of metal atom desposition a material transport balance is established comparing impurity sources and sinks.

PACS: 52.75-d

Introduction

The release of metallic impurities from the vessel walls in tokamaks is of great interest, because of their large contribution to central radiation losses. For the divertor experiments ASDEX, erosion sources have already been identified, the dominant process being sputtering by charge exchange (CX) neutrals at the vessel walls /1-5/, the contribution of ion sputtering has been estimated /4/ and direct erosion measurements at the divertor plates have been performed /6/.

At the vessel walls the erosion per unit area due to sputtering by charge exchange neutrals is relatively small, compared to ion sputtering per unit area at divertor plates or limiters. In addition, erosion rates at the wall can at least partly be balanced by the deposition of impurities /7-11/. However, erosion and deposition do not necessarily occur at the same areas and long term changes in the shape of limiters and divertor plates may occur /12,13/. For a better understanding of these processes the deposition pattern becomes increasingly important.

In the past, deposition has been investigated by analysing wall structures like windows, carbon wall and limiter tiles or RF antennae /8,9,12,14/ while a systematic survey using specially designed wall collector probes was rarely attempted /7-9/. In ASDEX all these informations are now combined with results obtained from time-resolving collector probes in the plasma boundary /15,16/ to yield a comprehensive picture of long term impurity transport. The investigations have been performed for two divertor geometries, one with Ti and one with Cu divertor plate material.

Experimental

For the first divertor geometry with Ti divertor plates used between 1980 and 1986, impurity deposition was systematically monitored starting 1984 by analysing the deuterium and metal coverage of carbon tiles mounted toroidally to shield the divertor entrance slits (Fig. 1). Several of these tiles were removed and analyzed at the occasion of vessel openings and replaced by new ones. Cu observed on carbon tiles exposed in the first divertor geometry with Ti plates originated from a Cu deposit applied prior to the last discharge period in 1985 onto the Ti plates in the outer lower divertor over a length of about 3 m at a toroidal position around north-east (NE).

In 1986 the Ti divertor plates have been removed and could be investigated in detail. These results are complemented with scattered information from the analysis of other wall structures like windows /13/ and antennae /8/ in order to obtain relatively complete picture of the wall modifications. One difficulty in the interpretion of the compiled data arises, however, from the large number of discharges (about 20000) accumulated on the divertor plates which include disruptions and the use of a stainless steel limiter in the initial phase of operation. In addition, the frequent use of Ti sublimation in the divertor chamber makes the conclusion about the Ti erosion and transport uncertain.

In 1986 the divertor geometry has been changed to a water cooled Cu structure for the divertor plates and water cooled stainless steel shields forming the divertor entrance which now extend further into the divertor chamber opposite to the divertor plates. In this new geometry the erosion of Cu at the divertor plates was monitored spectroscopically /17/ and the

distribution of Cu in the divertor and main plasma chamber was followed with the use of collector probes. These probes, made of polished pyrolytic graphite were installed in the main discharge chamber at the vessel walls toroidally in the outer and inner midplane and poloidally in two positions (NNE and WSW). At the same poloidal positions, in addition, Al collector probes were inserted into the stainless steel shields opposite to the Cu-divertor plates (Fig. 2). To obtain Al-probes with high purity surfaces about 1 /um of pure Al was evaporated onto the probes prior to the installation. One major opening of the divertor chamber after 2 months of operation also provided the opportunity to investigate the Cu plates visually. Dark deposits on the Cu-plates could be stripped using adhesive tape to uncover the shiny Cu-surface and the stripped material was analyzed for its composition. To distinguish deposition during normal plasma operation and the initial glow discharge cleaning of the main vessel in this period additional probes were inserted in a wall position using a manipulator during glow discharges only.

The analysis of the wall probes was done in general by ion beam methods like nuclear reactions for D detection as well as PIXE and RBS for metal determination. In addition, X-ray fluorescence using a Cu K_α source was used to investigate the Ti plates. A lateral distribution of the stainless steel components could be obtained by analysing the plates on air without cutting. By stripping the deposited layer with adhesive tape also the Ti content of the deposit could be determined. The morphology of the deposited films was investigated in a SEM.

Results

a) Old geometry, Ti plates.

The toroidal distributions of the main metallic impurities and deuterium were rather uniform both, in the old geometry, as well as in the new one. Figure 3 shows an example for stainless steel, Ti and deuterium measured on the carbon tiles mounted on the outer and inner entrance shield of the lower divertor. The composition of the deposits deviates slightly from the bulk composition of the vessel wall material showing an enrichment of Cr of about 2%. This can be explained by preferential sputtering of segregated surface layers from the stainless steel wall /18/.

In contrast to the toroidal uniformity in the main chamber the distributions at the divertor entrance show pronounced variations. The poloidal distribution of stainless steel, Ti, Cu and D around the divertor entrance slits in the toroidal position ESE was shown already in Fig. 1. All metals show a peak in the deposition at the edges facing the entrance of the divertor. Especially the distribution on the central carbon tiles show pronounced maxima at edges closest to the plasma. The deposition for Ti found on this central tile, which was only mounted in the upper position, was the highest deposition measured, while for Fe and Cu the deposition on the inner and outer carbon ribs was higher. D deposition does not show such pronounced variations as the metals, the deposited amount being of the order of 2×10^{17} D/cm^{+2}. For all metals the deposition on the lower carbon ribs showed a pronounced assymetry, being larger at the outer bottom entrance shield than at the inner bottom shield. Impurities like Ca, K, Cl are predominantly deposited on the lower carbon tiles. For the divertor plates the lateral distribution of iron deposition across the

separatrix is shown in Fig. 4. At the location of the separatrix intersection, were the largest deposition is expected, the smallest depostied amounts are actually found. This can be seen, more pronounced on the outer divertor plates than on the inner ones. Other than iron the deposited film contains about 30% Ti and only little C.

b)New geometry, Cu plates

The toroidal distribution of metals like Fe, Ti, and Cu at the outer midplane as shown in Fig. 5 exhibits little variations. Only elements with strongly localized sources, such as Au from mirrors installed inside the torus, also showed corresponding deposition maxima close to the source. While Fe originates from the wall material and Cu from the divertor plates, Ti must be a wall contamination from the former period susing Ti divertor plates. At the occasion of short openings during the operation periods several collector probes could be exchanged. The analysis of collector probes exposed for different numbers of discharges shows, that Fe and Cu deposition increases proportional to the number of discharges, while the Ti deposition decreases with time. The relation of deposited wall material to divertor material is roughly the same as in the old geometry.

The poloidal distribution of the deposition was shown already in Fig. 2 for two toroidal positions and for two experimental periods. While in the main plasma chamber iron is the dominant deposited metal, in the divertor chamber copper exceeds the iron deposition at positions closest to the intersection of the separatrix with the divertor plates. The comparison of the two discharge periods shows similar distributions of the depositions, but increasing with the number of discharges such that an average number of

deposited material per discharge or exposure time can be calculated. Ti originating mainly from depositions on the vessel wall from former discharge periods can be found in the divertor only in very spurious amount below 10^{15} cm^{-2}. After the first discharge period the deposited layer on the divertor plates could be removed using adhesive tape and analysed by RBS and X-ray fluorescence. While at the separatrix location the copper plates were blank, a black deposited layer of Cu, Fe was found at more lateral positions. The oxygen concentration indicated a fully oxidized layer of 3×10^{17} cm^{-2} of Cu and 2×10^{17} cm^{-2} Fe with only small amounts of carbon extending laterally away from the plasma for about 2 cm.

Discussion

For both, the old and new divertor configuration the deuterium and most metal deposits are toroidally rather uniform except for elements from a localised source, such as the Au mirrors (Figs. 3 and 5). This indicates a uniform impurity source for Fe, Cu, and Ti and this is in agreement with previous conclusions, that the main source for Cr, Fe, Ni is the uniform wall bombardment with CX-neutral /1-5/. The source for divertor material is ion sputtering at the plates being also toroidally uniform. For the old geometry, Cu was applied only locally in the NE section of the lower divertor. After transport into the main vessel, however, this localized source also spreads out uniformly as determined by time resolving collector probes in the main chamber and the opposite divertor /19/. The level of deuterium of $2 \cdot 10^{17}$ D/cm^2 corresponds to a surface saturation for ions with energies of 500 eV assuming a maxwellian energy distribution /20,21/. This is of the order of the mean energy of CX-neutrals from typical ASDEX discharges /3/. The measured deuterium levels may, however, be influenced by codeposition with carbon atoms, which cannot be assessed on graphite samples.

The poloidal distribution of metallic deposits around the divertor entrance slits was measured in the old geometry. The dependence of the deposit on distance from the separatrix, as seen in Fig. 1, indicates that here the impurities are at least partly deposited as ions following magnetic field lines. This is especially true for Ti and Cu which in this case are not produced in the main chamber. The center upper carbon tile shows especially large Ti depositions and variation with distance from the plasma. Field lines reaching this plate do not originate in the plasma boundary but only from the Ti divertor plate. This suggests that deposited Ti atoms originate directly from erosion at the plates and that an impurity ion flux exists opposite to the stream of plasma ions into the divertor. Such a flux has also resulted from 2D calculations by Braams et al. /22/, however, for a different divertor geometry.

A comparison of deposition on the divertor and plasma chamber walls can be obtained for the new geometry as shown in Fig. 2. Most of the eroded divertor material is deposited on the walls of the divertor chamber and does not reach the main plasma vessel. This can be compared with the spectroscopically measured retention probability of the divertor, which is still around 80 % in the worst cases, i.e. at low plasma density /17,23/. On the average over long time operation, about only 10 % of eroded plate material is deposited in the main plasma chamber. This is in general agreement with 2D calculations by Brooks /24/, which predict the loss of only 0 to 5% sputtered W atoms to the main chamber depending on the ionization length of the atoms. This, however, was calculated for an open divertor geometry like INTOR design. For the closed divertor chamber as used in ASDEX we find about 70 % of the eroded Cu atoms on the inner divertor walls and not returning to the plates.

The divertor plate, is no final sink for eroded material. Both, the new Cu and old Ti plate exhibit far less deposition than expected from the integral erosion in the machine. Especially the observed minimum in deposition at the intersection of the separatrix with the plates, where a maximum of the deposition is expected shows that re-erosion of deposited material occurs. Deposited material is reeroded and step by step redeposited at lateral positions on the divertor plates or on the divertor chamber wall. The pattern is similar to the ones frequently observed on limiters in other tokamaks /8, 25, 26/. Time resolving divertor collector probe measurements show that deposition dominated phases alter with erosion dominated phases, such as during intense neutral beam injection /27/. From measurements integrating over longer discharge periods, it cannot be concluded whether reerosion occurs constantly or only during phases of high divertor loading. Spectroscopic measurements /23/ indicate, however, much stronger erosion during auxiliar heating like NBI and ICRH, increasing dramatically with decreasing plasma density. Thus, it seems plausible that deposition phases at the plates alter with erosion phases either during one discharge or from discharge to discharge.

The depositions measured on different wall areas can further be combined with measured and estimated erosion fluxes from the different areas in order to obtain the average particle fluxes between different vessel areas. For this purpose the depositions on the following 3 areas have been integrated for both divertor geometries: (1) main chamber wall, (2) divertor chamber wall, (3) divertor plates. The total deposits have been devided by the total discharge time. The resulting fluxes are compared in Table 1 with erosion fluxes determined previously /1-5,17,22,28,29/. In

cases, where long term erosion or deposition fluxes are compared with fluxes measured time resolved, e.g. spectroscopically or using collector probes, average values over different discharge conditions are taken. However, averaging over the time dependence may lead to errors of the order of 2. For the divertor region it can be seen, that the deposition in the divertor chamber including the divertor plates roughly balances the average flux eroded from the divertor plates. Only about 10% of the flux is finally deposited at the main chamber wall. This flux of ionized impurity atoms opposit to the streaming plasma ions is poorly understood and requires 2D calculations /22/.

Considering impurities released from the main chamber wall, such as Fe, it is surprising that about 50 % is found on collectors back at the wall, while the rest divides between divertor plates and divertor wall. 1D-transport code calculations /30,31/ predict a loss of about 25% of the ionized wall atoms bank to the wall due to cross field diffusion. The larger amount of iron redeposited on the wall may be partly due to neutral sputtered atoms which hit wall structures before being ionized in the boundary plasma. Iron atoms once deposited on the divertor plate can subsequently be treated like plate material and will be reeroded here. Again, the calculated erosion from the wall due to CX-neutral sputtering roughly balances the deposition integrated over the machine walls.

Conclusions

Using long term wall probes mounted at the wall of the ASDEX vessel and in the divertor the history of the deposition of material eroded from the wall and the divertor plates has been followed. Combining this information with results from analysing wall structure like carbon ribs and divertor plates a picture of material migration can be constructed. It can be shown that only 10 % of the material eroded at the divertor plates migrates into the main plasma chamber. This is in good agreement with the spectroscopically measured divertor retention while the origin of these fluxes is still poorly understood. More than one half of atoms eroded from the wall of the main plasma chamber, predominantly by CX-sputtering, is deposited back to the wall, while the remaining amount is found on the divertor plates and divertor wall. At the area of on the divertor plates, where the separatrix intersects, erosion exeeds deposition and metal atoms are recycled into the transport pattern of impurities.

Figure Captions

Fig. 1 Distribution of the deposition of metallic impurities on carbon ribs around the top and bottom divertor entrance of ASDEX for the old divertor geometry.
Dashed line: bottom divertor entrance.
Solid line: upper divertor entrance.

Fig. 2 Poloidal distribution of the desposition of metallic impurities in ASDEX during two operation periods in 1987 for two toroidal positions and the new divertor geometry.

Fig. 3 Toroidal distribution of the deposition of metallic impurities and deuterium in ASDEX for the old divertor geometry at the entrance shield of the main plasma chamber.
a) at the torus outside
b) at the torus inside.

Fig. 4 Vertical distribution of the net deposition of metallic impurities at the Ti divertor plates after about 20 000 discharges. The measured distribution is compared with an estimate neglecting reerosion of deposited impurities.

Fig. 5 Toroidal distribution of metallic impurities in ASDEX for the new divertor geometry at the outer torus midplane.

Table 1: Eroded and deposited metal fluyes measured by various surface probes, charge exchange neutral spectroscopy and by optical spectroscopy.

References

/1/ G. Staudenmaier, J. Vac. Sci. Technol. A3 (1985) 1091.

/2/ G. Staudenmaier, W.R. Wampler, J. Nucl. Mat. 145-147 (1987) 569.

/3/ H. Verbeek and the ASDEX team, J. Nucl. Mat. 145-147 (1987) 523.

/4/ G. Fussmann and the ASDEX team, J. Nucl. Mat. 145-147 (1987) 96.

/5/ R. Behrisch, J. Roth, G. Staudenmaier, H. Verbeek, Nucl. Instr. and Meth. in Phys. Res. B18 (1987) 629.

/6/ B. Schweer, P. Bogen, E. Hintz, D. Rusbüldt, S. Goto and K.H. Steuer, J. Nucl. Mater. 111&112 (1982) 71.

/7/ J. Ehrenberg, R. Behrisch, J.P. Coad, L. De Kock, D.H.J. Goodall, G.M. McCracken and A.P. Martinelli, J. Nucl. Mat. 145-147 (1987) 741

/8/ R. Behrisch, J. Ehrenberg, M. Wielunski, A.P. Martinelli, H. Bergsåker, B. Emmoth, L. De Kock, J.P. Coad, J. Nucl. Mat. 145-147 (1987) 723.

H. Bergsåker, R. Behrisch, J.P. Coad, J. Ehrenberg, B. Emmoth, S.K. Erents, G.M. McCracken, A.P. Martinelli and J.W. Partridge, J. Nucl. Mat. 145-147 (1987) 727.

/9/ J. Roth, J. Ehrenberg, K. Wittmaak, J.P. Coad, J.B. Roberto, J. Nucl. Mat. 145-147 (1987) 383.

/10/ H. Wolff, H. Grote, A. Herrmann, D. Hildebrandt, M. Laux, P. Pech, H.-D. Reiner, G. Ziegenhagen, V.M. Chicherov, S.A. Gashin, V. Kopecky and K. Jakubka, J. Nucl. Mat. 145-147 (1987) 671

/11/ P. Coad, R. Behrisch, J. Roth, L. De Kock, J. Ehrenberg, G. Israel, D.H.J. Goodall, Wang WenMin, M. Wielunski, Proc. 14th Europ. Conf. on Contr. Fusion and Plasma Physics, Madrid 1987, Europhys. Conf. Abstr. Vol II (1987) 74.

/12/ G. Staudenmaier, P. Staib, G. Venus, TFR-Group, J. Nucl. Mat. 76&77 (1978).

/13/ P. Staib, H. Kukral, E. Glock, G. Staudenmaier, J. Nucl. Mat. 111&112 (1982) 173.

/14/ R. Behrisch, M. Wielunski, J.M. Noterdaeme, F. Wesner et al., 14th Europ. Conf. on Controlled Fusion and Plasma Physics, Madrid (1987) Vol. II, p. 778.

/15/ E. Taglauer, B.M.U. Scherzer, P. Varga, R. Behrisch, Chen Cheng-Kai, and ASDEX Team, J. Nucl. Mat. 111&112, 142 (1982).

/16/ J. Roth, P. Varga, A.P. Martinelli, B.M.U. Scherzer, Chen Cheng-Kai, W.R. Wampler, E. Taglauer and ASDEX-Team, J. Nucl. Mat. 111&112, 123 (1982).

/17/ G. Janeschitz et al., Abstracts of the Americal Phys. Soc., Plasma Physics, San Diego, Calif. (1987).

/18/ W.-M. Wang, J. Roth, J. Behrisch, to be published.

/19/ G.Janeschitz et al., Nucl. Fus. 26, 1725 (1986).

/20/ G. Staudenmaier, J. Roth, R. Behrisch, J. Bohdansky, W. Eckstein, P. Staib, S. Matteson, S.K. Erents, J. Nucl. Mat. 84, 149 (1979).

/21/ W. Eckstein, Max-Planck-Institut für Plasmaphysik, IPP-Report 9/30 (1980).

/22/ J. Neuhauser, B. Braams, priv. communication.

/23/ G. Janeschitz , G. Fußmann, J. Hofmann, et al., this conference.

/24/ J.N.Brooks, J. Nucl. Mat. 145-147, 837 (1987).

/25/ R.T.McGrath, B.L.Doyle, J.N.Brooks, A.E.Pontau, G.J.Thomas, J. Nucl. Mat. 145-147, 660 (1987).

/26/ G.McCracken, D.Goodall, J.Roth et al., this conference.

/27/ J.B.Roberto, J.Roth, E.Taglauer, O.W.Holland, J. Nucl. Mat. 128&129, 244 (1984).

/28/ E.Taglauer, G.Staudenmaier, J.Vac. Sci. Techn. A5 1352 (1987).

/29/ E. Taglauer, A.P. Martinelli, this conference.

/30/ K. Lackner, K. Behringer, W. Engelhardt, R. Wunderlich, Z. Natur. 37a, 931 (1982).

/31/ G. Fußmann, Nucl. Fusion 26, 983 (1986).

/32/ G. Staudenmaier, W.R. Wampler, this conference.

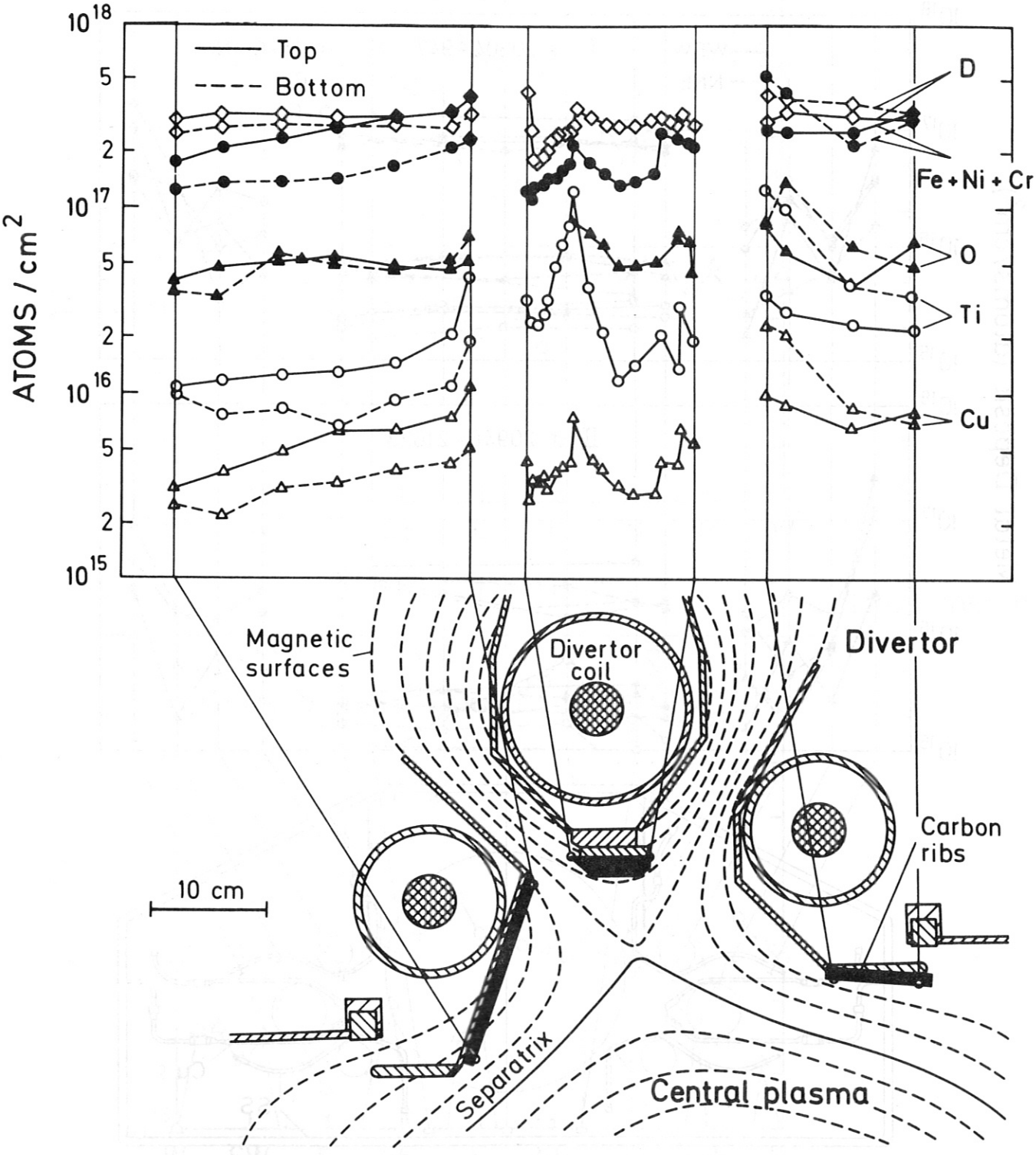
ATOMS / cm²
10¹⁸
5
2
10¹⁷
5
2
10¹⁶
5
2
10¹⁵
Top
Bottom
D
Fe + Ni + Cr
O
Ti
Cu
Magnetic surfaces
Divertor coil
Divertor
Carbon ribs
10 cm
Separatrix
Central plasma

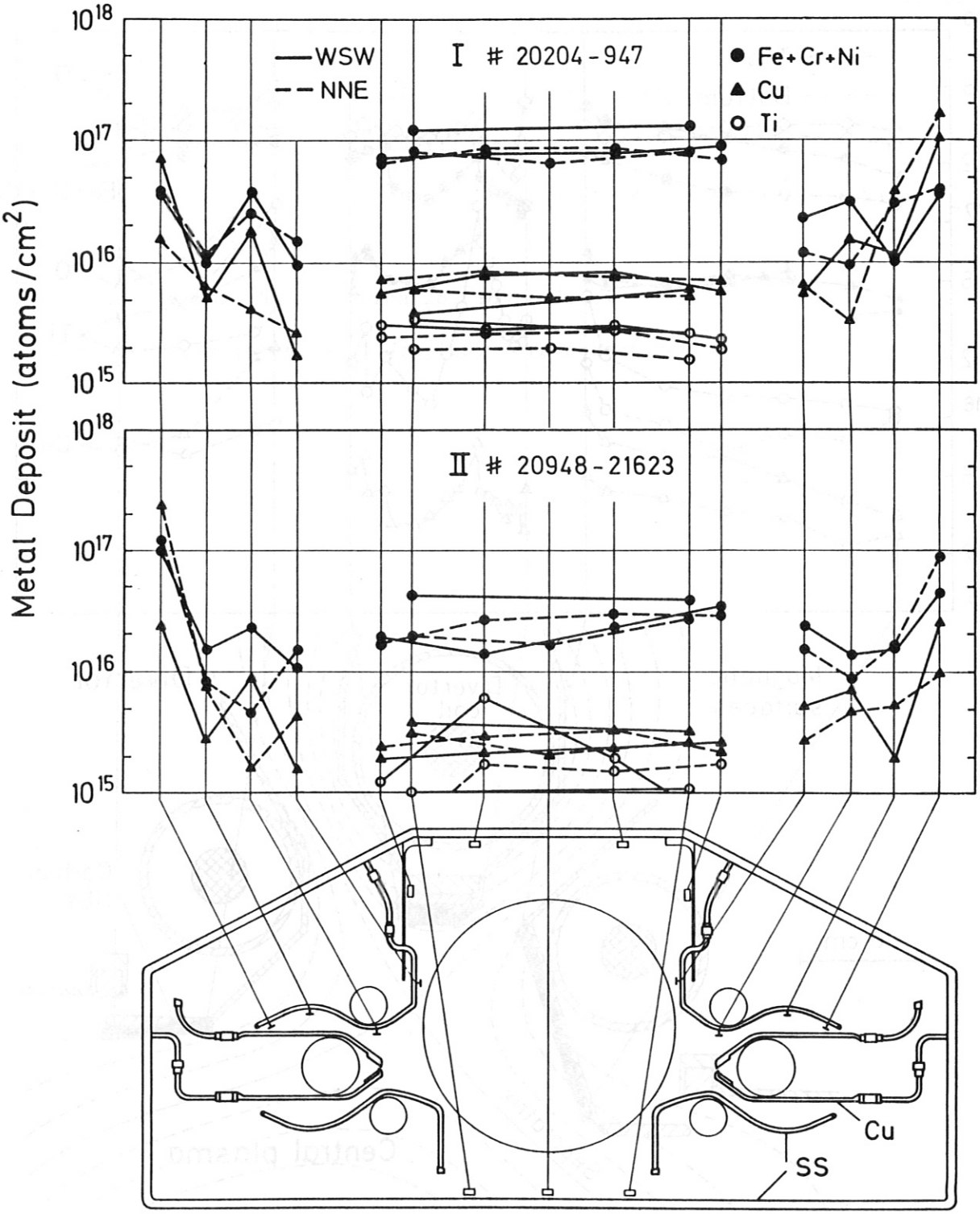
Metal Deposit (atoms/cm²)
10¹⁸
10¹⁷
10¹⁶
10¹⁵
—WSW
– – NNE
I # 20204-947
II # 20948-21623
● Fe+Cr+Ni
▲ Cu
○ Ti
Cu
SS

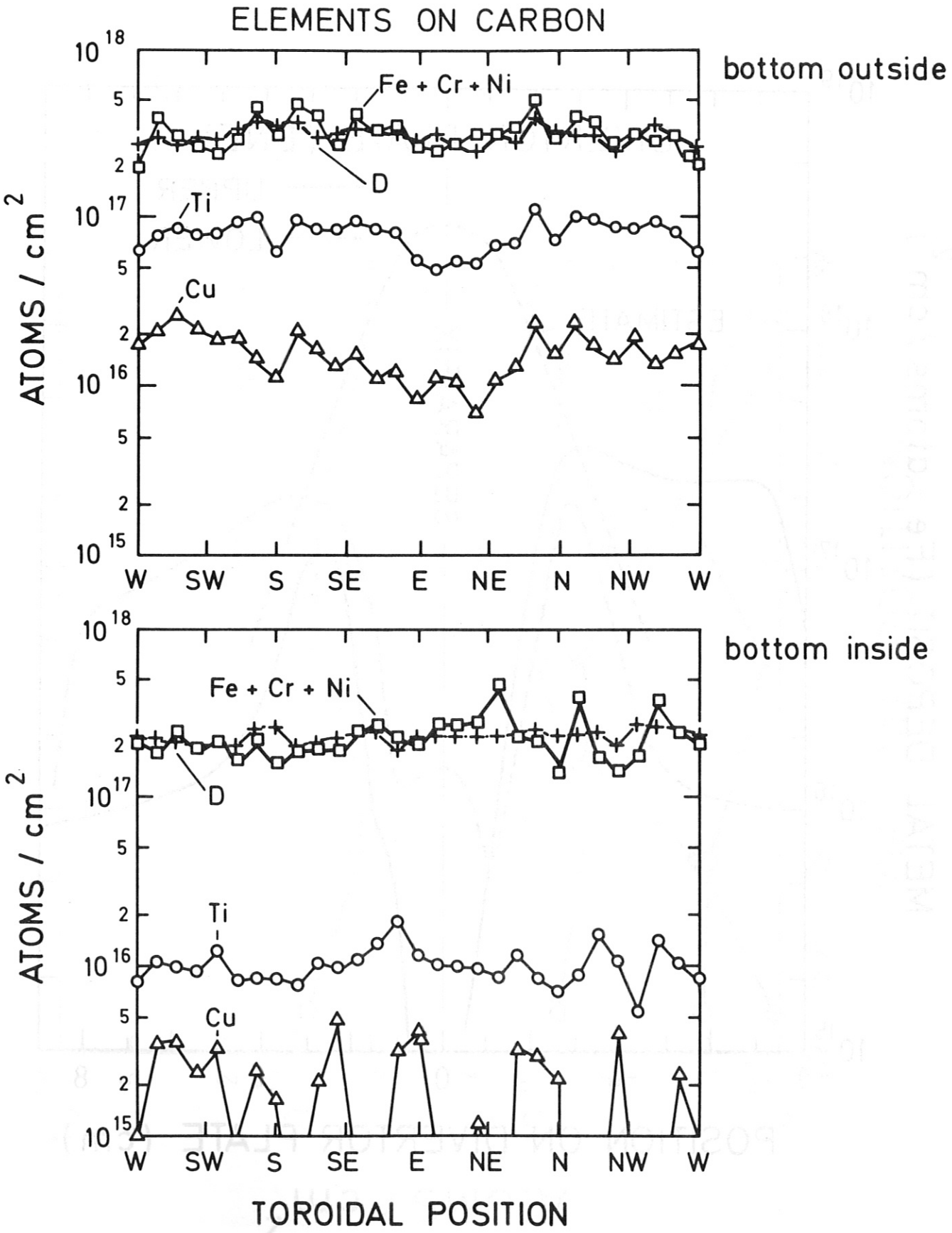
ELEMENTS ON CARBON
bottom outside
bottom inside
ATOMS / cm 2
Fe + Cr + Ni
D
Ti
Cu
10 18
10 17
10 16
10 15
5
2
W SW S SE E NE N NW W
TOROIDAL POSITION

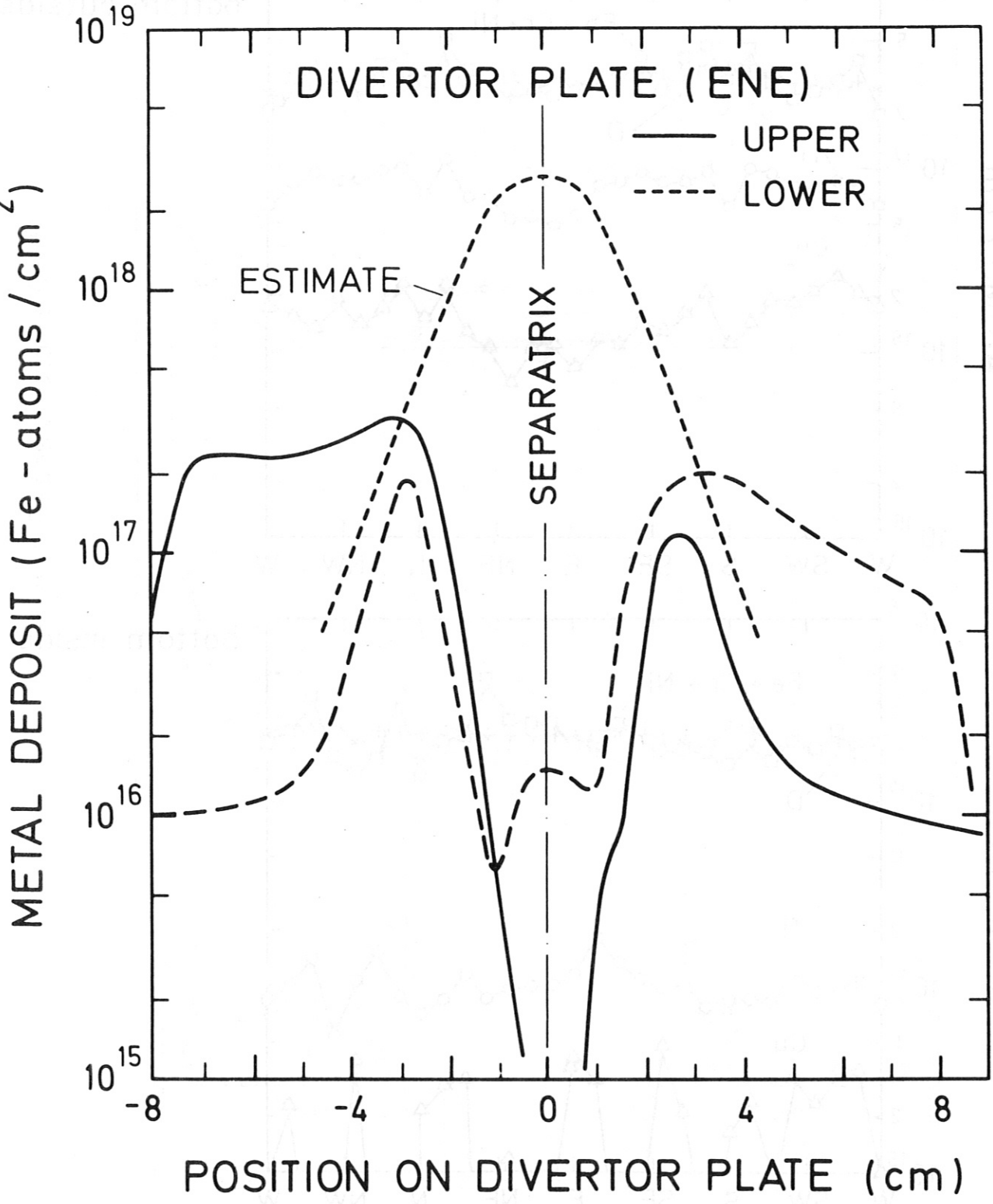
DIVERTOR PLATE (ENE)
UPPER
LOWER
ESTIMATE
SEPARATRIX
METAL DEPOSIT (Fe - atoms / cm^2)
10^{19}
10^{18}
10^{17}
10^{16}
10^{15}
-8
-4
0
4
8
POSITION ON DIVERTOR PLATE (cm)

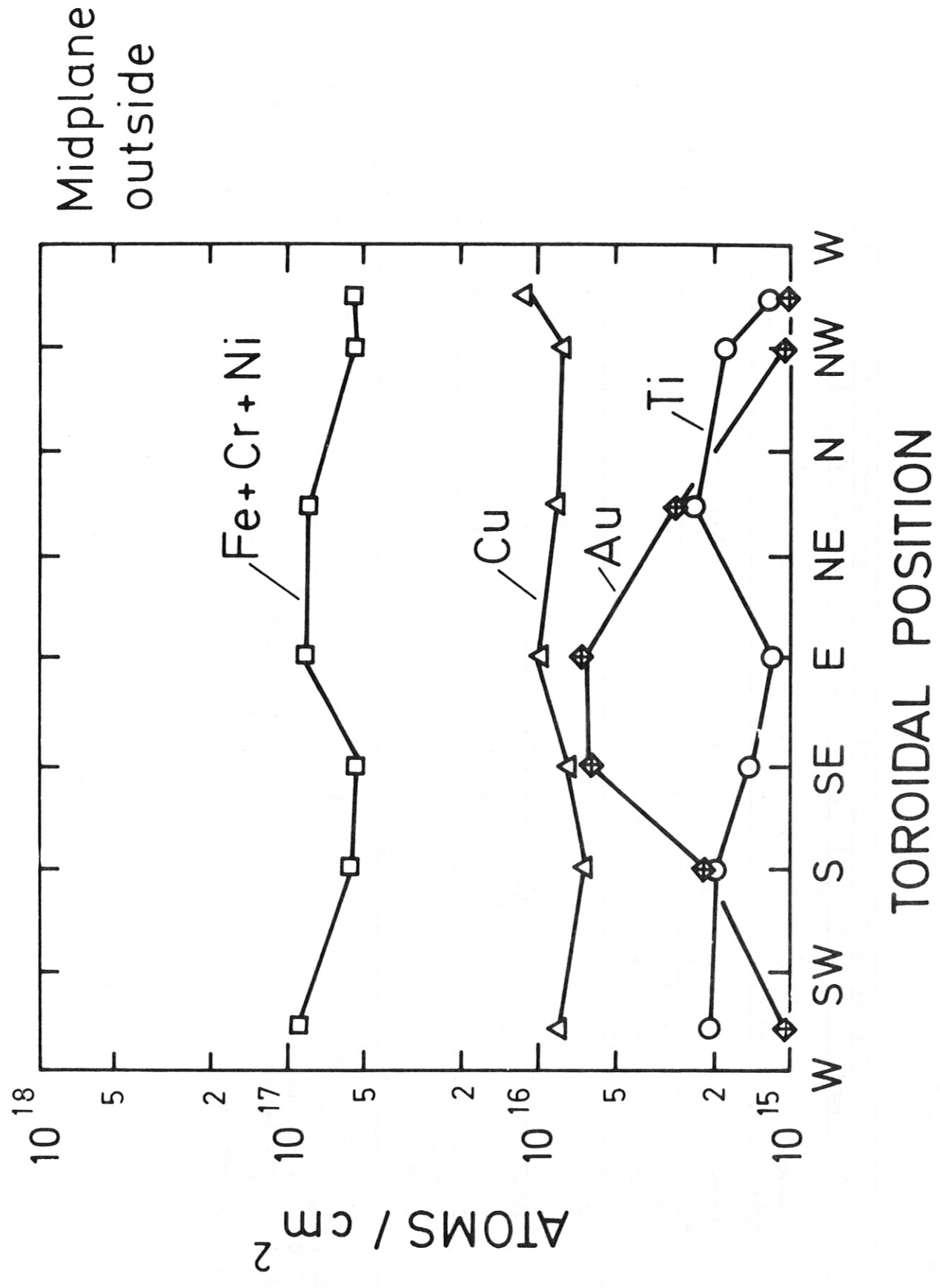
Midplane
outside
Fe+Cr+Ni
Cu
Au
Ti
ATOMS / cm²
10¹⁸
5
2
10¹⁷
5
2
10¹⁶
5
2
10¹⁵
W SW S SE E NE N NW W
TOROIDAL POSITION

Table 1: Eroded and deposited metal fluxes measured by various surface probes, charge exchange neutral spectroscopy and by optical spectroscopy

ASDEX	Old divertor config. (Ti-plates)		new divertor config. (Cu-plates)	
	Fe-flux (atoms/s)	Ti-flux (atoms/s)	Fe-flux (atoms/s)	Cu-flux (atoms/s)
main chamber wall	$4.5 \cdot 10^{18}$ f) $\geq 1.5 \cdot 10^{18}$ g)	$4.5 \cdot 10^{17}$ f)	$2.5 \cdot 10^{18}$ a) $4.4 \cdot 10^{18}$ d)	$2.5 \cdot 10^{17}$ a) $7 \cdot 10^{17}$ d)
divertor chamber wall	$8 \cdot 10^{17}$ g)	$6 \cdot 10^{18}$ g)	$1.8 \cdot 10^{18}$ d)	$2.4 \cdot 10^{18}$ d)
divertor plates	$1 \cdot 10^{18}$(OH) i) $1 \cdot 10^{19}$(NI) b) $2 \cdot 10^{17}$ l)	$6 \cdot 10^{16}$	$9 \cdot 10^{17}$ $1.8 \cdot 10^{18}$ b)	$1.2 \cdot 10^{18}$ $9 \cdot 10^{17}$ b)
main chamber wall	$1 \div 3 \cdot 10^{18}$(OH) k) $\leq 3 \cdot 10^{19}$(NI) k)	$1-3 \cdot 10^{17}$(OH) e) $3 \cdot 10^{18}$(NI) e)	$4 \cdot 10^{18}$(OH) a)	$4 \cdot 10^{17}$ e)
divertor chamber wall	negligible	negligible	not measured	not measured
divertor plates	$\gtrsim 2 \cdot 10^{18}$ e)	$4 \cdot 10^{17}$(OH) c) $6 \cdot 10^{17}$(OH) h)	$2 \cdot 10^{18}$ e)	$3 \cdot 10^{18}$(OH) c) $3 \cdot 10^{19}$(NI) c) $1.8 \cdot 10^{19}$ b)

a) G.Staudenmaier et al. /32/
b) E.Taglauer et al. /29/
c) G.Janeschitz et al. /23/
d) long term samples 1987
e) estimate
f) long term samples 1986
g) P. Staib et al. /13/
h) B. Schweer et al., /6/
i) E. Taglauer et al., /28/
k) G. Staudenmaier et al., /2/
l) Ti-divertor plate after 20 000 discharges

PLASMA INDUCED CHANGES OF A METALLIC DIVERTOR NEUTRALIZER PLATE FROM ASDEX ANALYSED BY PHOTOACOUSTICS

B.K. Bein, M. Wojczak, and J. Pelzl

Ruhr-Universität Bochum, Institut für Experimentalphysik VI
D-4630 Bochum, P.O. Box 102148, Federal Republic of Germany

Abstract

A metallic divertor neutralizer plate of the ASDEX tokamak has been analysed by photoacoustics, a thermal wave method with acoustic detection, to obtain space resolved thermal depth profiles and to characterize the plasma-induced changes of the plate material. In the intersection region between the plasma separatrix and the neutralizer plate where the maximum power deposition occurred during incorporation in ASDEX, the effusivity $\sqrt{k\rho c}$, the thermophysical parameter relevant for time dependent surface heating processes, increased about 18 % over its original value.

1. Introduction

To establish thermal wave analysis as a tool to characterize fusion plasma-induced changes of metallic wall components, a divertor neutralizer plate of ASDEX has been analysed by frequency-dependent photoacoustics. Space resolved thermal depth profiles have been measured and interpreted quantitatively. In this work we try to relate the changes in the thermophysical properties to plasma-surface interactions and to identify dominant effects. The plate analysed had been incorporated in the lower divertor chamber (sector SWS) of ASDEX (Fig. 1) at the ion side, the outer side, from the beginning of the experiment 1979 until summer 1985. Thus this plate accompanied the continuous progress of ASDEX to higher plasma temperatures, higher particle and energy fluxes onto the neutralizer plates.
During this time about 20 000 discharges were run with an average duration of 2.5 s, initially with ohmic heating alone; about 9000 of

them were run with additional heating, mainly neutral beam injection up to 4 MW during 400 ms, and ultimately ICRH and LH heating. Most of the discharges were run in the Double-Null divertor mode, where the neutralizer plates of both the lower and the upper divertor chamber are in contact with the plasma. The neutralizer plates consisting of the titanium alloy TiAl6V4 (CONTIMET ALV64) were 2 mm thick, 18 cm wide in poloidal direction, and between 60 and 80 cm long in toroidal direction. The outer neutralizer plates formed a toroidal loop of approximately 10 m length. The maximum tolerable heat load was 400 J/cm² for a temperature raise of approximately 800°C. Between successive discharges the plates cooled down only due to heat radiation and conduction through the mechanical support structure [1].

The plate analysed here had to withstand higher heat loads at one of its edges in toroidal direction. Due to thermal stresses the mechanical fixing was broken there, the plate was distorted and heavily damaged at this edge. The measurements reported here have been restricted to regions near the opposite toroidal edge which had remained fixed to the support structure and where thus the usual toroidal symmetry can be assumed for the particle and energy deposition. Optically the plate shows a bright metallic horizontal trace, about 13 mm wide, between 55 mm and 68 mm distance from its lower edge (Fig. 2), where the last intense plasma-solid contact took place before removal from the experiment. This intersection between the separatrix and the neutralizer plate changed with time, depending on the plasma current, the current of the divertor field coils, and the poloidal ß changing due to additional heating. Consequently, other less bright horizontal traces are still visible at major distances, e.g. 100 mm - 110 mm, from the lower edge, former intersections between separatrix and neutralizer plate. Above and below the bright metallic trace a gray deposition of material can be seen (Fig. 2). The measurements presented subsequently are from a stripe perpendicular to the horizontal intersection between separatrix and neutralizer plate plate, mainly from the bright separatrix region and its neighborhood. Data from this region are interesting for two reasons: First, the effects of plasma exposure on the metal can be measured here free from additional effects of material deposition, and secondly,

thermophysical data from this region are of interest for the power deposition calculations based on IR thermography [2].

2. Experimental

The frequency dependent measurements and interpretation of amplitude and phase of the thermal wave probe give information about the depth profile of the effusivity $\sqrt{k\rho c}$, the thermophysical parameter relevant for time dependent surface heating processes [3]; here k, ρ and c are the thermal conductivity, density, and specific heat capacity of the plate material. To eliminate the response characteristics of the measurement device and to calibrate the measured signals, both the photoacoustic amplitude and phase are compared to the signals measured with reference materials (quartz glass with a carbon coating of 25 $\mu g/cm^2$) of known thermal properties by a 'normalization procedure'. If opaque or surface-heated homogeneous samples and reference materials are considered, the (inversely) normalized photoacoustic amplitude [3] is given by

$$S_r(f)/S_s(f) = \eta_r \sqrt{(koc)_s} \;/\; \eta_s \sqrt{(koc)_r} \quad , \qquad (1)$$

where $S_r(f)$ and $S_s(f)$ are the measured frequency dependent amplitudes, η_r and η_s the photothermal conversion efficiencies, and $\sqrt{(k\rho c)_r}$ and $\sqrt{(k\rho c)_s}$ the effusivities of the reference and sample, respectively. In order to distinguish between the changes of the optical properties η_s induced by the plasma and the changes of the thermophysical properties, the reflectivity has been measured in an additional optical experiment for the same wave length of the laser light used in the photoacoustic experiment. The details about the experimental device and methods, developed for the photoacoustic analysis of graphite limiters, were published earlier [4,5].
To improve our understanding of the changes of the thermal properties measured and to facilitate the correlation with plasma surface effects, additional measurements such as electron microprobe analysis (EIXE), light and electron microscopy, Vickers hardness, etc.[6] were done.

3. Results

Depending on the distance from the intersection between separatrix and neutralizer plate (Fig. 2) three different types of thermal depth

profiles were found on the plate:

(1) In the region of the main plasma-solid contact between the positions 55 mm and 68 mm, where the maximum power deposition occurred during incorporation in ASDEX and where the plate now shows a bright metallic surface, the normalized amplitudes which are corrected for the measured local photothermal conversion efficiencies,

$$S_r(f)\,\eta_s \;/\; S_s(f)\,\eta_r = \sqrt{(k\varrho c)_s} \;/\; \sqrt{(k\varrho c)_r} \quad , \qquad (2)$$

and thus also the effusivity values increased and are now higher than the value for the material without plasma exposure, at least if larger penetration depths of the thermal wave $\mu \sim f^{-1/2}$ are considered. This annealing effect may be related to thermal cycling by the plasma heat deposition. For the central position 60 mm the effusivity even increased about 18% over its original value, and only for a very short penetration depth the frequency dependence of this profile additionally shows a thermal depth structure slightly falling towards the surface. The metal surface here is nearly free from material deposition, as can be seen from both electron micrography [6] and visible light microscopy (Fig. 4a), and thus this additional surface effect may be related to lattice damage induced by particle bombardment. For the positions 55 mm, 65 mm, and position 67.5 mm which marks the transition from the separatrix to the region of material redeposition, the profiles start at the surface at relatively lower values and only after comparatively larger penetration depths the effusivity grows over the original value. The beginning deposition of material (Fig. 4b) which consists mainly of Ti droplets, as found by electron micropobe analysis [6], is probably responsible for the lower effusivity at the surface and the depth structure.

The normalized amplitudes (Eq. 2) plotted versus the inverse of the square root of the heating modulation frequency in Fig. 3, 5 and 7 provide the depth variation. The corresponding geometrical penetration depth from the surface is approximately given by the thermal wave length

$$x_0 \lesssim \lambda_0 = \sqrt{4\,\pi\, a_0 / f} \quad , \qquad (3)$$

which depends on the thermal diffusivity a_0. Measuring the photoacoustic phase shift as a function of the modulation frequency for a

TiAl6V4 sample of limited finite thickness [7], the thermal diffusivity was determined to be $a_o = 2.96\ 10^{-6}$ m²/s for the material without plasma exposure, in good agreement with the literature value. For the profile of position 60 mm, the effusivity is nearly unchanged over the frequency interval covered by our measurement. In this case the thermal wave length can be corrected for the effective value after plasma exposure $\lambda_s = \sqrt{4\pi a_s/f} = \sqrt{a_s/a_o}\,\lambda_o \approx \sqrt{(k\varrho c)_s/(k\varrho c)_o}\,\lambda_o = 1.18\,\lambda_o$, where we assume that the plasma heat deposition mainly affected the thermal conductivity k_s and not the density and specific heat capacity $(\varrho c)_s = (\varrho c)_o$. For the lower frequency limit of the measurements, f= 40 Hz, the annealing effect has thus been measured over a penetration depth up to 1 mm. Measurements at still lower frequencies would be necessary for a more exact limitation of the further penetration depth in the plate.

(2) Farther away from the intersection separatrix/ neutralizer plate, for example at the positions 30 mm, 45 mm and 50 mm where a darker layer of redeposited material is seen (Fig. 2), the thermal depth profiles start with very low effusivity values $\sqrt{(k\varrho c)_s}$ at the surface, and only for larger thermal penetration depths the original value is reached (Fig. 5). The reduced thermal properties of the deposited material and the contact resistance between the deposited layers and the substrate may be accountable. As shown by the electron micrograph from position 30 mm (Fig. 6) the regions of dominant material deposition can have a multilayer structure.

(3) In a limited region close to the main plasma-solid contact, above the position of the separatrix, the thermal depth profiles (Fig. 7) show a behavior as foreseen and characteristic for delaminated coatings [8,9,10] or layered samples of reduced thermal properties below a well conducting surface layer. Both the amplitudes and the normalized phases between positions 70 mm and 75 mm (Fig. 8) accuse this behavior, whereas the nearby positions 67.5 mm and 82 mm show the typical thermal depth profile behavior of material deposition layers. Electron micrographs from this region (Fig. 9) show a rough surface with thin cracks which are not visible at sample points elsewhere. A possible explanation for this "delamination" is cracking due to short, very intense heat pulses as observed in H-regime discharges by IR thermography. These additional peaks were

found shifted by a distance of approximately 1.4 cm towards the main plasma torus [11]. Other possible explanations for such a decreased effusivity below the surface - a layer of hydrogen or lattice damage below the surface due to energetic particle bombardment - could not be supported by evidence.

4. Conclusions

Frequency dependent photoacoustics are here proved to be a tool for characterizing plasma-solid interactions at metal surfaces in fusion devices. Characteristic thermal depth profiles were observed for regions of dominant plasma heat deposition, material redeposition, and of microcrack formation.

For the power deposition calculations based on thermographical measurements, an increase of the effusivity value by about 18%, as found for the separatrix region, corresponds according to

$$F_s(t) = \sqrt{(k\varrho c)_s/4\pi}\ \{ {}_0\!\int^{t} dt' [T_s(t)-T_s(t')]/(t-t')^{3/2} + 2\,[T_s(t) - T_s(t_o)]/\,t^{1/2}\ \} \qquad (4)$$

to an increase of the power deposition $F_s(t)$ by the same amount. $T_s(t)$ in Eq.(4), which is the solution for the semi-infinite solid [2], is the measured surface temperature evolution. It means, power deposition calculations based on literature values of the thermophysical properties would lead in this case to an underestimate of the plasma energy deposition by 18%. In the divertor tokamak ASDEX, where the plasma energy losses are mainly by radiation losses in the main torus and the four divertor chambers [12], this amount is not important for closing the energy gap of the discharge. In a limiter tokamak, however, where the percentage of the conductional-convectional energy losses is higher, such effectively increased effusivity values could be decisive for energy balance studies.

Frequency-dependent photoacoustics belong to the thermal wave methods which, based on the lock-in technique, are sensitive to small temperature oscillations. Using an alternative detection technique like IR radiometry, which can work non-contact in unaccessible hostile environments, such a thermal wave technique could be suited

to be applied in fusion devices for materials' studies and the control of wall components during the intervals between successive discharges.

Acknowledgements

We acknowledge the support and contribution of F. Wagner, G. Haas, D. Zasche, and H. Rapp, IPP Garching, to this work. At the same time we are grateful to W. Oswald and O. Reh, Ruhr-Universität Bochum, for their help with the electron microprobe analysis and microscopy and the optical measurements.

References

[1] H. Rapp, H. Niedermeyer, M. Kornherr, and ASDEX team, In: Proc. 14th SOFT, Avignon, France, (1986).

[2] B.K. Bein and E.R. Müller, J. Nucl. Mater. 111 & 112 (1982) 548.

[3] B.K. Bein, S. Krueger, and J. Pelzl, J. Nucl. Mater. 128 & 129 (1984) 945.

[4] B.K. Bein, S. Krueger, and J. Pelzl, Can. J. Phys. 64 (1986) 1208-1216.

[5] S. Krueger, R. Kordecki, J. Pelzl, and B.K. Bein, J. Appl. Phys. 62 (1987) 55-61.

[6] M. Wojczak, Diploma thesis, Ruhr-Universität Bochum, FRG (1988).

[7] B.K. Bein, et al., to be publ. in High Temp. - High Pressures (1988).

[8] C.A. Bennett and R.R. Patty, Appl. Opt. 21 (1982) 111.

[9] G. Busse and A. Rosencwaig, Appl. Phys. Lett. 36 (1980) 815.

[10] P.M. Patel and D.P. Almond, J. of Materials Science 20 (1985) 955.

[11] E.R. Müller, B.K. Bein, and K. Steinmetz, Max-Planck-Institut für Plasmaphysik, Garching, FRG, Report IPP III/97 (1984).

[12] E.R. Müller, B.K. Bein, H. Niedermeyer, and the ASDEX team, In: 'Controlled Fusion and Plasma Physics', Europhysics Conference Abstracts (Ed. S. Methfessel) Vol 7D, Part I (1983) 47-50.

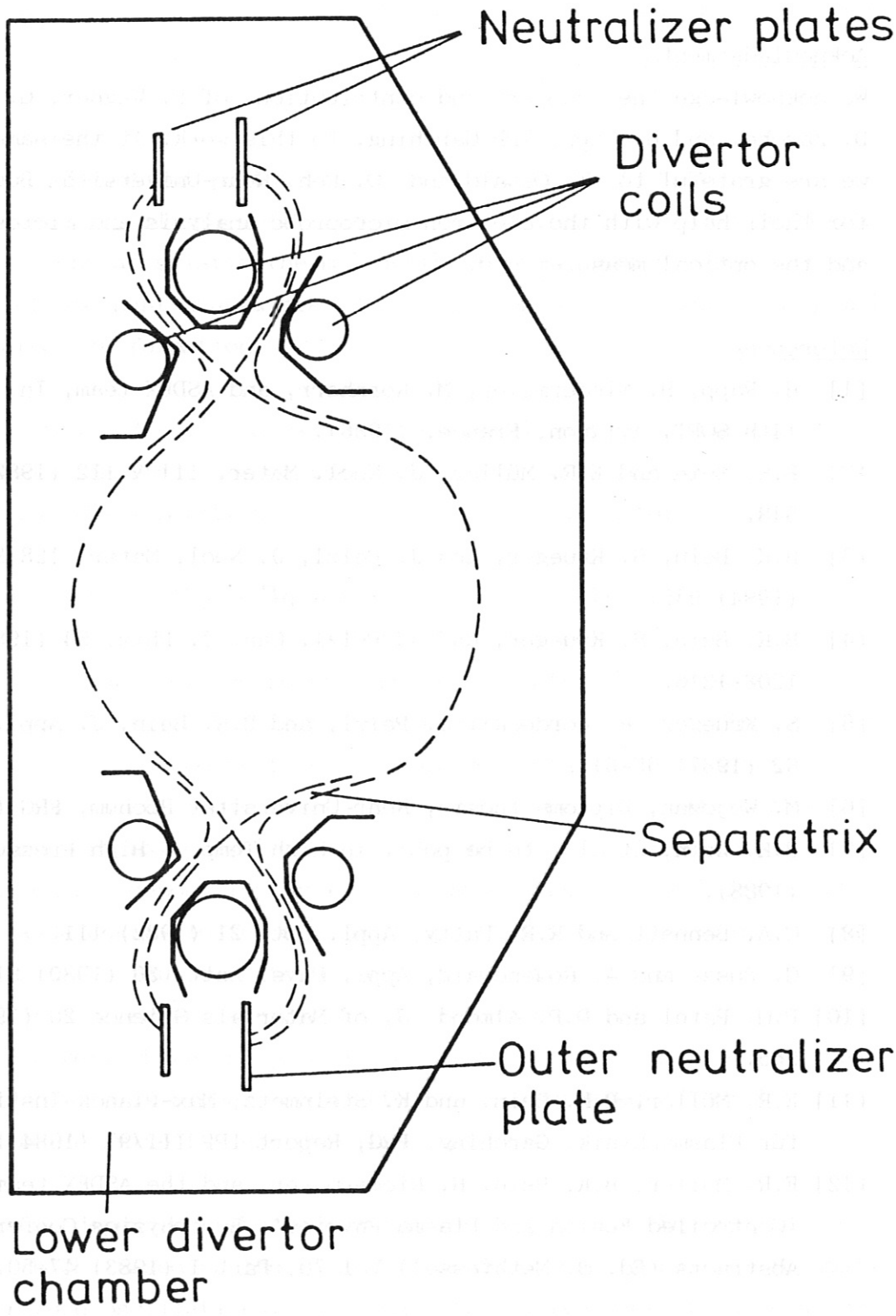

Fig. 1. Cross sectional view of the ASDEX tokamak - Position of the analysed divertor neutralizer plate.

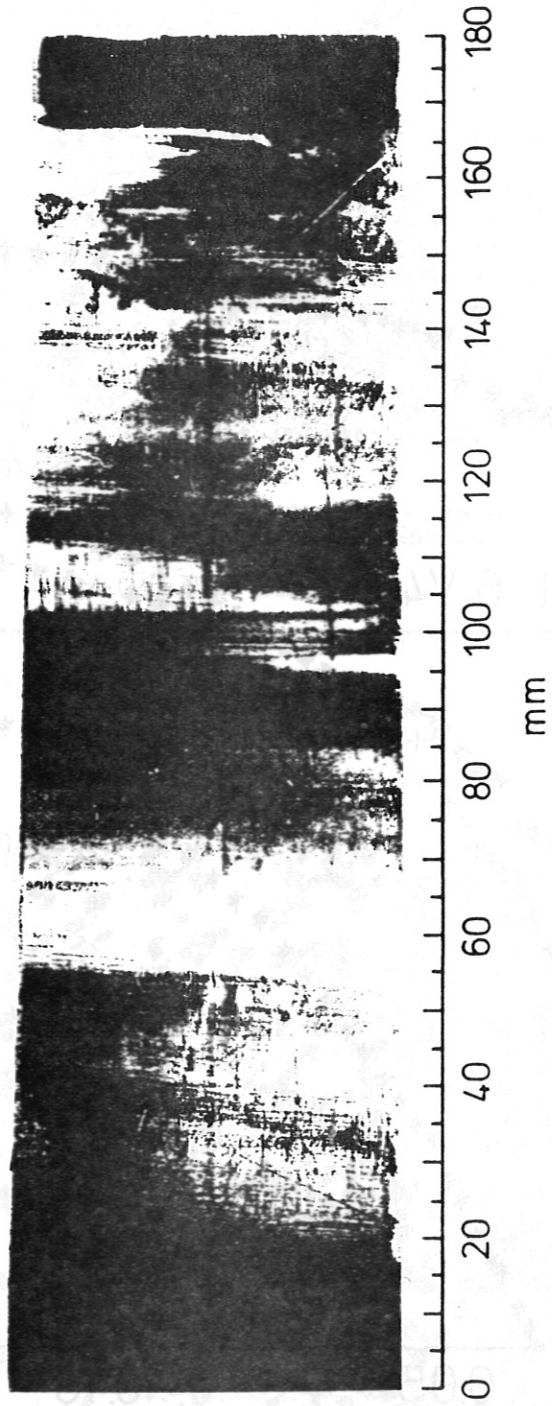

Fig. 2. Vertical stripe cut from the neutralizer plate of the lower outer divertor chamber of ASDEX (sector SWS) - Visual impression and localization of the sample points.

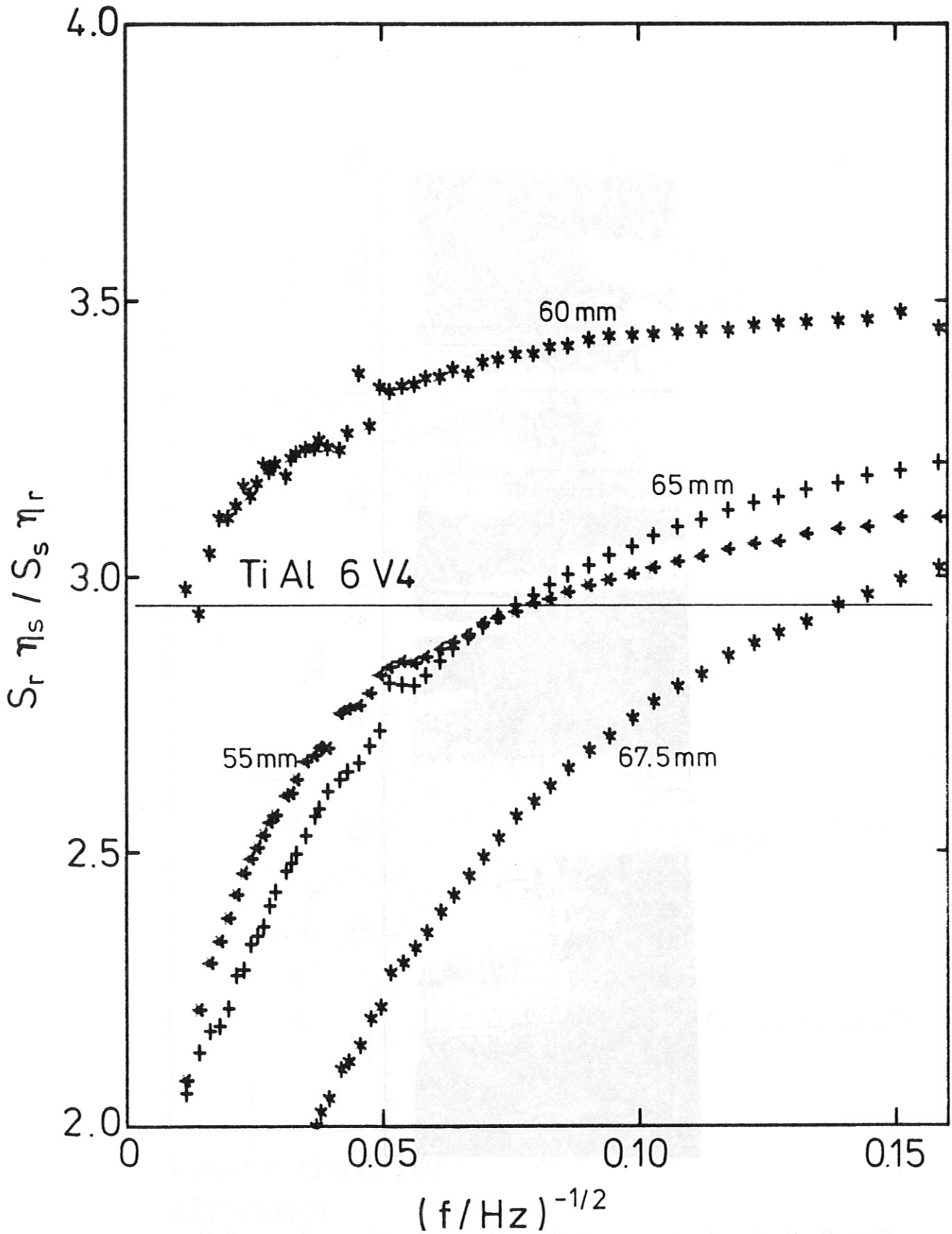

Fig. 3. Normalized photoacoustic amplitudes from the intersection region between separatrix and neutralizer plate, in comparison to a TiAl6V4 sample without plasma exposure (continuous straight line). Reference material for normalization is a quartz glass sample with a carbon coating of 25 $\mu g/cm^2$.

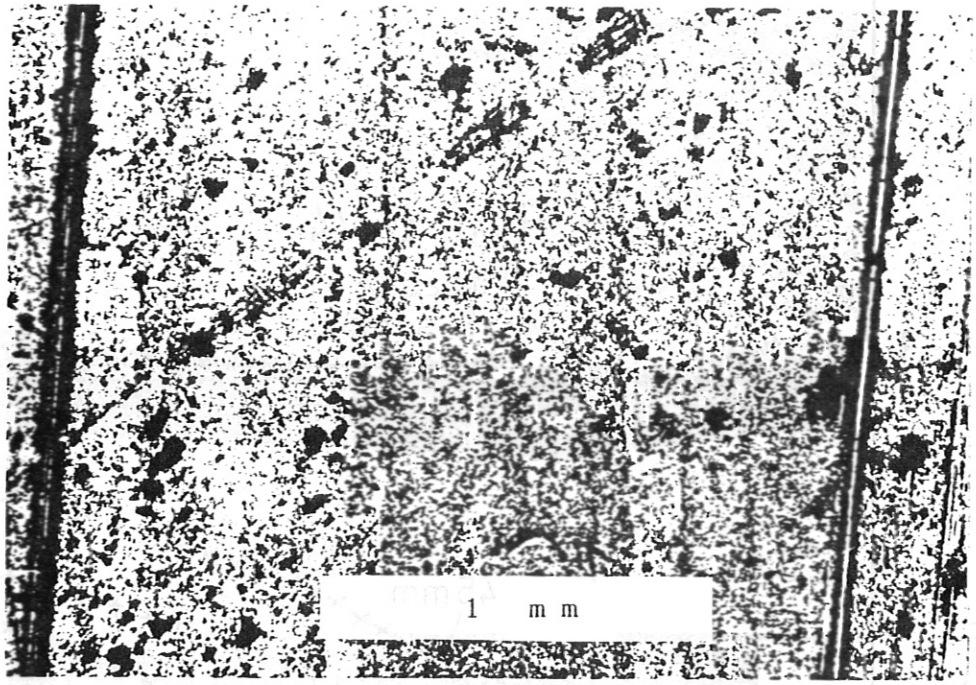

Fig. 4a.Microscopic view (visible light) from the central position 60 mm of the separatrix showing a smooth surface nearly free from material deposition.

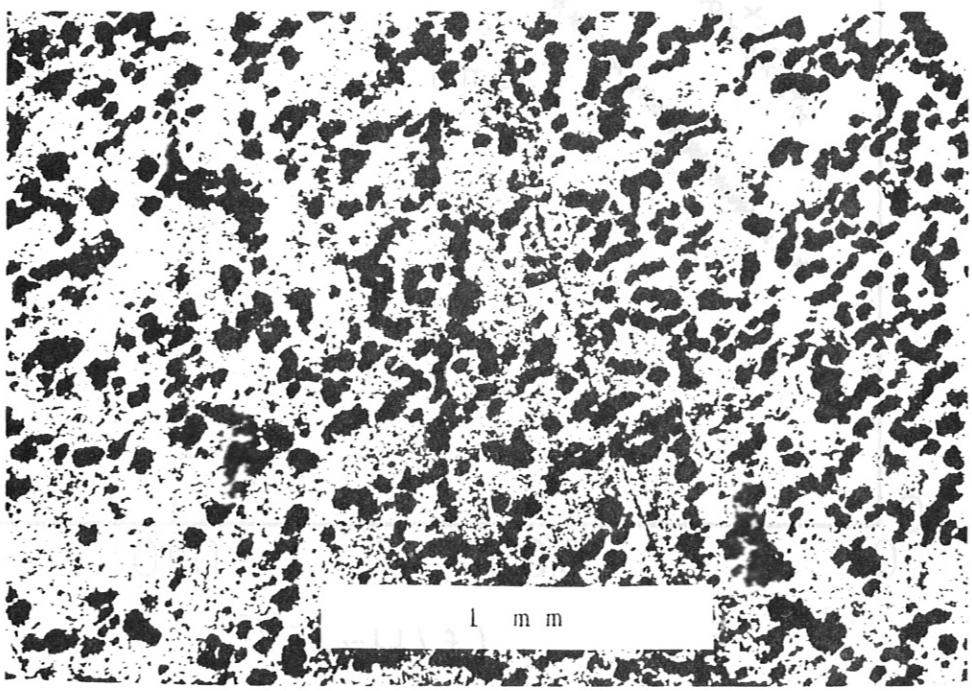

Fig. 4b.Microscopic view (visible light) from position 65 mm from the intersection between separatrix and neutralizer plate showing the droplet deposition of Ti.

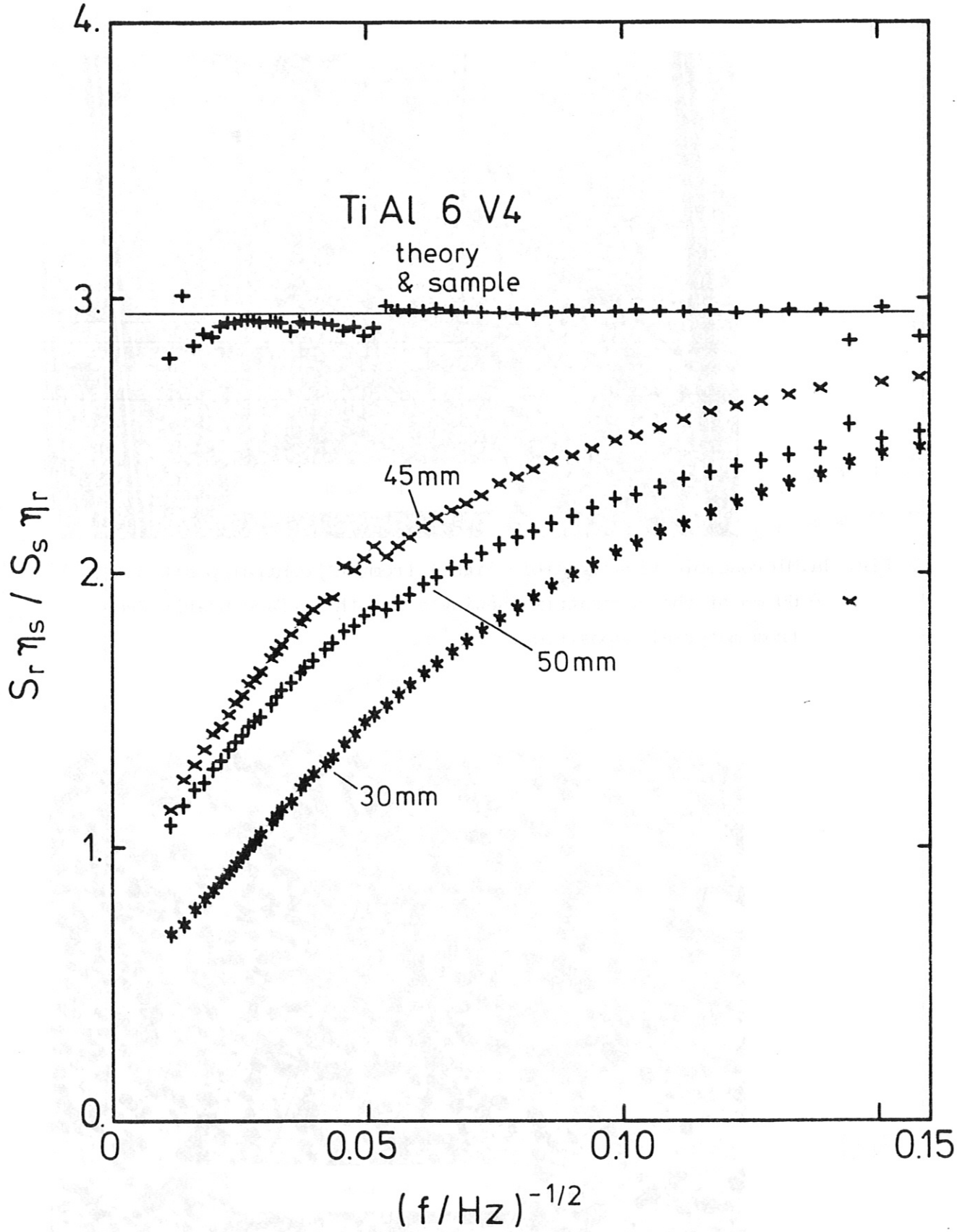

Fig. 5. Normalized photoacoustic amplitudes from the regions of visible material deposition, in comparison to the TiAl6V4 sample without plasma exposure. (The measured effusivity of this sample agrees with the literature value within a relative error of less than 3%.)

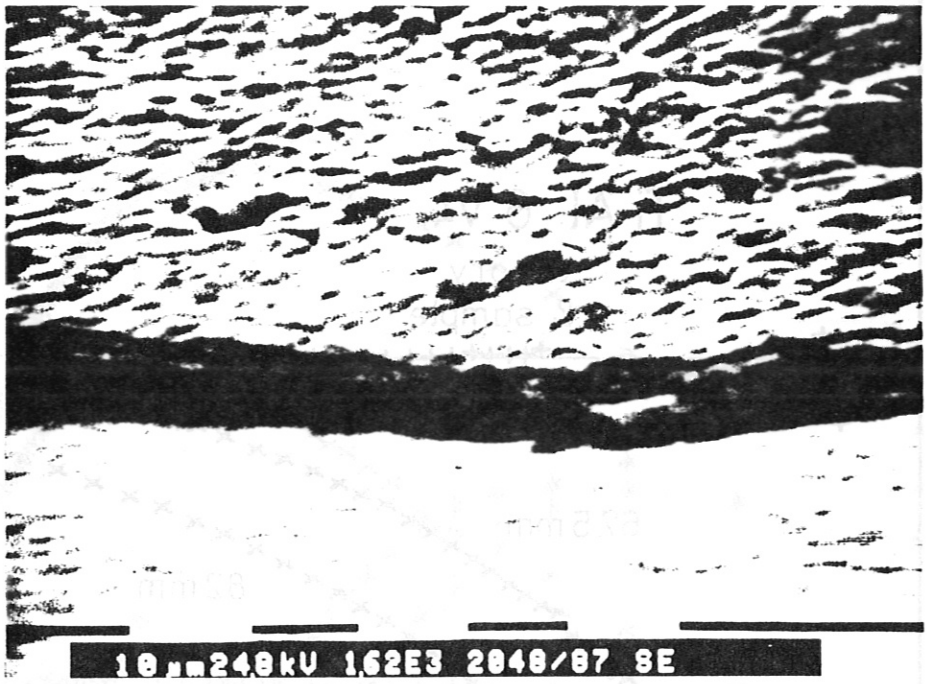

Fig. 6. Electron micrograph from sample position 30 mm, a region of dominant material redeposition, showing a multi-layered deposition of approximately 5 µm thickness.

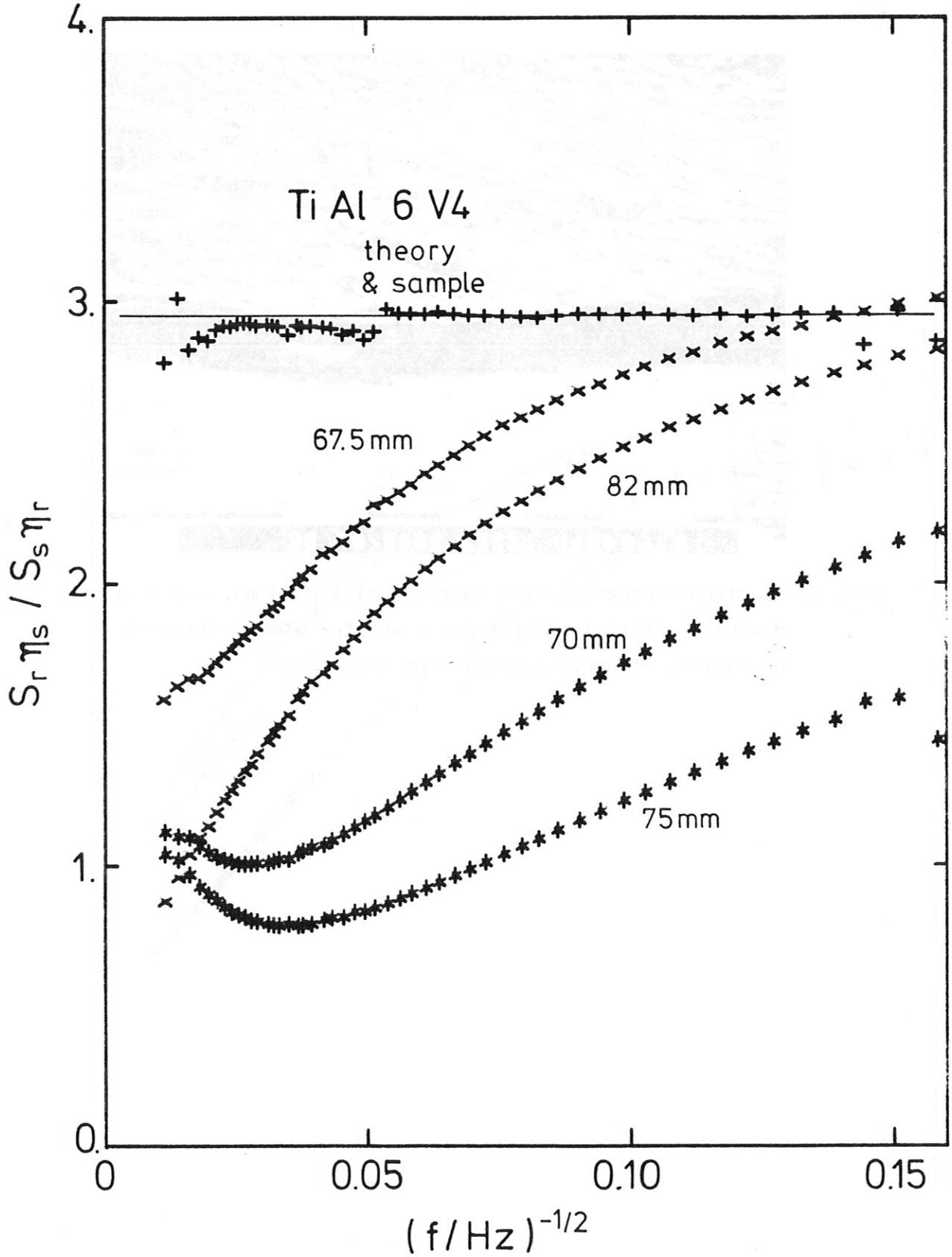

Fig. 7. Normalized photoacoustic amplitudes from a limited region close to the separatrix showing an "inversion" of the thermal depth profiles (70 mm and 75 mm), in comparison to typical "deposition" profiles nearby (67.5 mm and 82 mm) and the homogeneous TiAl6V4 sample without plasma exposure.

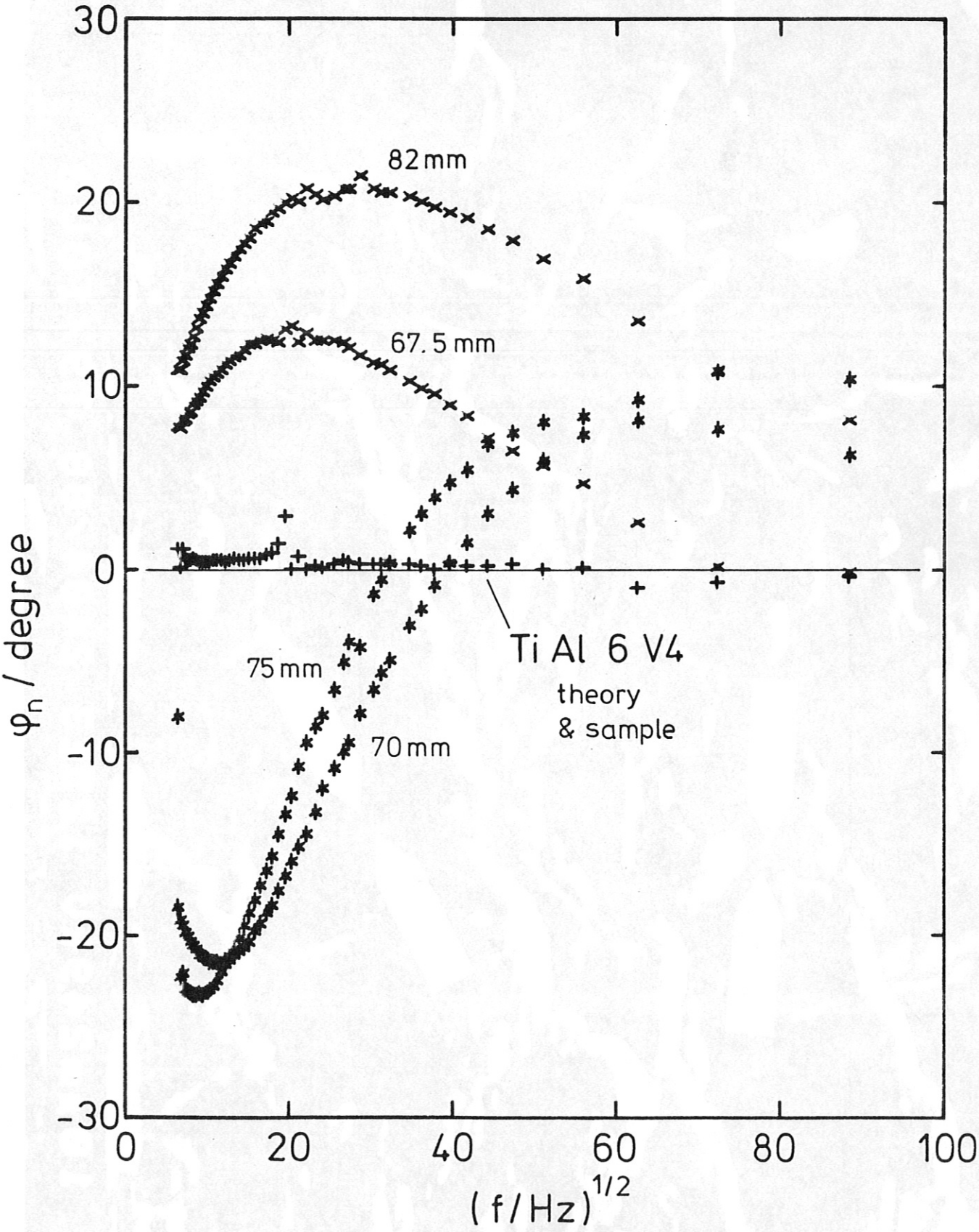

Fig. 8. Normalized phases from the "inversion" region (70 mm and 75 mm), in comparison to typical "deposition" profiles nereby (67.5 mm, 82 mm) and the homogeneous TiAl6V4 sample without plasma exposure.

Fig. 9. Electron micrograph from the "inversion" region, showing cracks of approximately 1 µm width in the deposited material.